UNIVERSITY OF CALIFORNIA SAN DIEGO

Area-selective Atomic Layer Deposition of Silicide and Oxides Using Inherent Substrate Dependent Processes

A dissertation submitted in partial satisfaction of the requirements for the degree Doctor of Philosophy

in

Materials Science and Engineering

by

Jong Youn Choi

Committee in Charge:

Professor Andrew C. Kummel, Chair
Professor Prabhakar Bandaru
Professor David P. Fenning
Professor Ivan K. Schuller
Professor Wei Xiong

2019

The Dissertation of Jong Youn Choi is approved, and it is acceptable in quality and form for publication on microfilm and electronically:

Chair

University of California San Diego

2019

DEDICATION

To my God who has guided my life until now and to my family for all the prayers, love and support during my graduate studies.

EPIGRAPH

A man’s heart plans his way, but the LORD directs his steps.

Proverbs 16:9

TABLE OF CONTENTS

LIST OF SYMBOLS AND ABBREVIATIONS

Å	angstrom
AC	alternating current
AFM	atomic force microscopy
ALD	atomic layer deposition
AS-ALD	area-selective atomic layer deposition
BE	binding energy
CB	conduction band
C_{max}	maximum capacitance
CV	capacitance voltage
CVD	chemical vapor deposition
DC	direct current
D_{it}	density of interface traps
DMADMS	Bis(dimethylamino)dimethylsilane
eV	electron volt
EOT	equivalent oxide thickness
Eq.	equation
FGA	forming gas anneal
GV	conductance voltage
HV	high vacuum
I	electric current
IMPM	inelastic mean free path
KE	kinetic energy

L	Langmuir
MOSCAP	metal oxide semiconductor capacitor
MOSFET	metal oxide semiconductor field effect transistor
nm	nanometer
pA	picoamps
PBN	pyrolitic boron nitride
STM	scanning tunneling microscopy
TMDS	tetramethyldisilazane
UHV	ultra-high vacuum
V	volts
VB	valence band
V_{fb}	flatband voltage
V_{th}	threshold voltage
XPS	x-ray photoelectron spectroscopy
υ	frequency
Φ_{spec}	spectrometer work function

LIST OF FIGURES

ACKNOWLEDGEMENTS

I would like to first acknowledge my advisor, Professor Andrew Kummel, who was always available for the insightful discussions and was responsible for managing the projects. Prof. Kummel has been an intelligent teacher/engineer who I learned a lot from. I especially appreciate all the opportunities to attend and present my work at numerous conferences including an international conference in South Korea. I really valued the experiences to give oral presentations in front of a broad range of audiences from academia and industry. Additionally, I confess that I appreciated Prof. Kummel's sense of humor and his straightforward philosophy towards life which made me enjoy talking to him regarding not only the research data but also general things in life.

I can confidently say that I would never be able to make it without Christopher Ahles, my best friend inside and outside of lab. I strongly believe those uncountable nights we spent together to solve the engineering problems (with booze) have brought us to the next level. I will never forget his encouragement and companionship during my graduate school period. Steven Wolf was greatly supportive both in terms of research as well as in getting me acclimated to life in San Diego. We had a number of stupid and funny moments together for the last four years which we will never forget. We will be good friends forever and I will always keep their positivity and kindness in my bottom of heart.

Scott is a good friend of mine and I know that I will miss his random Asian language jokes (those were customized for me). I was often impressed by his knowledge and skills that he established in a very short term and now I strongly believe that he will be one of the most successful people from Prof. Kummel's group. I was grateful to have him as a colleague.

I must also acknowledge all the other Kummel group members who I have shared precious moments of working with, dining out with, talking with, working with, attending conferences with and enjoying our weekly group meetings with: Michael Breeden, Victor Wang, Ashay Anurag, Harshil Kashyap, Dr. Sang Wook Park, Dr. Iljo Kwak, Dr. Mahmut Kavrik, Dr. Mary Edmonds and Dr. Kasra Sardashti. Thanks to Sofia Clemente, Robyn Swanland, Kristen Itahara and Heather Sears who helped me with lab purchases, shipping and trip coordination.

It was my great honor to be refereed by my committee members who were experts in physics, chemistry, mechanical and materials engineering. I cannot thank the committee members enough for actively participating and advising my thesis defense presentations. My committee includes Professor Prabhakar Bandaru, Professor Wei Xiong, Professor Ivan Schuller, and Professor David Fenning.

I want to give special thanks to my family for the endless support and belief in me: Jin-Gyu, Soonok, and Eunjeong Choi. I cannot imagine my life without their prayers and love. They are my motivation to persist in being diligent and hard-working. I will keep doing my best to make them always proud. I also appreciate Hyun Wook Jin, I look up to you for being a good husband and good father. Special thanks to my little angels, niece Seyeon Jin and nephew Hamin Jin. I promise I will make a better world for you two. I want to express my special thanks to my dear friends Jaeil Choi, Garam Kim and Jaeik Jang. It is never enough to say thank you. Thank you all.

This work was funded mainly by Applied Materials and partially by the San Diego Nanotechnology Infrastructure (SDNI) that was supported by the National Science Foundation (NSF).

Chapter 2, in part or in full, is a reprint of the material as it appears in the Applied Surface Science. J. Y. Choi, C. F. Ahles, R. Hung, N. Kim, and A. C. Kummel, "Selective atomic layer deposition of $MoSi_x$ on Si(001) in preference to Silicon Nitride and Silicon Oxide" Applied Surf. Sci., 2018, 462, 1008–1016. The dissertation author was the primary investigator and author of this paper.

Chapter 3, in part or in full, is reprinted with permission from J. Y. Choi, C. F. Ahles, K. T. Wong, S. Nemani, E. Yieh and A. C. Kummel, "Highly Selective Atomic Layer Deposition of $MoSiO_x$ Using Inherently Substrate-Dependent Processes" Applied Surf. Sci. (2019) (*manuscript accepted*). The dissertation author was the primary investigator and author of this paper.

Chapter 4, is in part or full, reprinted with permission from J. Y. Choi, C. F. Ahles, Y. Cho, A. Anurag, K. T. Wong, S. Nemani, E. Yieh and A. C. Kummel, "Selective Pulsed Chemical Vapor Deposition of Water-free HfO_x on Si in Preference to SiO_2 and SiCOH" (*manuscript in preparation to Applied Surface Science)*. The dissertation/thesis author was the primary investigator and author of this paper.

VITA

EDUCATION

2013 Bachelor of Science in Materials Science and Engineering, Korea University

2015 Master of Science in Materials Science and Engineering, Korea University

2019 Doctor of Philosophy in Materials Science and Engineering, University of California San Diego

PUBLICATIONS

J. Y. Choi, C. Ahles, Y. Cho, A. Anurag, K. Wong, S. Nemani, Ellie Yieh and A. Kummel. “Selective Pulsed Chemical Vapor Deposition of Water-free HfO_x on Si in Preference to SiO_2 and SiCOH”, (In preparation).

J. Y. Choi, C. Ahles, K. Wong, S. Nemani and A. Kummel. “Highly Selective Atomic Layer Deposition of MoSiOx Using Inherently Substrate-Dependent Processes”, Applied Surf. Sci., 2019 (accepted).

J. Y. Choi, C. F. Ahles, R. Hung, N. Kim, and A. C. Kummel "Selective atomic layer deposition of MoSix on Si (001) in preference to Silicon Nitride and Silicon Oxide" Applied Surf. Sci., 2018, 462, 1008–1016

C. F. Ahles, J. Y. Choi, S. Wolf, and A. C. Kummel "Selective Etching of Silicon in Preference to Germanium and $Si_{0.5}Ge_{0.5}$" ACS Appl. Mater. Interfaces, 2017, 9, 20947.

S. W. Park, J. Y. Choi, S. Siddiqui, B. Sahu, R. Galatage, N. Yoshida, J. Kachian, A. C. Kummel "Formation of atomically ordered and chemically selective Si-O-Ti monolayer of $Si_{0.5}Ge_{0.5}$(110) for a MIS structure via H_2O_2(g) functionalization" Journal of Chemical Physics, 2017, 146, 052808.

FIELD OF STUDY

Major Field: Materials Science and Engineering

Studies in Surface Science and Physical Chemistry
Professor Andrew C. Kummel

ABSTRACT OF THE DISSERTATION

Area-selective Atomic Layer Deposition of Silicide and Oxides Using Inherent Substrate Dependent Processes

by

Jong Youn Choi

Doctor of Philosophy in Materials Science and Engineering

University of California San Diego, 2019

Professor Andrew C. Kummel, Chair

For the last three decades, the semiconductor industry continued to grow in all aspects such as the device performance, power efficiency, data process speed, manufacturing yield and costs. One of the most important factors that made this big stride possible was a scaling of metal-oxide-semiconductor field effect transistors (MOSFETs), the fundamental and core component of microelectronic devices. The miniaturization of MOSFETs allowed for the integration of billions of transistors into a single microprocessor

chip, and currently the industry is looking into the issues of fabricating MOSFETs to further scale down to a sub-10 nm node using three-dimensional features.

A significant challenge of fabricating MOSFETs at the sub-10 nm node is the patterning process, which requires excellent spatial uniformity, a detailed positioning of material, and perfect thickness control. To avoid the technical complexity and limitation of a conventional top-down patterning technique, lithography, a new approach of patterning MOSFET components should be developed.

In this work, selective deposition of molybdenum silicide ($MoSi_x$), molybdenum silicate ($MoSiO_x$) and hafnium oxide (HfO_x) were demonstrated using selective atomic layer deposition, a bottom-up approach of nanoscale patterning for MOSFETs. Selectivities were obtained by the difference in the chemical reactivity of precursors between the different substrates of interest. The deposition was performed in a self-limiting manner or carefully controlled decomposition of the precursor which provides conformality with a sub-nanoscale thickness control. In sum, this study focuses on the inherently selective deposition processes based on the surface chemistry and the engineering techniques for selectivity enhancements which can be integrated into three-dimensional MOSFET fabrication processes.

Chapter 1

Introduction

1.1 Atomic Layer Deposition (ALD) and patterning Metal Oxide Semiconductor Field Effect Transistors

As Metal-oxide-semiconductor field effect transistors (MOSFETs) were scaled down to sub-10 nm node using three-dimensional features, a precise control of film thickness and conformality while maintaining the required electrical, physical and chemical qualities became substantial. [1,2] Therefore, atomic layer deposition (ALD) is employed since ALD provides a spatial conformality with atomic-scale thickness control by the self-limiting reactions of alternatingly dosed precursors.

For the patterning process, the conventional lithography technique met a limitation in resolution for sub-10 nm features due to a restricted focal plane of the X-ray source and imperfect alignment of the patterning masks. Three-dimensional MOSFETs (FinFets) in particular require a multi-patterning lithography process (i.e. double patterning) which has insufficient structural quality and resolution due to a memory effect originating from a chemical damage from reactive ion etching and structural complexity in mask alignment. [3-6] To overcome the complexity and limitations of the conventional top-down lithography scheme, ALD-enabled nanopatterning has been gaining attention to achieve higher resolution. For example, a spacer defined double patterning (SDDP) process employs a “spacer” to pattern an underlying film to the sub-10 nm in three-dimensions as shown in Fig. 1.1. [7,8] The pattern of the spacer is transferred to the underlying film; therefore, the spacer film is deposited using ALD to accomplish the high-resolution

features. In sum, implementing ALD is critical to achieve good film qualities and to enable a high-resolution patterning for the MOSFET components in three-dimensions.

1.2 Area-selective Atomic Layer Deposition

Area-selective Atomic Layer Deposition (AS-ALD) is a bottom-up approach of the patterning technique which leverages the advantages of ALD and the spontaneous positioning of a depositing film. The selectivity is obtained by the preferential reactions between the precursors and the target surface where a film grows. In contrast, the precursors show non-reactivity with the unwanted surface where the film should not be grown. Since the ALD selectivity relies on the chemical reactivity of the surface, surface modification is often employed using passivation or activation. [9,10] Another approach is to remove nucleation from the unwanted surface by adding plasma etching during the deposition. [11] However, adding the passivation or activation layers may require another process of selective removal of residual passivants or activants after the selective deposition is complete. The plasma process also necessitates damage control of the films and substrates from reactive ion etching and residual by-products.

AS-ALD using inherently substrate-dependent processes has a benefit of not using any preceding steps such as passivation or activation, or any additional plasma steps because it only utilizes the intrinsic differences in reactivity of the starting substrates. Therefore, the choice of the precursors and the substrate preparation are important for the intrinsic selective processes. [12-14] A comparison between the conventional patterning and ALD enabled patterning is depicted in Fig. 1.2.

1.3 X-ray Photoelectron Spectroscopy

X-ray photoelectron spectroscopy (XPS) is the main surface characterization technique employed to study the chemical compositions and chemical states of the substrates and thin films by analyzing the photo-emitted electrons from the samples. XPS can effectively investigate a surface coverage and saturation of chemisorbates within the topmost 1-3 nm of the sample by a quantitative analysis of the XPS spectra. The chemical states of the elements provide information about the other elements that they are bonded to; therefore, the empirical formula can be obtained. The composition of the XPS includes a monochromatic X-ray source, a multichannel hemispherical analyzer and a spectra acquisition software. An Al anode (Kα = 1486.7 eV) was used as a monochromatic X-ray source. As this characteristic X-ray irradiates a sample, the core level electrons are emitted from the sample atoms having a kinetic energy of the following equation:

$$E_{kinetic} = E_{h\upsilon} - E_{binding} - \Phi_{spec}$$

, where $E_{kinetic}$ is the kinetic energy of the electron, $E_{h\upsilon}$ is the energy of the incident X-ray, $E_{binding}$ is the binding energy of the electron, and Φ_{spec} is the work function of the spectrometer. [15] The photoemitted electrons are collected by a multichannel analyzer where the incoming electrons pass through the lenses and the fixed voltage (pass energy) applied to the hemisphere. [16] The electrical current from the collected electrons are amplified by a factor of 10^8 in an electron multiplier (Channeltron) and the counts of electrons are plotted as a function of $E_{binding}$ in the form of spectrum. A schematic of XPS is shown in Fig. 1.3.

1.4 Scanning Tunneling Microscopy

Scanning Tunneling Microscopy (STM) was employed to investigate the morphology of $MoSi_x$ in the Chapter 2. STM is a powerful surface imaging tool using the quantum tunneling effect of an electron between an atomically sharp tip (i.e. tungsten) and the topmost atom on the surface of interest by applying a bias to the tip. The STM tip sweeps around the surface only a few angstroms away by fine control of the tip using a piezoelectric feedback loop while maintaining a constant tunneling current between the sample and the tip. [17] The current from the tunneled electrons are amplified and processed by a control unit to record the data in the form of image. This technique allows mapping of morphology at atomic resolution in two different modes of filled states and empty states depends on the relative bias of the sample surface in respect to the tip. For example, a positively biased tip attracts the electrons from the filled orbitals of the atoms of the sample surface, resulted in a filled state imaging mode. For the $MoSi_x$/Si surface in Chapter 2 the surface morphologies were obtained using the filled state imaging mode of in-situ STM. This allowed us to investigate an as-deposited and in-situ annealed $MoSi_x$ surface without oxidizing metallic $MoSi_x$ by exposing the film into an ambient air. A schematic of a simplified STM circuit is shown in Fig. 1.4.

1.5 Atomic Force Microscopy

Atomic Force Microscopy (AFM) is employed to investigate a surface morphology of a deposited film in a sub-nanometer resolution. The components of AFM are a probe, a laser, a detector and feedback loop as described in Fig. 1.5. A sharp tip ($\Phi < 30$ nm) attached to an end of a cantilever, which oscillates near its resonance frequency, is used as

a probe. A laser constantly shines the back of the cantilever and a laser beam is reflected to the detector where the amplitude of the oscillation is measured. When the tip approaches to the sample close enough to interact with the surface with an atomic scale forces such as Van der Waals forces, the amplitude of the cantilever's oscillation changes. The change in amplitude of the oscillation is used for feedback loop device to control the distance between the cantilever and the sample operated by a piezoelectric controller. In this study, AFM was employed to characterize the $MoSiO_x$ and HfO_x surfaces in Chapter 3 and Chapter 4.

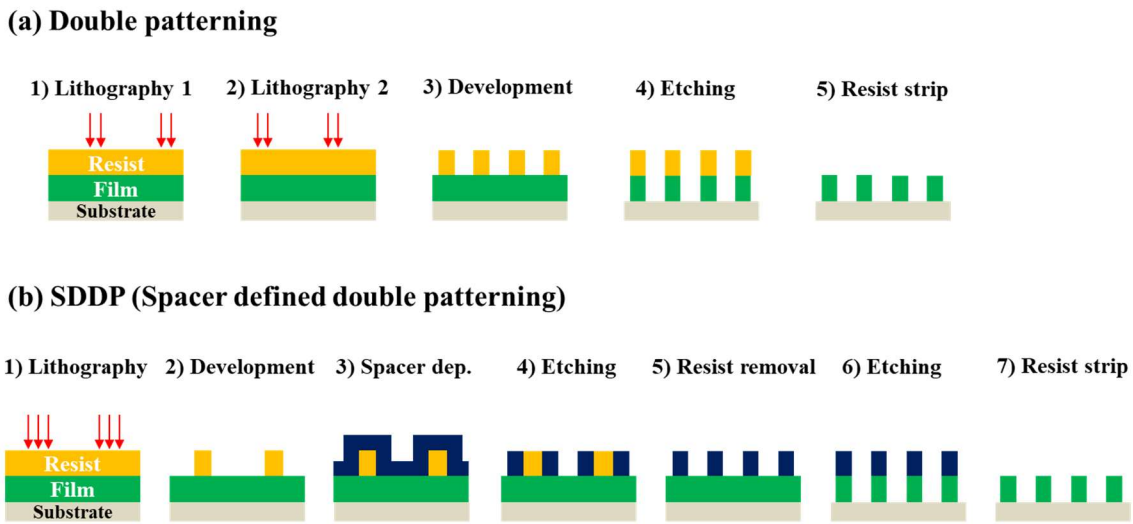

Figure 1.1 A comparison between the (a) double patterning and (b) spacer defined double patterning (SDDP) processes.

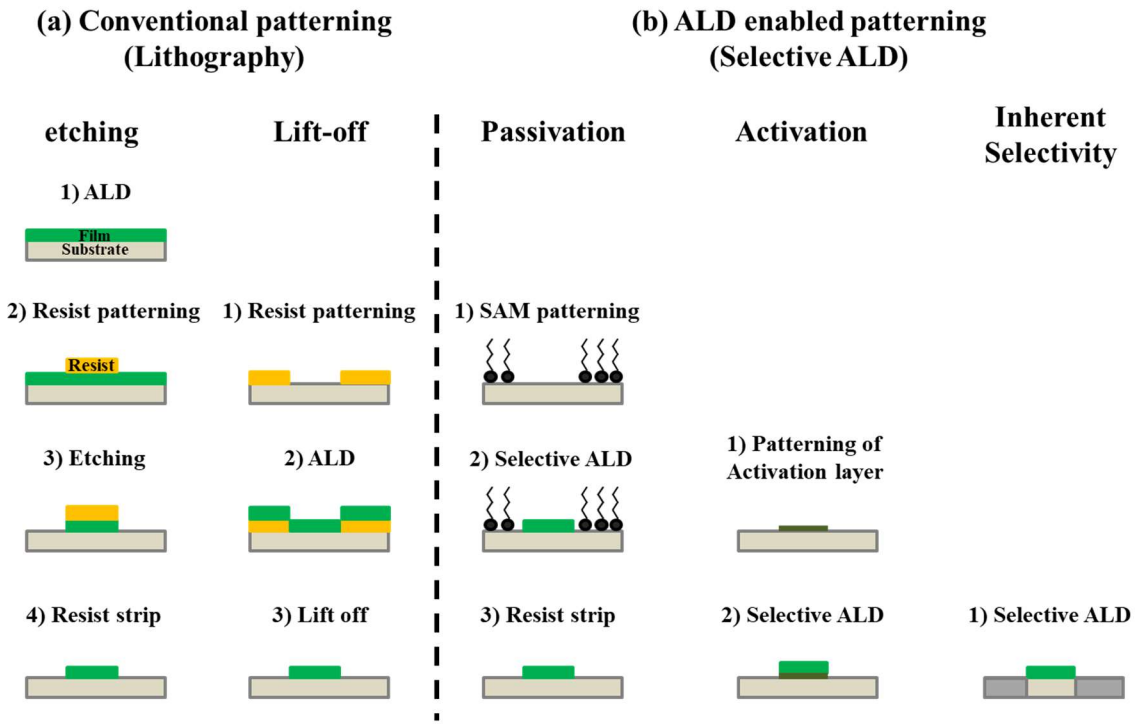

Figure 1.2. A comparison of the (a) conventional patterning (Lithography) and (b) ALD enabled patterning (Selective ALD) processes.

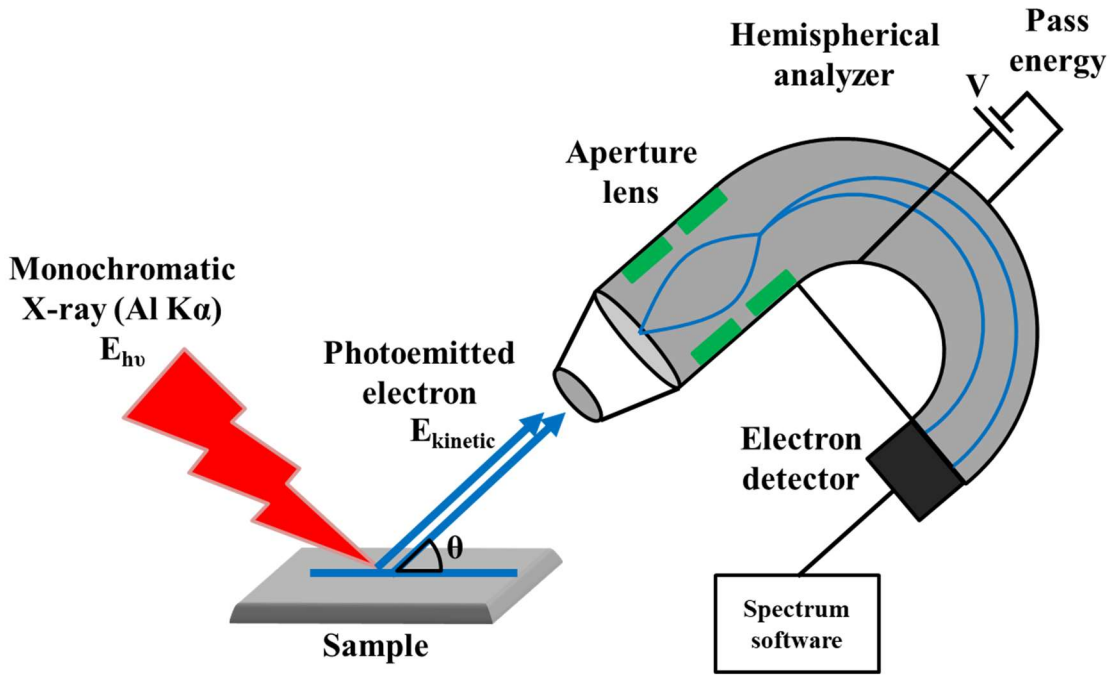

Figure 1.3. A schematic of X-ray Photoelectron Spectroscopy.

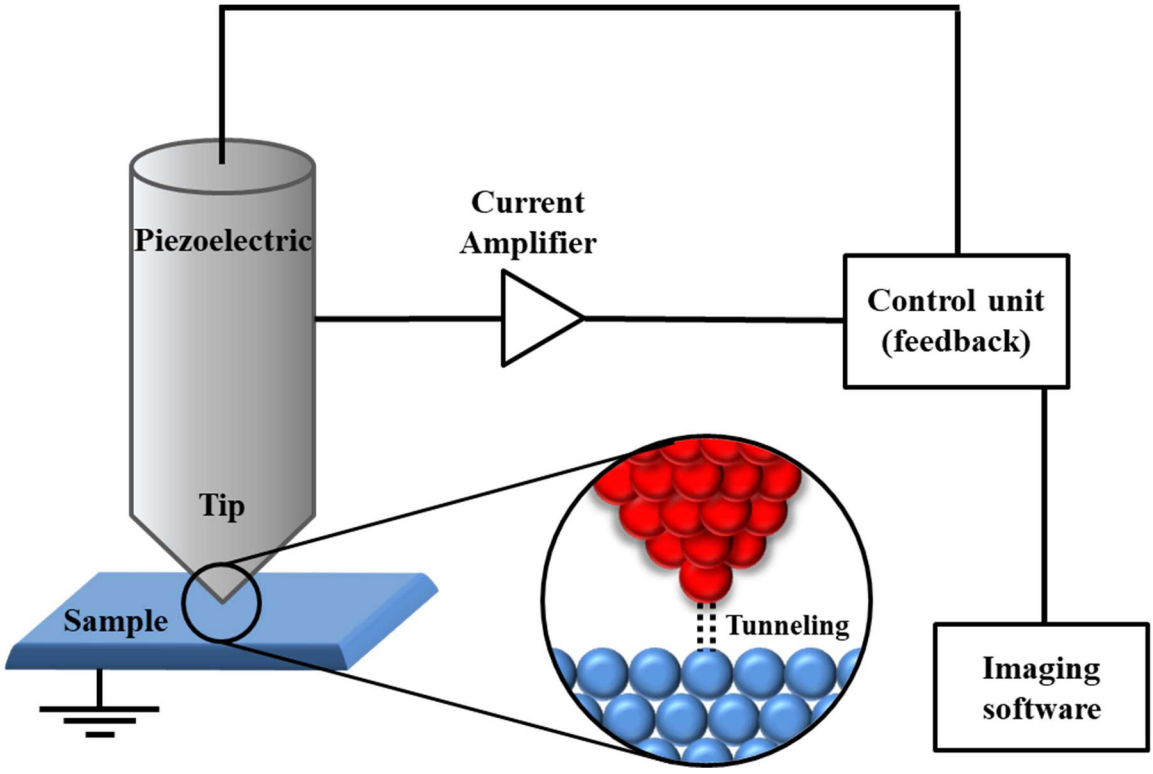

Figure 1.4. A schematic of the simplified Scanning Tunneling Microscopy circuit.

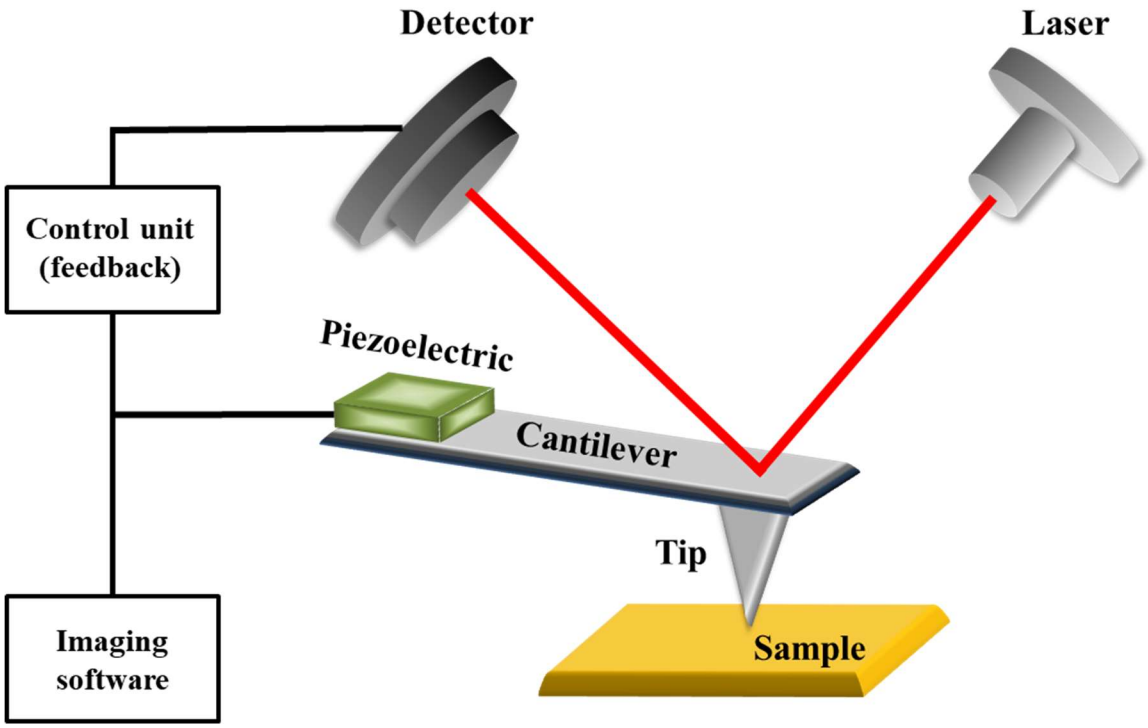

Figure 1.5. A schematic of Atomic Force Microscopy.

1.6 References

(1) Y. Kuo; J. Lu; S. Chatterjee; J. Yan; H. C. Kim; T. Yuan; W. Luo; J. Peterson, M. Gardner, ECS Transactions **2006**, 1, 447.

(2) B. H. Lee; L. Kang; R. Nieh; W.-J. Qi; J. C. Lee, Appl. Phys. Lett. **2000**, 76, 1926.

(3) W.-H. Kim; F.S.M. Hashemi; A.J.M. Mackus; J. Singh; Y. Kim; D. Bobb-Semple; Y. Fan, T. Kaufman-Osborn; L. Godet; S.F. Bent, *ACS Nano* **2016**, 10, 4451.

(4) J.A. Liddle; G.M. Gallatin, *ACS Nano* **2016**, 10, 2995.

(5) D.G. Lishan; H.F. Wong; D.L. Green; E.L. Hu; J.L. Merz; D. Kirillov; *J. Vac. Sci. Technol., B: Microelectron. Process. Phenom*. **2019**, 7, 556.

(6) C.H. Jan; U. Bhattacharya; R. Brain; S.J. Choi; G. Curello; G. Gupta; W. Hafez; M. Jang; M. Kang; K. Komeyli; T.Leo; N. Nidhi; L. Pan; J. Park; K. Phoa; A. Rahman; C. Staus; H. Tashiro; C. Tsai; P. Vandervoorn; L. Yang; J.Y. Yeh; P. Bai, *IEEE int. Electron Devices Meet.* **2012**, 3.1.1.

(7) A. J. M. Mackus; A. A. Bol; W. M. M. Kessels, Nanoscale **2014**, 6, 10941.

(8) A. J. M. Mackus; M. J. M. Merkx; W. M. M. Kessels, Chem. Mater. **2019**, 31, 2

(9) A. Mameli; M. J. M. Merkx; B. Karasulu; F. Roozeboom; W. M. M. Kessels; A. J. M. Mackus, ACS Nano **2017**, 11, 9303.

(10) F. S. M. Hashemi; S. F. Bent, Adv. Mater. Interfaces **2016**, 3, 1600464.

(11) R. Vallat; R. Gassilloud; B. Eychenne; C. Vallée, J. Vac. Sci. Technol. A **2017**, 35, 01B104.

(12) S. E. Atanasov; B. Kalanyan; G. N. Parsons, J. Vac. Sci. Technol. A **2016**, 34, 01A148.

(13) B. Kalanyan; P.C. Lemaire; S.E. Atanasov; M.J. Ritz; G.N. Parsons, *Chem. Mater.* **2016**, 28, 117.

(14) D. Seghete; G.B. Rayner Jr.; A.S. Cavanagh; V.R. Anderson; S.M. George; *Chem. Mater.* **2011**, 23, 1668.

(15) Hollander, J. M.; Jolly, W. L. *Accounts of chemical research* **1970**, *3*, 193.

(16) Nogi, K.; Naito, M.; Yokoyama, T. *Nanoparticle technology handbook*; Elsevier, 2012.

(17) Binnig, G.; Rohrer, H. *Surface science* **1983**, *126*, 236.

Chapter 2

Selective atomic layer deposition of $MoSi_x$ on Si (001) in preference to Silicon Nitride and Silicon Oxide

2.1 Abstract

Highly selective deposition of $MoSi_x$ on Si in preference to SiO_2 and SiN_x was achieved via atomic layer deposition (ALD) using MoF_6 and Si_2H_6 at 120°C. The selectivity was enabled by the lack of chemical reactivity between the reactants and the SiO_2 and SiN_x substrates. In contrast, MoF_6 nucleated in a self-limiting manner on H-terminated Si, and a following Si_2H_6 exposure reduced MoF_x to Mo^0 which is consistent with Mo-Si bond formation. X-Ray photoelectron spectroscopy (XPS) revealed that the 5 ALD cycles of MoF_6 and Si_2H_6 selectively deposited a substoichiometric $MoSi_2$ film on the Si substrate in contrast to previous results showing a nearly pure Mo deposition. Extra Si_2H_6 doses on the substoichiometric $MoSi_2$ film incorporated more Si into the film without disturbing the inherent selectivity over SiO_2 and SiN_x. A depth-profiling study showed that the bulk of the film has Si/Mo = 1.7 – 1.9 with <10% F and O impurities. The data is consistent with higher pressure Si_2H_6 doses inducing silicide formation instead of metal deposition. To verify selectivity on the nanoscale, the selective deposition of $MoSi_x$ was investigated on a patterned Si wafer containing three-dimensional (3D) nanoscale SiO_2 and SiN_x features. Cross-sectional transmission electron microscopy (TEM) showed that selective $MoSi_x$ deposition was achieved on nanoscale 3D structures. AFM documented that there were less than 10 nuclei/μm^2 on SiO_2.; since SiO_2 has ~10^6/μm^2 OH groups, this corresponds to an intrinsic selectivity of about 10^6:1 between the OH groups on SiO_2 and

Si-H groups on Si. This inherent substrate-dependent selectivity for silicide deposition allows the elimination of pre-positioning of passivants.

2.2 Introduction

Exact positioning of materials on nanoscale devices is required to manipulate atomic-scale properties for next-generation nanoelectronics [1-3]. For semiconductor fabrication, detailed positioning of materials with excellent conformality and stoichiometry is required to meet the demand for cost, yield, and throughput [4]. As metal-oxide-semiconductor field effect transistors (MOSFETs) are scaled to less than <10 nm channel length, there is a need to overcome the constraints originating from top-down processes such as damage from reactive ion etching and structural complexity in alignments on three-dimension (3D) surfaces [3-6].

Recently, as MOSFET devices have been fabricated in 3D structures (FinFETs), there has been increasing interest in area-selective deposition on the nanoscale while maintaining conformal film quality since area-selective atomic layer deposition (ALD) eliminates patterning steps and complexity particular to 3D devices such as lithography onto 3D structures [6]. It has been demonstrated that selective ALD can be accomplished using self-assembled monolayers (SAMs) as passivation layers [7-9]. The passivation layers block or eliminate surface functional groups that are reactive towards ALD precursors so that selectivity can be obtained; however, this necessitates the selective deposition of the passivation layer. Furthermore, often the passivation layers must be selectively removed after the selective deposition [10]. Therefore, an alternative method to obtain selectivity has been suggested which is to utilize substrate-dependent reactivity of

ALD precursors [11-14]. B. Kalayan et al.[14] reported the intrinsic substrate-dependent selectivity of W metal deposition on Si over SiO_2 using WF_6 and SiH_4. The inherent substrate selectivity was ascribed to only H-terminated Si readily being reactive to WF_6(g) to form SiF_4(g) products since Si-O bonds are stable enough not to be attacked by WF_6 [13,24]. B. Kalayan et al. suggested that by adding a H_2 carrier gas with WF_6 during the deposition process, the selectivity window (number of ALD cycles over which selectivity is retained) could be improved. It was hypothesized that the ALD by-product HF passivated the –OH nucleation sites on SiO_2 in the form of SiO_xF_y which is not reactive towards WF_6.

Transition metal disilicides such as $TiSi_2$, $CoSi_2$ and $MoSi_2$ are capable of reducing the electrical resistance at the contact regions and tuning the contact work function in MOSFETs [15,16]. It is important to reduce the parasitic resistance since the performance of scaled devices with <10 nm channel length can be strongly affected by parasitic resistance. The conventional methods to form silicides involve a high temperature anneal after metal deposition onto Si or by direct deposition of silicides using evaporation or co-sputtering [17]. These methods readily form silicides of the desired stoichiometry, but they may not be applicable to complicated 3D structures due to the Si consumption, poor step coverage and insufficient thickness control for scaled devices. There have been several studies on W or Mo metal ALD using WF_6 or MoF_6 and SiH_4 or Si_2H_6 but little is documented on ALD of silicide [14,18]. K. Bernal-Ramos et al. carried out $CoSi_2$ ALD on H-terminated Si (111) at 140°C using an organometallic Co precursor (^{t}Bu-AllylCo(CO)$_3$) and trisilane (Si_3H_8) [19]. NbSi deposition was achieved by T. Proslier et al. using NbF_5 and Si_2H_6 at a deposition temperature of 150 – 400°C [20]. Using MoF_6 and Si_2H_6 as the reactants, D. Seghete et al. studied the nucleation and growth characteristics of Mo metal

ALD between 90–150°C using a quartz crystal microbalance [18]. It was hypothesized that Si_2H_6 acts as a sacrificial reducing agent for MoF_6 and leaves reduced Mo metal as a final product which was previously suggested in W metal ALD or CVD using WF_6 and SiH_4 [14,28]. While the inherent selectivity of metal deposition on Si over thermally grown pristine SiO_2 was previously reported using MoF_6 or WF_6, in 3D architectures (FinFETs), selective silicide growth on Si over SiO_2 as well as SiN_x or SiON which are ion damaged is also required. Selective silicide deposition on Si over ion damaged SiN_x or SiON is a critical challenge in 3D nanostructures.

The objective of the present study is to quantify on the nanoscale the selective deposition of $MoSi_x$ on Si in preference to SiO_2, SiON and SiN_x using the inherent substrate selectivity of MoF_6 and Si_2H_6. The selectivity on planar samples was quantified with X-ray photoelectron spectroscopy (XPS) as well as atomic force microscopy (AFM) in order to count the number of unwanted nuclei on SiO_2, while the selectivity on 3D nanoscale structures was probed by both XPS and transition electron microscopy (TEM). To achieve stoichiometric $MoSi_2$, additional Si insertion after the ALD cycles was performed by dosing Si_2H_6 onto the Mo rich $MoSi_x$ film. The resistivity of the $MoSi_x$ film was obtained by using 4-probe electrical measurements.

2.3 Experimental

Four types of samples were employed: P-type Si (100) (Boron-doped, Virginia Semiconductor), thermally grown SiO_2 on Si (100) (University Wafer), SiON (Applied Materials) and patterned samples having Si, SiO_2 and SiN_x. The SiON in this study is Si_3N_4 which has been subjected to reactive ion etching and plasma ashing in oxygen during

fabrication, and therefore contains oxygen; this mimics the conditions of Si_3N_4 after processing in integrated 3D nanoscale devices. The samples were diced into 12 mm × 3 mm pieces and degreased with acetone, methanol and deionized (DI) H_2O. The native oxide on Si was removed by immersing the degreased samples into a 0.5% HF(aq) solution for 30 seconds. For consistency in cleaning procedure, the SiO_2, SiON and patterned samples were subjected to the same cleaning procedure. The samples were blow-dried using high purity N_2 gas. Two or three samples out of the Si, SiO_2, SiON and patterned sample were loaded together on a single sample holder to expose the samples to the same ALD conditions. The samples were loaded into a load lock chamber pumped by a turbo molecular pump and backed by a mechanical pump. The base pressure of the load lock was ~2.0×10^{-7} Torr. Subsequently, the samples were transferred in-situ to an ultra-high vacuum chamber with a base pressure of ~3.0×10^{-10} Torr pumped by an ion pump and titanium sublimation pump. The ultra-high vacuum chamber was equipped with a monochromatic XPS (XM 1000 MkII/SPHERA, Omicron Nanotechnology), STM (Omicron Nanotechnology) and annealing system using a pyrolytic boron nitride (PBN) heater.

The samples were first annealed at 120°C in the ultra-high vacuum chamber and the chemical composition of the samples were determined using XPS. Afterwards, the samples were transferred in-situ to a home-made reaction chamber having a base pressure of ~5.0×10^{-7} Torr. For $MoSi_x$ deposition, MoF_6 (Synquest Laboratories, 99%) and Si_2H_6 (Air Liquide, 99.99%) precursors were employed.

During the ALD cycles, a constant purge of N_2 (80 mTorr) was used, and the pressure of this purge was controlled using a leak valve. The MoF_6 and Si_2H_6 doses were regulated using pneumatic valves controlled by a LabView program. An expansion volume

was employed for the MoF_6 and Si_2H_6 doses. This consisted of filling a secondary volume with MoF_6 or Si_2H_6 and dosing the precursors from their respective secondary volumes. The fill/dose times for the MoF_6 were 40ms/50ms and for Si_2H_6 the fill/dose times were 18ms/18ms. The exposures of MoF_6 and Si_2H_6 were calculated in terms of Langmuirs (L) where 1 L = 1×10^{-6} Torr × 1 sec. The pressure spikes during the exposures were monitored using a Convectron gauge in the reaction chamber. The doses were 1.8 MegaL for MoF_6 and 4.2 MegaL for Si_2H_6 with a 2-minute wait time between the doses. The samples were heated using a pyrolytic boron nitride (PBN) heater, and the temperature was maintained at 120°C. The chamber walls were maintained at 80°C. After the deposition cycles, the samples were transferred in-situ to the ultra-high vacuum chamber for XPS and STM. For the XPS measurement, the X-rays were generated by an Al Kα anode (1486.7 eV). XPS data was acquired using constant analyzer-energy (CAE) with a step width of 0.1 eV and a pass energy of 50 eV. The XPS detector was at 60° to the sample normal (30° take-off angle from the sample surface) with a detector-acceptance angle of 7°. XPS spectra were analyzed after correcting each peak area with its respective relative sensitivity factor using a Casa XPS v.2.3 program. All of the chemical components in this work were normalized to the sum of all components. STM was performed with a sample bias of -1.8 V and a constant current of 200 pA.

To investigate the elemental composition of the bulk of the film, Ar^+ sputtering was performed in conjunction with XPS. A lens voltage of 5kV with a beam current of 1.2 μA at 6.0×10^{-7} Torr of Ar was employed; since a raster was used to cover the full sample area, the current density was approximately 1.2 uA/50 mm^2. The $MoSi_x$ sample was maintained

at 25°C during sputtering to minimize any thermal desorption of SiH_xF_y or SiF_4 compounds from the surface.

2.4 Results and Discussion

2.4.1 XPS of MoF_6 and Si_2H_6 saturation on Si and selectivity in preference to SiON

Fig. 2.1(a) shows the XPS chemical composition of the HF cleaned Si surface before and after sequential doses of MoF_6 and Si_2H_6 at 120°C (note: the raw XPS spectra are presented in the supplement). After the HF clean, all the Si was in an oxidation state of 0 with 9% O and 12% C contamination which was most likely due to adventitious hydrocarbon adsorption during the sample transfer into vacuum. HF(aq) is known to eliminate native oxide on Si and leaves the Si surface H-terminated [21]. Note that the yellow bars (Si 2p) in Fig. 2.1 indicate the total amount of Si while the gray bars (Si (0)) indicate the amount of Si which is in an oxidation state of 0 (Si^0). The amount of Mo^0 (Mo (0), the purple bars) and the total amount of Mo (Mo 3d, the pink bars) were also plotted separately to emphasize the amount of pure $MoSi_x$. After the 5.4 MegaL of MoF_6 at 120°C, 14% Mo and 38% F were deposited on the HF cleaned Si surface. After an additional 5.4 MegaL of MoF_6 at 120°C were dosed, the Mo concentration increased from 14% to 16% and the F concentration increased from 38% to 42%. This small increase in Mo and F content after an additional 5.4 MegaL of MoF_6 shows that the reaction of MoF_6 on HF cleaned Si is self-limiting. (Also see Fig. 2.14) After the Si surface was saturated with MoF_x, the ratio of F/Mo was 2.6 and all of the Si was in an oxidation state of 0. Sequential doses of 4.2 MegaL of Si_2H_6 and 42 MegaL of Si_2H_6 indicate that the Si_2H_6 reaction also saturates on the MoF_x covered Si surface. It is shown below that with a thicker sub-

stoichiometric $MoSi_2$ film, additional Si can be forced onto the surface. However, the Si_2H_6 reacts in a self-limiting manner on a thinner (monolayer) film of Mo. After saturation of Si_2H_6, the Si content was 59% and F decreased to 10%. Since the substrate is Si, this increase of the Si content after dosing Si_2H_6 could be partially ascribed to the substrate since F desorption occurred in the form of SiH_xF_y or SiF_4. However, attenuation of the Mo after Si_2H_6 dose was observed which is consistent with the deposition of Si. The deposition of Si was also demonstrated by previously published studies using WF_6 and Si_2H_6 or MoF_6 and Si_2H_6 chemistry [14,18]. The half cycles of Si_2H_6 dosed onto a WF_6 or MoF_6 saturated surface; for the Mo chemistry, the reaction was described as:

$$MoF_5^* + Si_2H_6(g) \rightarrow MoSiH_xF_{3-x}{}^* + SiH_{2-x}F_{2+x}(g) + 2H_2(g) \text{ (x} = 0, 1 \text{ and } 2)$$

where the asterisks indicate surface species. The authors pointed out that the subsequent WF_6 or MoF_6 doses react with the deposited SiH_xF_y species to form W or Mo metal again.

The reaction of MoF_6 and Si_2H_6 on H-terminated Si demonstrates the potential for $MoSi_x$ ALD on Si-H terminated Si; conversely, for the same series of MoF_6 and Si_2H_6 saturation doses on SiON, no reaction was observed. (see Fig. 2.1(b)). It should be noted that while this sample was nominally SiON, XPS showed only negligible amounts of N on the surface and so this sample is mostly ion damaged SiO_x. After the first 3 pulses of MoF_6, 8% F and negligible Mo (<1%) were observed. For the rest of the saturation doses, the SiON surface remained unreactive to both MoF_6 and Si_2H_6. This inherent chemical selectivity of SiO_2 (not SiON) was reported earlier using WF_6 and SiH_4 for W metal ALD on Si vs. SiO_2 [13,14,23]. Kalanyan et al. used SiH_4 as a sacrificial reducing agent for W deposition, and the substrate dependent selectivity was explained by the thermodynamically unfavorable reaction between WF_6 and stable Si-O bonds of pristine

SiO_2. A similar mechanism is consistent with the selectivity of MoF_6 and Si_2H_6 on Si vs. SiON despite Si_2H_6 being more reactive than SiH_4 and SiON being a less stable film than SiO_2. While the SiON used in this study is ion damaged, the Si is in oxidation states of +3 and +4 and the data is consistent with these strong Si-O, Si-N, SiO-H bonds precluding the Si from forming bonds to Mo. (see Fig. 2.10). DFT models by Kwon et al. show that the stronger SiO-H bond compared to Si-H can raise the activation barrier and enthalpy of reaction for ALD [30].

In Fig. 2.2, the XPS spectra of Si 2p and Mo 3d for the HF cleaned Si sample are shown to compare the oxidation states at each experimental step. After the first 5.4 MegaL of MoF_6, the Si 2p peak remained at an oxidation state of 0 which is consistent with Si-Mo bond formation. The Mo 3d peaks appeared at multiple oxidation states which indicates that the surface species are MoF_x with x = 4, 5 and 6. (black line) The additional 5.4 MegaL of MoF_6 did not change the oxidation states of the Si 2p or the Mo 3d peaks. (blue line) These results are consistent with the formation of Si-Mo-F_x at the surface. It is noted that the F/Mo ratio was 2.6 after the MoF_6 saturation dose from XPS. (Fig. 2.1(a)) while the Mo is in oxidation states of 4-6; therefore, it is possible that there is some Mo-O bond formation. A small shoulder peak at a higher binding energy (103 eV) on the Si 2p XPS peak appeared after a 4.2 MegaL of Si_2H_6 dose. (red line) This is consistent with Si-F or Si-O formation. The Mo 3d spectra shows that after a single Si_2H_6 dose, all of the Mo is reduced to Mo^0 with a binding energy of 227.4 eV. This is consistent with the formation of a monolayer of $MoSi_x$ and the transfer of any residual oxygen or fluorine from Mo to Si in the form of Si-O and Si-F bonds. A possible simplified reaction of MoF_6 and Si_2H_6 could be described as:

$$MoF_6(g) + 1.5Si_2H_6(g) \rightarrow MoSi_2(s) + SiF_4(g) + 3.5H_2(g) + 2\text{HF(g)}$$

2.4.2 Selectivity of $MoSi_x$ in preference to SiO_2 and stoichiometry

ALD characteristics of $MoSi_x$ on the Si substrate and the inherent selectivity over the SiO_2 and SiN_x substrates were verified via XPS of $MoSi_x$ deposition on a patterned sample. Fig. 2.3 shows the chemical composition of a set of three samples: HF cleaned Si, HF cleaned SiO_2 and HF cleaned patterned sample (note: the raw XPS spectra are presented in Fig. 2.12). The three samples were loaded together on a single sample holder to ensure that they were exposed to identical deposition conditions. The Si and SiO_2 samples allowed verification of selectivity during deposition on the patterned sample. The patterned sample had SiO_2 layers sandwiched by SiN_x on top of the Si substrate as shown in Fig. 2.3(d). It is noted that the SiN_x on the patterned sample was actually SiON since it was ion damaged and ashed in O_2 during fabrication. As shown in Fig. 2.3(a), a 30 s HF clean removed the native oxide on Si. The thermally grown SiO_2 was 300 nm thick and so the 30 s of HF clean did not change the elemental composition or oxidation states of SiO_2. The HF cleaned patterned sample showed a mixture of SiN_x, SiO_x and Si^0. Even though there were Si and SiO_2 samples loaded together to monitor the selectivity of the patterned sample, the blanket films might not be the same as 3D nanostructure features due to the high aspect ratio as well as damage from the patterning processes. Employing a patterned sample in XPS allowed selectivity determination on the nanoscale on realistic surface because the Si^0 component could be distinguished from SiO_2 or SiN_x from XPS. If $MoSi_x$ was deposited selectively on the patterned sample, it was expected that only the attenuation of this Si^0 component from the mixture of SiO_2 and SiN_x would be observed. (See Fig. 2.12)

XPS was performed after 5 ALD cycles of MoF_6 and Si_2H_6 at 120°C as shown in Fig. 2.3(b). XPS showed a surface composition of 32% Mo and 10% Si with 39% F on the Si sample which shows a MoF_x rich surface. This is in contrast to a surface closer to $MoSi_2$ after the first ALD cycles. Even though a monolayer of $MoSi_2$ was able to be deposited on Si in the ALD saturation experiments described in Fig. 2.1 and Fig. 2.2, consecutive ALD cycles did not produce stoichiometric $MoSi_2$. The formation of Si deficient $MoSi_x$ could be due to the surface SiH_xF_y species desorbing during the fluorosilane elimination process and due to residual Mo-F bonds which are not readily removed by standard Si_2H_6 dosing [18,20,22]. For the first 1-3 monolayers, there is an excess of Si from the substrate present to assist in fluorine desorption in the form of SiH_xF_y or SiF_4, but for thicker films Mo-F surface bonds may persist since the only available Si is from the gaseous Si_2H_6. The overall fluorosilane elimination chemistry using MoF_6 and Si_2H_6 is consistent with one of two chemical reactions:

$$MoF_6(g) + Si_2H_6(g) \rightarrow Mo(s) + 2SiHF_3(g) + 2H_2(g)$$

or

$$2MoF_6(g) + 1.5Si_2H_6(g) \rightarrow 2Mo(s) + 2SiF_4(g) + SiHF_3(g) + 3.5H_2(g) + 2HF(g)$$

It is noted these processes are limited to the first 1-3 monolayers, since cross sectional TEM studies of the patterned sample shows Si substrate depletion of about 1 nm. For the ALD cycles remote from the surface, the depth profile studies below show that the MoF_x is just a surface layer and not a bulk film. There was no $MoSi_x$ deposition on the SiO_2 substrate consistent with highly selective ALD. On the patterned sample, XPS showed that 5% Mo was deposited, and the Si^0 was attenuated to 1%. (The raw XPS peaks are shown in Fig. 2.12(c)) The fraction of N and O at the surface did not change significantly during ALD

on the pattern sample. The data is consistent with Si-deficient $MoSi_x$ being deposited selectivity on the 6% of Si^0 (The grey bar in Fig. 2.3(a)) on the patterned sample. This selectivity on the pattern samples is consistent with three aspects of the XPS study: (1) There was $MoSi_x$ deposition on the Si sample but not on the SiO_2 sample. (2) After the $MoSi_x$ deposition, only the Si^0 (not the higher oxidation state Si peaks from Si-N and Si-O) was attenuated on the pattered sample. (3) Numerically, ~4% Mo deposition on the patterned sample with 6% Si^0 is proportional to having 32% Mo on the Si sample with 54% Si^0 on the HF clean surface.

To form $MoSi_2$, the three samples were exposed to an additional 25.2 MegaL (6 pulses) of Si_2H_6 at 120°C. (Fig. 2.3(c)) After the extra Si_2H_6, Si increased to 20% on the Si substrate consistent with Si being incorporated into the film or on the surface. These extra Si_2H_6 doses did not decrease the selectivity for deposition on Si versus SiO_2.

2.4.3 Post deposition anneal effect on $MoSi_x$ composition

The substrate selectivity of the $MoSi_x$ deposition with respect to SiON along with the effect of post deposition anneal on film composition were investigated. It should be noted that this SiON is actually Si_3N_4 which has been ashed with an O_2 plasma and so this models patterned sample sidewalls after RIE etching. The SiON was loaded into the chamber along with Si and SiO_2 for calibration. Fig. 2.4(a) shows that the SiON surface is composed primarily of SiN_x after the HF clean. After the 5 cycles of $MoSi_x$ ALD followed by an additional 25.2 MegaL of Si_2H_6, there was 24% Mo and 18% Si on HF cleaned Si while less than 1% Mo was detected on the SiO_x and SiN_x surfaces as shown in Fig. 2.4(b) (Note, the raw XPS spectra are presented in the supplement). Subsequently, the three

samples were annealed at 520°C for 3 mins which decreased F from 25% to 3% on the Si substrate. The 520°C PDA also reduced all of the Mo to Mo^0 on the Si substrate and decreased the Si/Mo ratio from 0.75 to ~0.5 at the surface. This is consistent with the desorption of surface F in the form of $SiHF_3$ or SiF_4. The XPS analysis of the high temperature anneal indicates that the F could be removed from the film by the post anneal which may be needed for practical application in MOSFETs [25-27].

2.4.4 Topography of the $MoSi_x$ film and selectivity

Using an in-situ STM and ex-situ AFM, the surface topographies were investigated after the deposition and the high temperature anneal on the Si and SiO_2 samples. A separate sample of HF cleaned Si after 20 cycles of MoF_6 and Si_2H_6 was prepared for the in-situ STM. Fig. 2.5(a) shows the STM image of $MoSi_x$/HF cleaned Si sample. The $MoSi_x$ film was atomically flat and conformal with an RMS roughness of 2.8 Å. This sample was annealed in-situ at 500°C for 3 mins in the ultra-high vacuum chamber at a pressure of ~5.0×10^{-10} Torr. After the 500°C anneal, the film became flatter with an RMS roughness of 1.7 Å shown in Fig. 2.5(b). There was no agglomeration at the surface. Another sample of $MoSi_x$/HF cleaned Si after 5 ALD cycles at 120°C followed by an in-situ 550°C anneal was taken into an ex-situ furnace for a 900°C spike anneal in 5% H_2 balanced with N_2. After the 900°C spike anneal, AFM was used to obtain the surface morphology. The film retained a sub-nanoscale RMS roughness of 4.75 Å demonstrating that the $MoSi_x$ film has very good thermal stability up to 900°C. (see Fig. 2.5(c))

Fig. 2.5(d) shows an ex-situ AFM image of the SiO_2 surface after dosing 5 ALD cycles at 120°C followed by an in-situ 550°C anneal for 3 minutes in order to confirm the

selectivity by counting the number of nuclei on the surface. The density of nuclei was 9 nuclei/μm^2 which confirms the very good selectivity over SiO_2. P.C. Lemaire et al. [13] studied the relationship between inherent substrate selectivity and hydroxyl density during tungsten (W) ALD using WF_6 and SiH_4. They reported that an increase in the surface OH density on SiO_2 provokes earlier nucleation of W on SiO_2 (selectivity loss) via a reaction of W-ALD reactants with the surface hydroxyls. The authors also stated that pre-dosing the Si-OH terminated SiO_2 with SiH_4 induces earlier W nucleation by forming a Si monolayer on SiO_2. In present study, Si_2H_6 was employed which is more reactive than SiH_4 due to the weak Si-Si bond; therefore it is likely that Si_2H_6 will react with Si-OH sites on SiO_2 above a threshold exposure. To estimate the selectivity of $MoSi_x$ deposition between H-terminated Si versus OH terminated SiO_2, the surface OH density of the thermally grown SiO_2 was assumed to be ~2 OH/nm^2 as reported by R. Mueller et al. [29] Assuming $MoSi_x$ deposition on H-terminated Si was 100%, there were only ~10 nuclei/μm^2 out of ~2×10^6/μm^2 (2 OH/nm^2) hydroxyls on SiO_2 which is consistent with more than 10^6 selectivity between Si-H groups and hydroxyls on SiO_2. Parson et al.[14] reported for the ALD of W using WF_6 and S_iH_4, ~450 nuclei/um^2 after 30 cycles of W ALD which is about 50× greater than in the present study. There are one two previous reports of similar selectivity for any selective ALD or CVD process. Chang et al.[24] studied the CVD of W by a mixture WF_6+H_2+SiH_4 and measured the W particles on SiO_2; while they observed a low particle density (20 particles/cm^2), the particles were ~2 μm^2 in size and therefore at least 10^3 larger is mass than the particles in the present study (~1.4×10^{-3} μm^2 in size with ~2 nm height). The high selectivity in the present study is consistent with careful control

of wall temperature and using short high pressure Si_2H_6 pulses and longer purge cycles to avoid CVD.

2.4.5 Depth profile XPS in conjunction with Ar^+ sputter

A depth profile study was performed to determine the internal composition of the $MoSi_x$ film. Fig. 2.6 (a) shows XPS of $MoSi_x$/HF cleaned Si after sequential sputtering experiments (Addition raw XPS spectra are presented in the supplement). The $MoSi_x$ film was deposited on HF cleaned Si at 120°C using 5 ALD cycles of MoF_6 and Si_2H_6 without additional Si_2H_6 incorporation. As the sputtering time increased, the $MoSi_x$ film became thinner until the underlying Si substrate was exposed. The first 10 mins of sputtering decreased the F from 35% to 8% while the Mo shifted from a mixture of oxidized Mo and Mo^0 to pure Mo^0. The data is consistent with the surface F being bonded primarily to Mo. Following consecutive sputtering cycles, the amount of Si increased and the amount of Mo decreased. Furthermore, the amount of Si^0 (gray bars) increased together with the total Si (yellow bar) and reached a maximum at 43% after 100 mins of a total sputtering time. The Si^0 to Mo^0 ratio was employed to distinguish the pure $MoSi_x$ phase because as shown by Wagner et al. as well as Brainard and Wheeler in the pure $MoSi_x$ phase, both Mo and Si are bonded to each other and have an oxidation state of 0 consistent with minimal charge transfer between Mo and Si in the silicide. [32,33] After removal of the silicon oxide and MoF_x species at the surface, the percentage of Si^0 exceeded that of Mo^0. The Si^0:Mo^0 ratio in the bulk of the $MoSi_x$ film was 1.41 which corresponds to a Si-deficient $MoSi_x$ film. It is noted that in the center of the film the Si/Mo ratio is 1.77 therefore, in the absence of background O_2/H_2O, it is possible the Si^0:Mo^0 ratio would be closer to 2.

Fig. 2.6 (b) shows the raw XPS spectra of Si 2p corresponding to each XPS measurement in Fig. 2.6 (a). The Si peak at 99.2 eV increased and broadened to higher binding energy after the 4th sputtering cycle. In contrast, the energy of the of Mo peak corresponded to Mo^0 after each sputtering cycle. (Fig. 2.11) The data is consistent with the bulk $MoSi_x$ film being mostly Si^0 and Mo^0 in the form of $MoSi_x$ while the top surface and the bottom interface was rich in SiO_x. The top SiO_x is consistent with contamination from the chamber environment while the bottom interfacial oxide is consistent with the imperfect ex-situ HF clean. The sub-stoichiometric oxide at the bottom interface did not affect the deposition and film quality indicating that the inherent selectivity of the $MoSi_x$ ALD is sensitive to the quality of the SiO_2. Fig. 2.6 (c) shows the percentages of the chemical components obtained from the XPS measurement in Fig. 2.6 (a). After the 2nd sputtering cycle (40 mins of total sputtering time), F decreased to below 3% and eventually reached 0%. O in the bulk of the film was <10% but slowly increased to 15% at the $MoSi_x$-Si interface which is consistent with the existence of an interfacial oxide layer.

2.4.6 Incorporation of Si_2H_6 for stoichiometry using depth profile XPS

To understand the effect of the additional Si_2H_6 doses on the Si/Mo ratio of $MoSi_x$ film, XPS depth profiling was performed on a $MoSi_x$ film which had the additional Si incorporation. An additional 6 pulses (25.2 MegaL) of Si_2H_6 were dosed at the end of the 5 ALD cycles of MoF_6 and Si_2H_6 at 120°C followed by an anneal at 530°C for 3 mins on dry cleaned Si. This dry clean process uses a downstream plasma of NF_3 and NH_3 with Ar as a carrier gas [31]. Fig. 2.7(a) presents a series of depth-profile XPS after each experimental step. After the 6×Si_2H_6/5ALD cycles, there were 28% F, 20% Si, and 28%

Mo at the surface. F on the surface was mostly removed after the 530°C anneal and the Mo was all reduced to Mo^0 which was consistent with the desorption of F in the form of SiH_xF_y or SiF_4 from the surface as presented in Fig. 2.4(c). The Si/Mo ratio was 0.89 at this step. In comparison, the Si/Mo ratio of the $MoSi_x$ film without the extra Si_2H_6 doses was only 0.33. (see Fig. 2.7(b)) After removing the surface oxide contamination, the Si^0/Mo^0 in the bulk was 1.32 (Si/Mo = 1.96) for $MoSi_x$ with extra Si_2H_6 pulses. This was comparable to the Si^0/Mo^0 = 1.41 (Si/Mo = 1.77) in the bulk of $MoSi_x$ without extra Si_2H_6 incorporation as depicted in Fig. 2.7(c). The ratio of Si^0/Mo^0 indicates the stoichiometry of the pure $MoSi_x$ component. This is important for the electrical properties as contact materials in MOSFETs. In this context, the notation of Si^0/Mo^0 indicates the ratio between Si and Mo at oxidation states of 0; conversely, Si/Mo indicates the ratio of the total amount of Si to total amount of Mo in the film including Si and Mo atoms boned to F and O and therefore having higher oxidation states. These results are consistent with the extra Si_2H_6 pulses increasing the Si content at the Si-deficient $MoSi_x$ surface after the ALD cycles. In contrast, the Si/Mo ratios in the bulk of the $MoSi_x$ films were close to stoichiometric $MoSi_2$. Fig. 2.7(d) shows the XPS percentage of each chemical component in the function of the Ar^+ sputter time which is consistent with the $MoSi_x$ formation in bulk of the film.

Previous studies reported Si_2H_6 and SiH_4 to be sacrificial reactants to reduce metal fluorides for pure metal deposition [14,18,20,22,28]. D. Seghete et al. previously reported Mo metal deposition on Al_2O_3 using MoF_6 and Si_2H_6 at 130°C with almost complete removal of Si from the Mo metal film as determined by Auger Electron Spectroscopy (AES) [18]. Even though identical reactants were used at a very similar temperature, there was a significant difference in the Si_2H_6 dosing conditions. For pure Mo metal deposition

with minimal Si impurities, 1.5 MegaL of Si_2H_6 was introduced into a high vacuum reaction chamber for 60 s at a constant pressure of 25 mTorr using a leak valve. In the present study, 4.2 MegaL of Si_2H_6 was introduced within 6 seconds using a pneumatic valve. This is about 3 times larger Si_2H_6 exposure within 10 times shorter dosing time thus a 30× higher partial pressure during the ALD dose. The 30× higher instantaneous pressure during dosing may allow a precursor mediated Si_2H_6 chemisorption layer to remain on the surface long enough to react with the Mo to incorporate more Si into the film. This self-limiting Si CVD component can also explain the larger growth rate of $MoSi_x$ (1.2 nm/cycle) in the present study versus that of pure Mo metal (0.6-0.7 nm/cycle) at a similar process temperature. However, the possibility of the thermal decomposition of Si_2H_6 during the ALD cycles were excluded since the thermal decomposition of Si_2H_6 did not occur below 360°C. (See Fig. 2.15) It is noted that an alternative explanation is provided by D. Seghete et al.[18] which is the reaction is sufficiently exothermic that the high pressure Si_2H_6 dosing raises the surface temperature during reaction.

2.4.7 Electrical property (resistivity) of the $MoSi_x$ film

The resistance of the $MoSi_x$ film was measured using a 4-point probe measurement. For the electrical measurement, updoped Si (001) with >10000 ohm·cm resistance was used as a substrate. For the electrical measurement, 10 cycles of $MoSi_x$ ALD at 120°C was deposited on an HF cleaned intrinsic (semi-insulating) Si sample followed by an in-situ 550°C anneal for 3 minutes and a 900°C spike anneal in 5% H_2 balanced in N_2. Ni dots were deposited as a probe contact. Fig. 2.8 shows the resistance of the film versus the

current. The resistance was 110 Ohm and, using an infinite sheet approximation, the resistivity could be calculated as:

$$\rho = ktR_{max} = (4.53) \times (10 \times 10^{-7}) \times (110) = 498\ \mu\Omega cm$$

where k is a constant, t is thickness and R_{max} is the measured maximum resistance.

2.4.8 Cross-sectional TEM of a patterned sample after $MoSi_x$ selective deposition

A cross-sectional TEM study was performed on the patterned sample to confirm the selectivity of $MoSi_x$ on the nanostructured pattern. On the HF cleaned patterned sample, 5 cycles of $MoSi_x$ ALD followed by an additional 25.2 MegaL of Si_2H_6 were dosed at 120°C. The elemental composition of this sample at each deposition step is shown in Fig. 2.3 (a-c). Fig. 2.9 (a-b) presents the cross-sectional TEM images of the patterned sample before and after $MoSi_x$ deposition. The TEM image shows complete selectivity of $MoSi_x$ deposition only on Si but not on SiN_x nor SiO_2 without damaging Si substrate by etching. (See Fig. 2.9 (c-d)) The thickness of the $MoSi_x$ film deposited on Si was ~6.3 nm after the 5 ALD cycles followed by an additional 25.2 MegaL which gives a growth rate of 1.2 nm/cycle. This higher than expected growth rate was observed by D. Seghete et al.[18] and ascribed to extra Mo deposition due to the decomposition of MoF_6 from a highly exothermic reaction between MoF_6 and H-Si species. In addition, a direct reaction between the H-terminated Si substrate and MoF_6 could be also attributed to the high growth rate by consuming Si from the substrate. The reaction between the MoF_6(g) and Si(s) could be:

$$MoF_6(g) + 2Si - H(g) \rightarrow Si - MoF_2(s) + 2SiHF_3(g) + HF(g)$$

or

$$MoF_6(g) + 2Si(s) \rightarrow Si - MoF_2(s) + SiF_4(g)$$

, where Si-H(s) indicates H terminated Si surface and Si-MoF_2(s) indicates the MoF_2 surface species bonded to the Si atoms of the surface. However, extra Si_2H_6 pulses of high pressure after 5 cycles may incorporated more Si into the film which is consistent with the high growth rate because the consumption of Si from the surface on patterned samples was very small as shown in Fig. 2.9. Due to the high growth rate per cycle of $MoSi_x$ ALD, 5 ALD cycles is sufficient for contact materials. There was 2.8 nm of an interface oxide layer between the $MoSi_x$ film and the Si substrate which is consistent with the results in Fig. 2.6. This could be improved by an in-situ clean such as a plasma clean at the sample preparation step.

2.5 Conclusions

Selective atomic layer deposition of sub-stoichiometric $MoSi_2$ was achieved by an inherently selective process on hydrogen-terminated Si versus thermally grown SiO_2, ion damaged SiON, and SiN_x. This inherent selectivity is based on the favorable reactivity of MoF_6 and Si_2H_6 on H-Si but not on SiO_2 or SiN_x since Si-O, Si-N, and SiO-H bonds are strong enough that they cannot be cleaved by either precursor at 120°C. Both MoF_6 and Si_2H_6 showed self-limiting behavior which allowed deposition of a highly conformal and smooth film with a root mean square (RMS) roughness of 2.8 Å. Post-annealing in ultra-high vacuum at 500°C for 3 minutes further decreased the RMS roughness to 1.7 Å. The quality of the film was preserved even after a 900°C spike anneal in an H_2/N_2 environment which is consistent with very good thermal stability. A depth profiling XPS study revealed that the bulk of the $MoSi_x$ film is close to stoichiometric $MoSi_2$ (Si/Mo = 1.7 – 1.9) with <10% oxygen and fluorine. The surface of the $MoSi_x$ film after 5 ALD cycles showed a

highly Si-deficient $MoSi_x$ surface with Si/Mo ratio of 0.33 and this Si/Mo ratio at the surface could be improved to 0.89 by pulsing extra Si_2H_6. The selectivity of $MoSi_x$ was examined on nanoscale patterned features of SiO_2 and SiN_x. The cross-sectional TEM imaging shows that the selectivity is retained on the nanoscale and that $MoSi_x$ can be selectively deposited on Si without substrate consumption. A large growth rate of 1.2 nm/cycle allows only 5 ALD cycles to be sufficient for its purpose as a contact material. This inherently selective $MoSi_x$ deposition would obviate the need for lithography on complicated 3D MOSFET structures (FinFETs). The selectivity for Si-H bonds vs SiO-H bonds exceeds 10^6 showing that with careful choice of precursor, extreme selectivity is possible on the nanoscale even without the use additional passivation layers. The study also showed that ALD of silicide versus metal could readily be switched while retaining selectivity by changing the partial pressure during the ALD pulse of the reductant.

2.6 Acknowledgements

Funding support from Applied Materials is gratefully acknowledged. The electrical measurements were facilitated by the San Diego Nanotechnology Infrastructure (SDNI) which is supported by the National Science Foundation (NSF) to Nano3 (Grant ECCS-1542148).

Chapter 2, in part or in full, is a reprint of the material as it appears in the Applied Surface Science. J. Y. Choi, C. F. Ahles, R. Hung, N. Kim, and A. C. Kummel, "Selective atomic layer deposition of $MoSi_x$ on Si(001) in preference to Silicon Nitride and Silicon Oxide" Applied Surf. Sci., 2018, 462, 1008–1016. The dissertation author was the primary investigator and author of this paper.

2.7 Supplemental Materials

An experiment was performed to study the saturation behavior of MoF_6 on HF cleaned Si. Fig. 2.14(a) below shows the elemental composition of HF cleaned Si followed by different amounts of MoF_6 doses at 120°C. Mo coverages on HF cleaned Si were 12.3%, 13.9% and 15.8% after 0.25 MegaL, 5.4 MegaL, and 10.8 MegaL of MoF_6 doses respectively. Fig. 2.14(b) shows ΔMo coverage/Δdose size at each experiment corresponding to Fig. 2.14(a). Even though the Mo coverage increases as the amount of dose increases, the increase per MegaL of dose is only substantial for the 0.25 MegaL dose. Since the sizes of the dose for the next two experiments are 20 times larger, the increases of Mo coverage per MegaL of doses are negligible. This is consistent with the saturation of MoF_6.

To investigate if there was a contribution of Si_2H_6 decomposition to the growth rate, Si CVD (chemical vapor deposition) was performed on HF cleaned Si and HF cleaned SiON using Si_2H_6. Fig. 2.15 below shows the elemental composition of HF cleaned Si and HF cleaned SiON followed by Si_2H_6 doses at 360°C and 500°C. 3 MegaL of Si_2H_6 was dosed at 360°C and Si_2H_6 did not react with Si-H surface nor the SiON surface. The Si percentage went up from 76% (HF cleaned Si) to 87% (After dosing 3 MegaL Si_2H_6 at 360°C); however, this is due to reduction of C contaminants from the heating to 360°C since no change was observed on SiON. After the 10 MegaL Si_2H_6 dose at 500°C, both Si and SiN_x surfaces were completely covered with Si showing 99% Si and 98% Si respectively. This is consistent with the Si CVD by thermal decomposition of Si_2H_6. This is consistent with the absence of Si_2H_6 thermal decomposition at the deposition temperature of 120°C.

Fig. 2.16 is a cross-sectional TEM image after 20 cycles of MoF_6 and Si_2H_6 at 120°C on HF cleaned Si. The $MoSi_x$ film thickness was 17.7 nm which correspond 0.88 nm/cycle. This is smaller than the growth rate (1.2 nm/cycle) that we obtained from 5 ALD cycles followed by extra Si_2H_6 pulses. The higher growth rate for the first 5 ALD cycles is consistent with the hypothesis that the larger growth is due to the direct reaction between Si substrate and MoF_6 or from extra Si incorporation into the film after the 5 ALD cycles. The absence of substrate consumption in the cross-sectional images of the patterned samples (Fig. 2.9) implies that the substrate consumption is limited to < 1 nm.

2.8 Figures

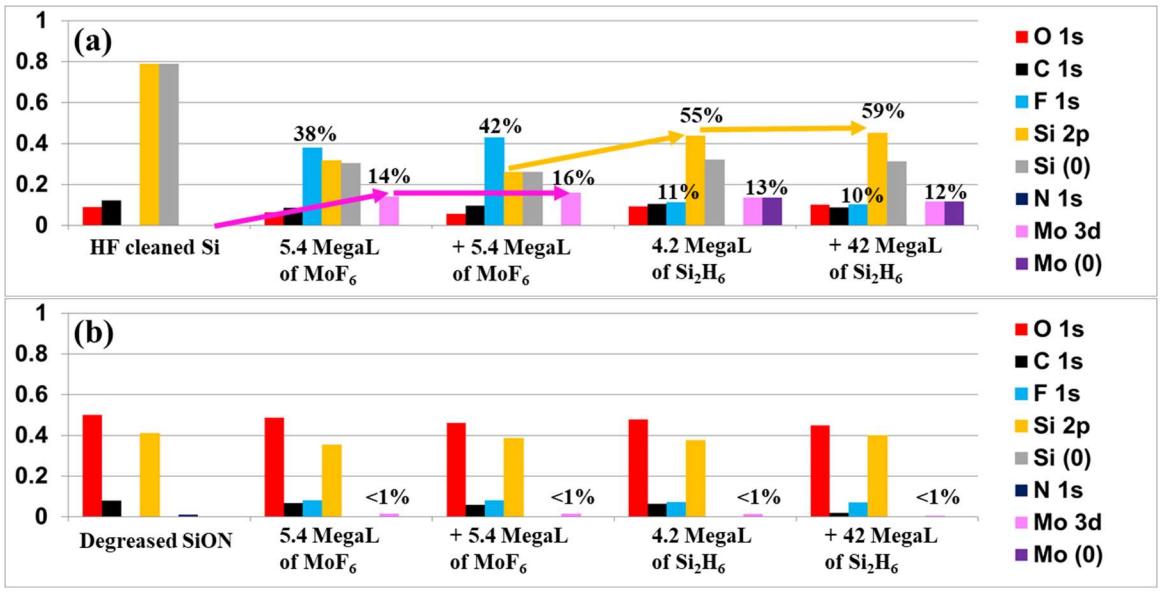

Figure 2.1. XPS of $MoSi_x$ film selectively grown on HF cleaned Si versus degreased SiON after a cycle of saturating doses of MoF_6 and Si_2H_6. (a) 2 sets of 5.4 MegaL of MoF_6 were dosed on HF cleaned Si at 120°C. XPS showed saturation of Mo at 16%. Afterward, 4.2 MegaL and an additional 42 MegaL of Si_2H_6 were dosed onto the MoF_6-saturated Si surface at 120°C; Si was saturated at 59%. (b) The same amounts of MoF_6 and Si_2H_6 were dosed on the degreased SiON at 120°C. Degreased SiON showed an inherent non-reactivity to both MoF_6 and Si_2H_6 and had <1% Mo detected on the surface.

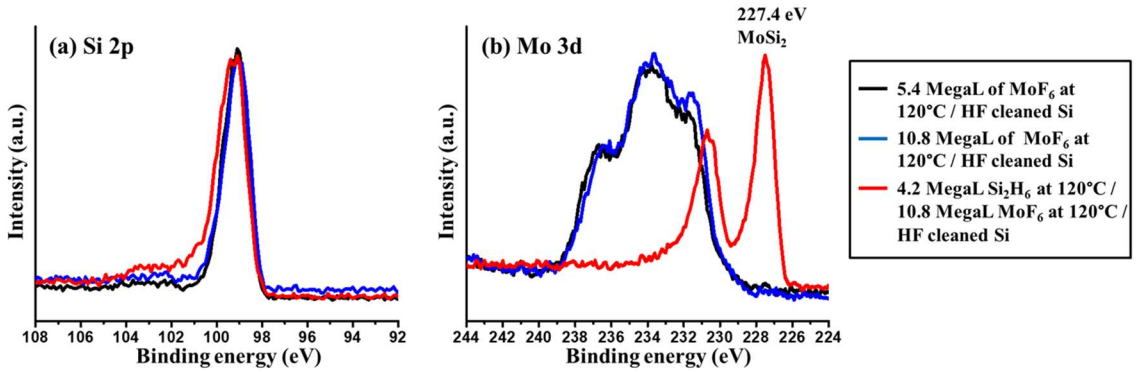

Figure 2.2 Oxidation States from XPS peaks of Si 2p and Mo 3d at each experimental step on HF cleaned Si. (a) Si 2p peaks after sequential MoF_6 and S_2H_6 doses shows that Si remained in oxidation state of 0 after the 10.8 MegaL of MoF_6 at 120°C (blue line) which is consistent with Mo-Si bond formation and no Si-F bonds being present on the surface. After the 4.2 MegaL Si_2H_6 dose at 120°C (red line), most of the Si stayed in an oxidation state of 0. This is consistent with the formation of a monolayer of $MoSi_2$. A small oxidized Si peak emerged at higher binding energies which might be SiH_xF_{4-x} (x = 2 or 3) or SiO_x at the surface. (b) Mo 3d peaks after sequential MoF_6 and S_2H_6 doses shows that the Mo 3d peaks existed in multiple oxidation states after the saturation dose of MoF_6. (black and blue line) After a Si_2H_6 dose (red line), all of the Mo was reduced and the peak was centered at 227.4 eV which is consistent with $MoSi_2$ formation.

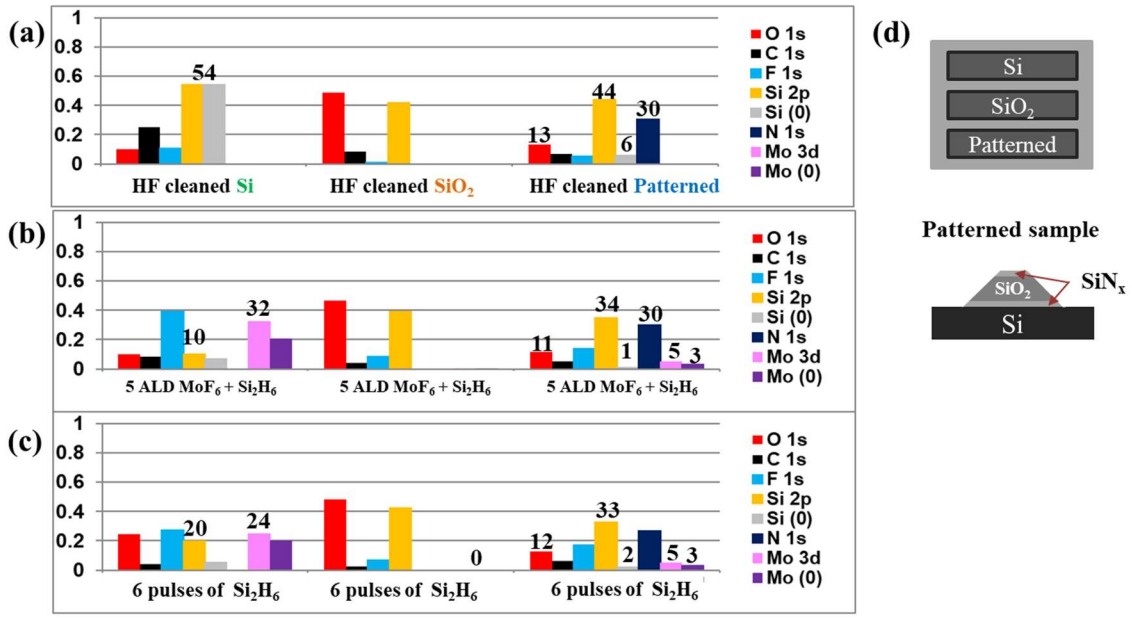

Figure 2.3. XPS chemical composition of Si, SiO_2 and a patterned sample after 5 ALD cycles of $MoSi_x$ and subsequent further Si_2H_6 dosing. (a) Chemical composition of HF cleaned Si, SiO_2 and patterned sample. (b) 5 ALD cycles of MoF_6 and Si_2H_6 at 120°C selectively deposited Si-deficient $MoSi_x$ on Si and not on SiO_2. The Si^0 component of the patterned sample was also selectively attenuated by the $MoSi_x$ deposition. (c) After an additional 25.2 MegaL (6 pulses) of Si_2H_6, more Si was incorporated onto the $MoSi_x$ surface. Selectivity with respect to SiO_2 was maintained during the additional Si_2H_6 pulses. (SiO_2 had 0% Mo and 0% Si^0 throughout the ALD process). (d) A schematic of HF cleaned Si, SiO_2 and patterned samples loaded together on a single sample holder along with a diagram of a patterned sample showing its features.

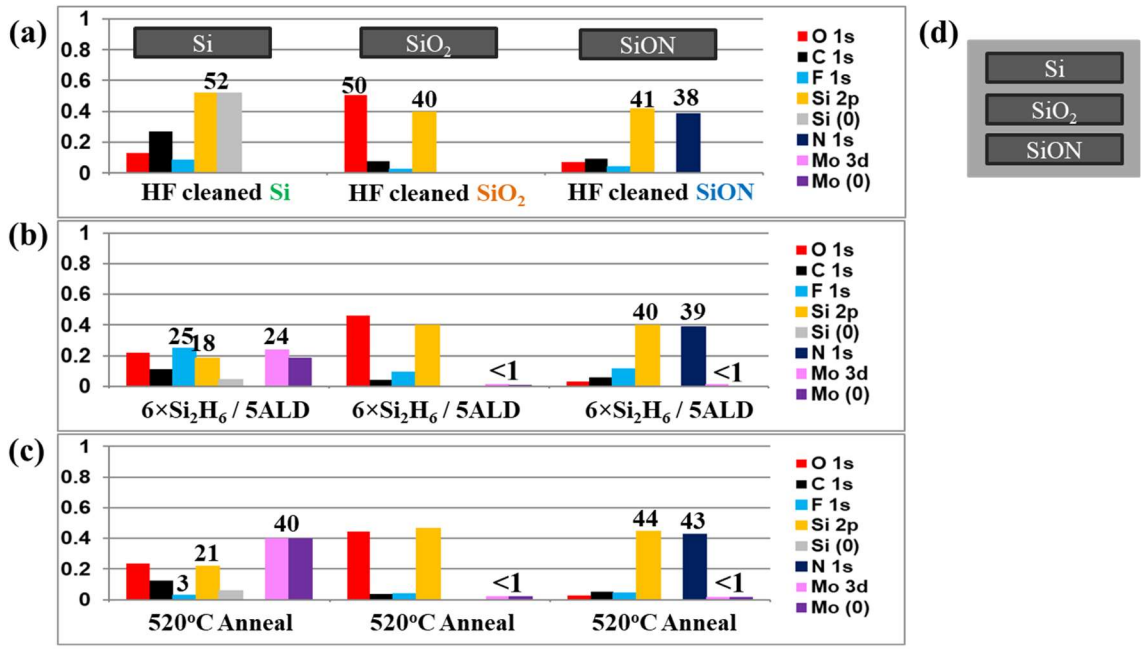

Figure 2.4. XPS chemical composition of selective $MoSi_x$ deposition on HF cleaned Si vs SiO_2 and SiON with 520°C PDA for 3 mins. (a) Chemical composition of Si, SiO_2 and SiON after the HF clean. (b) $MoSi_x$ was selectively deposited only on Si after the 5 ALD cycles of $MoSi_x$ followed by the additional 6 pulses (25.2 MegaL) of Si_2H_6 at 120°C. (c) Post-deposition anneal was performed at 520°C for 3 mins. The PDA removed F from the $MoSi_x$ film and reduced all of the Mo to Mo^0. (d) A schematic of HF cleaned Si, SiO_2 and SiON samples loaded together on a single sample holder.

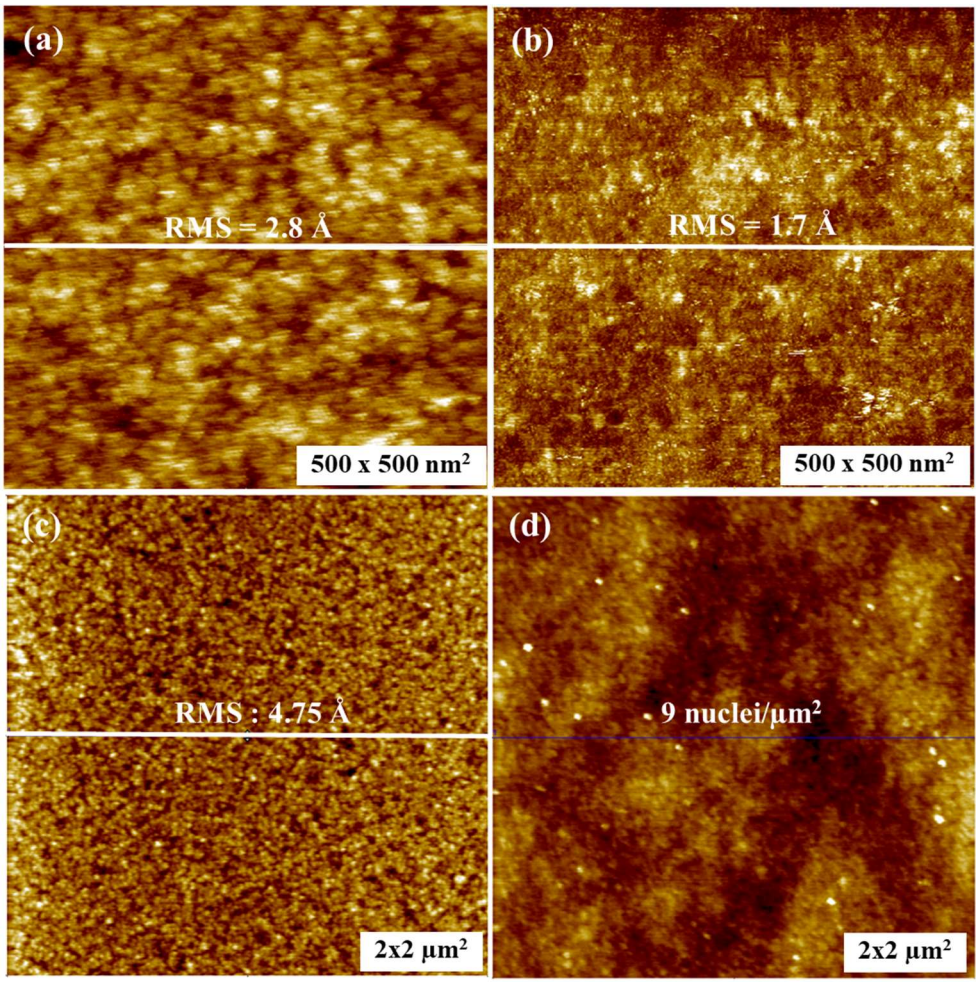

Figure 2.5. Surface morphology of Si samples after each stage of ALD and PDA and SiO_2 sample after ALD and PDA. (a) After 20 ALD cycles of $MoSi_x$ on HF cleaned Si, STM shows an atomically flat and conformal surface with an RMS roughness of 2.8 Å. (b) After the PDA at 500°C for 3 mins, the film got smoother and the RMS roughness decreased to 1.7 Å. (c) 5 cycles of $MoSi_x$ ALD on HF cleaned Si was subjected to the in-situ 550°C anneal followed by an ex-situ spike anneal at 900°C. The film did not show agglomeration, and the RMS roughness was 4.75 Å which demonstrates the thermal stability of the $MoSi_x$ film. (d) AFM image of SiO_2 showed only a few $MoSi_x$ nuclei on the surface after the 5 cycles of MoF_6 and Si_2H_6 at 120°C followed by the 550°C anneal for 3 mins which is consistent with the high selectivity.

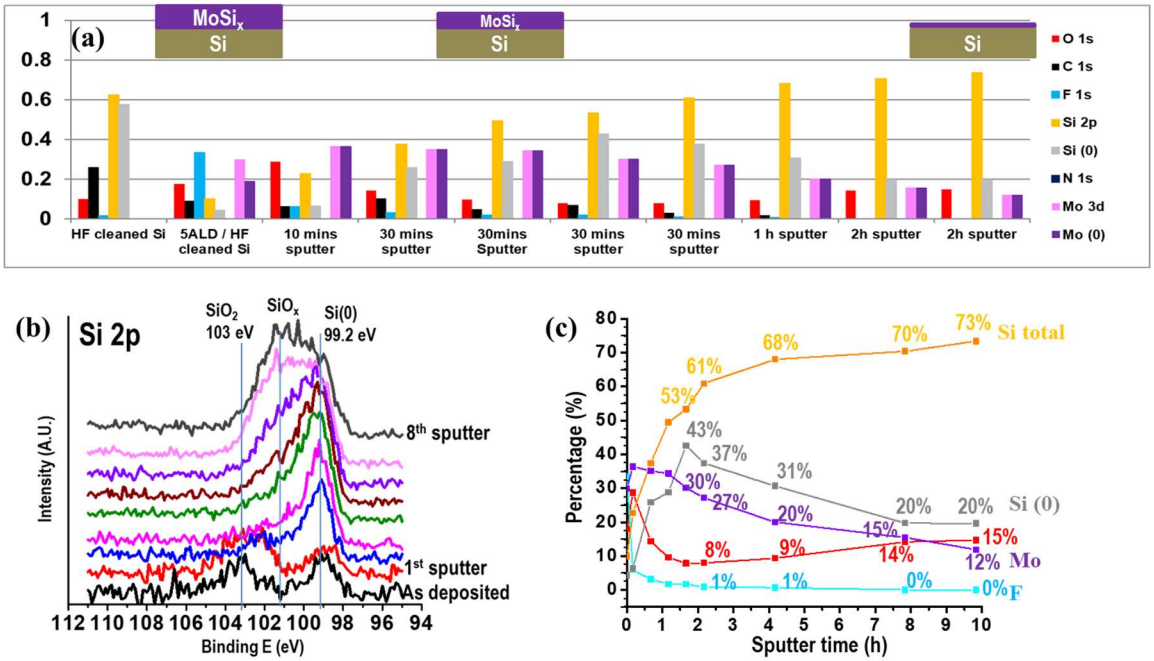

Figure 2.6. Depth profiling XPS study of the $MoSi_x$ film. (a) A series of Ar^+ sputtering experiments were performed in conjunction with XPS on HF cleaned Si after the 5 cycles of MoF_6 and Si_2H_6 at 120°C. (b) XPS peaks of Si 2p after sequential Ar^+ sputtering shows that the bulk of the $MoSi_x$ film consisted mostly of Si^0. (c) The chemical composition of the film is plotted versus Ar^+ sputter time on Si after 5 cycles of MoF_6 and Si_2H_6 at 120°C. A lens voltage of 5kV with a beam current of 1.2 μA at 6.0×10^{-7} Torr of Ar was employed.

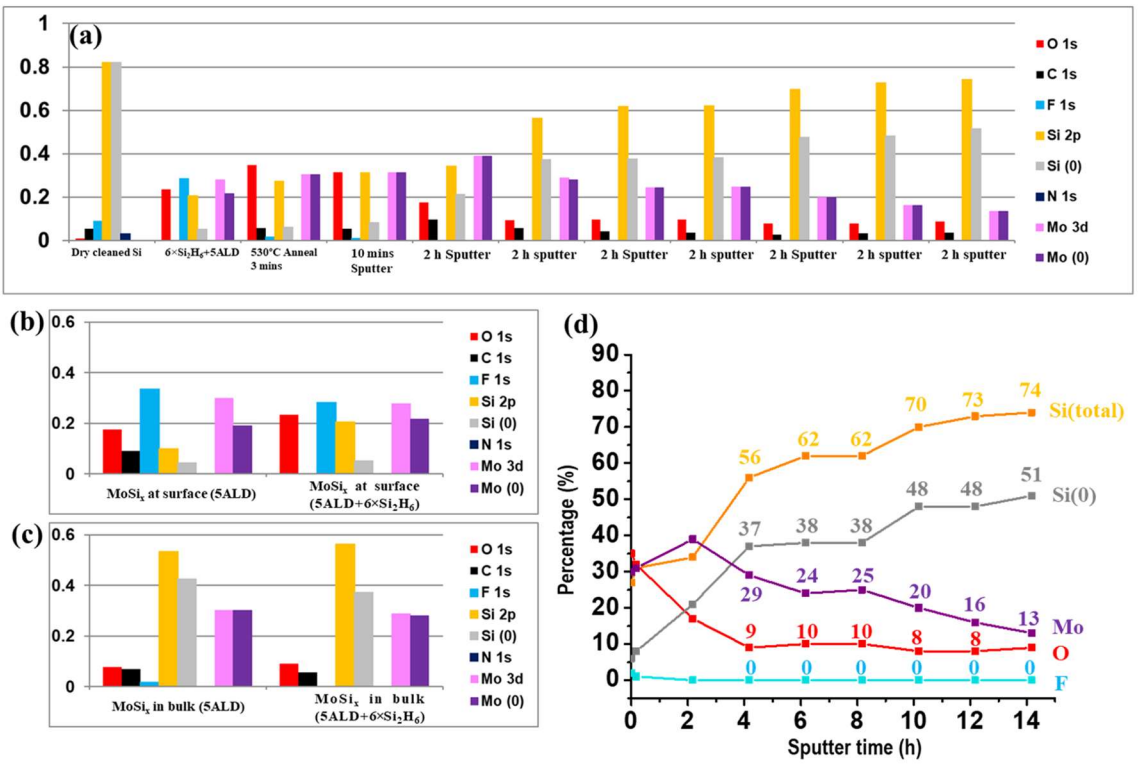

Figure 2.7. Depth profiling XPS study of the $MoSi_x$ film with extra Si_2H_6 doses. (a) A series of Ar^+ sputtering experiments were performed in conjunction with XPS on dry cleaned Si after 5 cycles of MoF_6 and Si_2H_6 followed by additional 6 pulses (25.2 MegaL) of Si_2H_6 at 120°C. (b) Surface composition after 5 ALD cycles of MoF_6 and Si_2H_6 with and without extra Si_2H_6 pulses is compared. Si/Mo ratios were 0.33 for 5 ALD and 0.89 for 5ALD + 6×Si_2H_6 which is consistent with Si incorporation on the surface. (c) Bulk composition of $MoSi_x$ with and without extra Si_2H_6 pulses is compared after getting rid of the surface contaminations using Ar^+ sputter. Si/Mo ratios were 1.77 for 5 ALD and 1.96 for 5ALD + 6×Si_2H_6. (d) The chemical composition of the film is plotted versus Ar^+ sputter time on Si after 5 cycles of MoF_6 and Si_2H_6 followed by additional Si_2H_6 pulses at 120°C. A lens voltage of 5kV with a beam current of 1.2 μA at 6.0×10^{-7} Torr of Ar was employed.

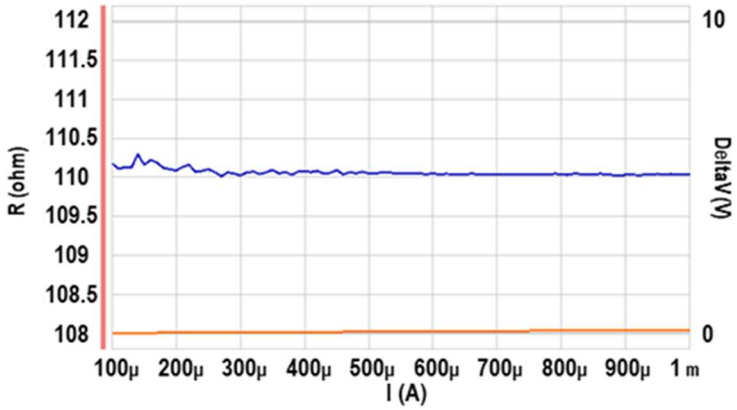

Figure 2.8. 4-probe measurement after Ni deposition on the 900°C annealed $MoSi_x$/Si. Using an infinite sheet model approximation, the resistivity of the $MoSi_x$ film is estimated to be 498 μΩcm.

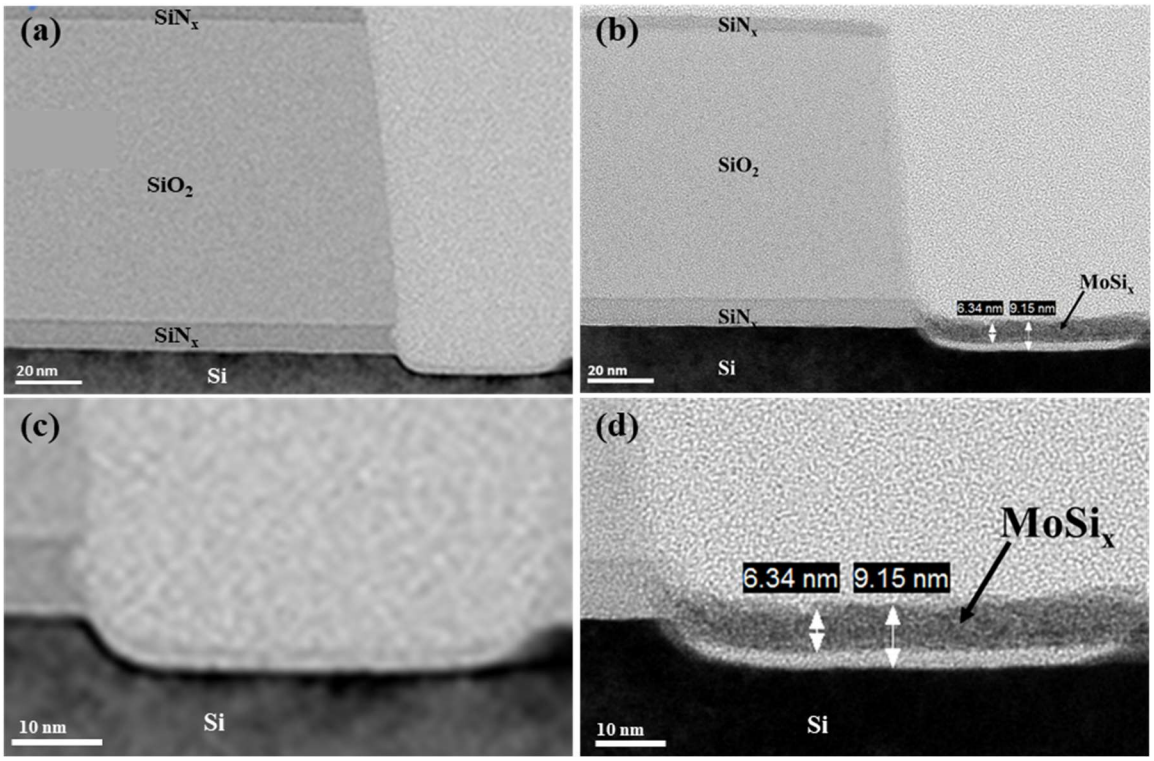

Figure 2.9. Selective ALD on a patterned sample. (a) Cross-sectional TEM image of the patterned sample before the deposition. (b) Cross-sectional TEM image of the HF cleaned patterned sample after 5 cycles of MoF_6 and Si_2H_6 at 120°C with a continuous N_2 purge. 6.34 nm of $MoSi_x$ was selectively deposited only on Si and not on SiO_2 nor SiN_x. (c) Magnified Si region of the patterned sample before the deposition. (d) Magnified Si region of the patterned sample after the $MoSi_x$ deposition shows that $MoSi_x$ was deposited without damaging Si substrate by etching.

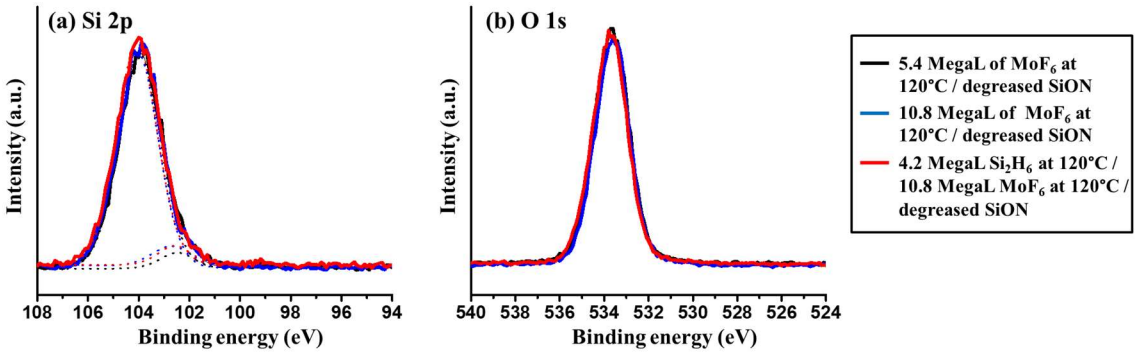

Figure 2.10. Oxidation states from XPS peaks of Si 2p and O 1s of degreased SiON at each experimental step of MoF_6 and Si_2H_6 doses. (a) Si 2p peaks show oxidation states of +3 and +4 which are consistent with strong Si-O, Si-N and Si-OH bonds. (b) O 1s peaks are positioned at 533.8 which is consistent with Si-O.

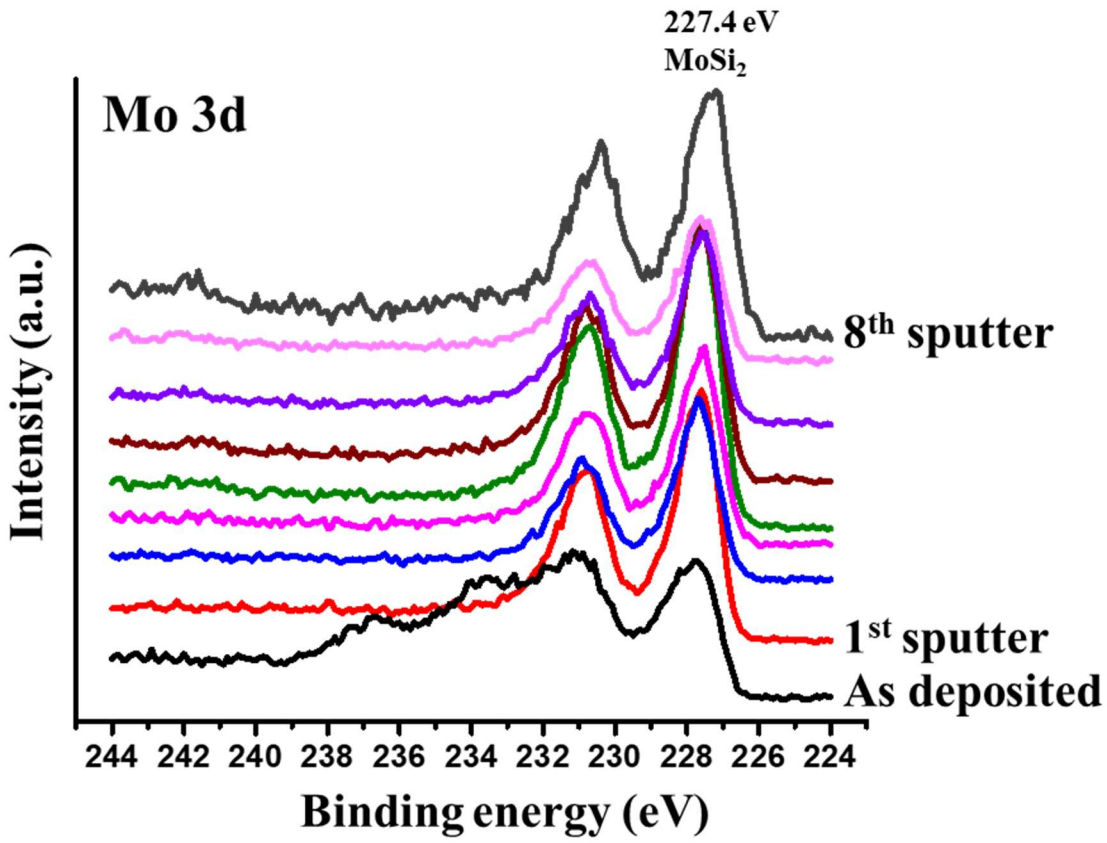

Figure 2.11. Depth profiling XPS study of the $MoSi_x$ film. XPS peaks of Mo 3d after sequential Ar^+ sputter cycles show that the Mo 3d peak stays at a 0 oxidation state.

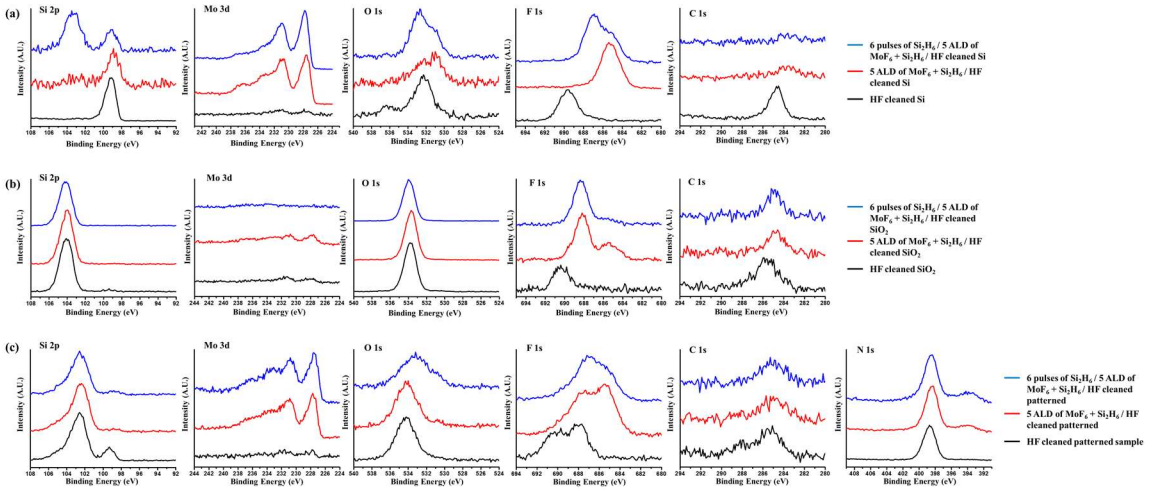

Figure 2.12. XPS spectra of Si 2p, Mo 3d, O 1s, F 1s, C 1s and N 1s on (a) HF cleaned Si, (b) HF cleaned SiO_2 and (c) HF cleaned patterned sample at each step of $MoSi_x$ deposition.

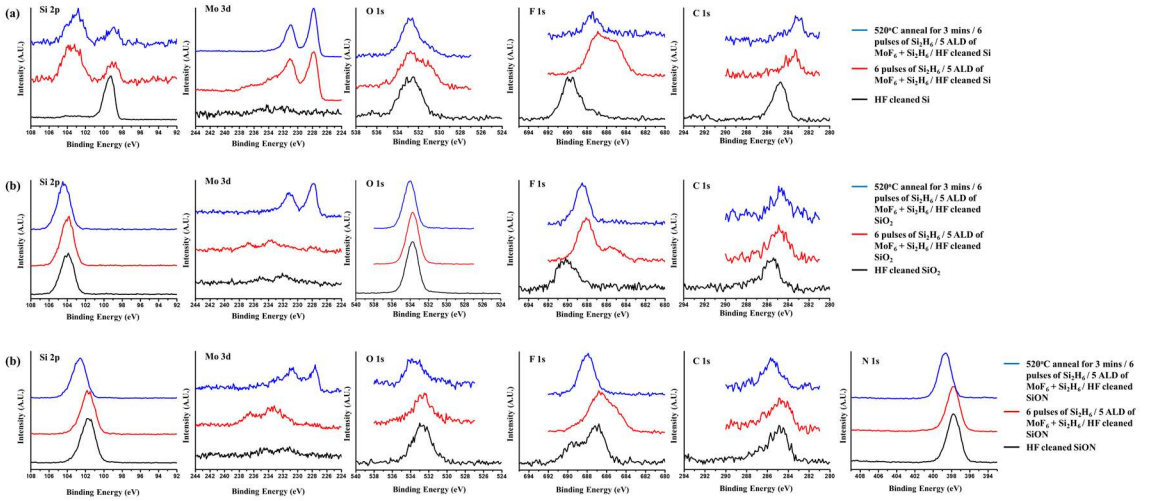

Figure 2.13. XPS spectra of Si 2p, Mo 3d, O 1s, F 1s, C 1s and N 1s on (a) HF cleaned Si, (b) HF cleaned SiO_2 and (c) HF cleaned SiON at each step of $MoSi_x$ deposition followed by 520°C anneal for 3 mins.

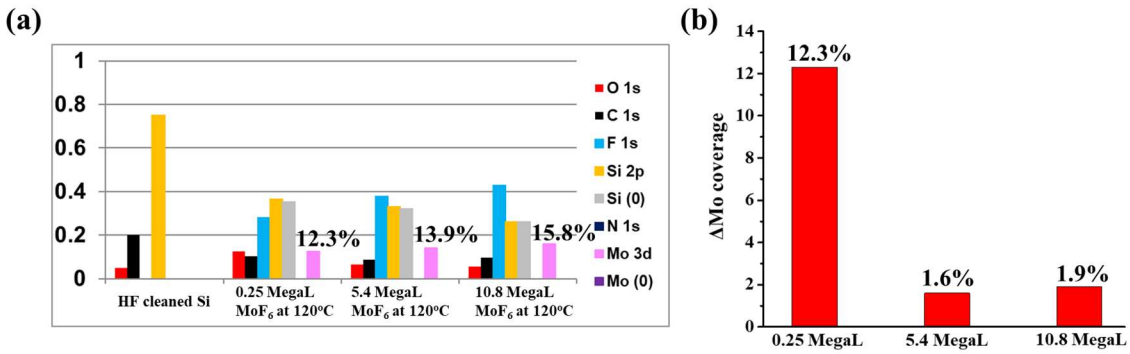

Figure 2.14. Saturation study of MoF_6 on HF cleaned Si. (a) The elemental composition of HF cleaned Si followed by different amount of MoF_6 doses. (b) Change of Mo coverage per MegaL of dose for each experiment of MoF_6 dose.

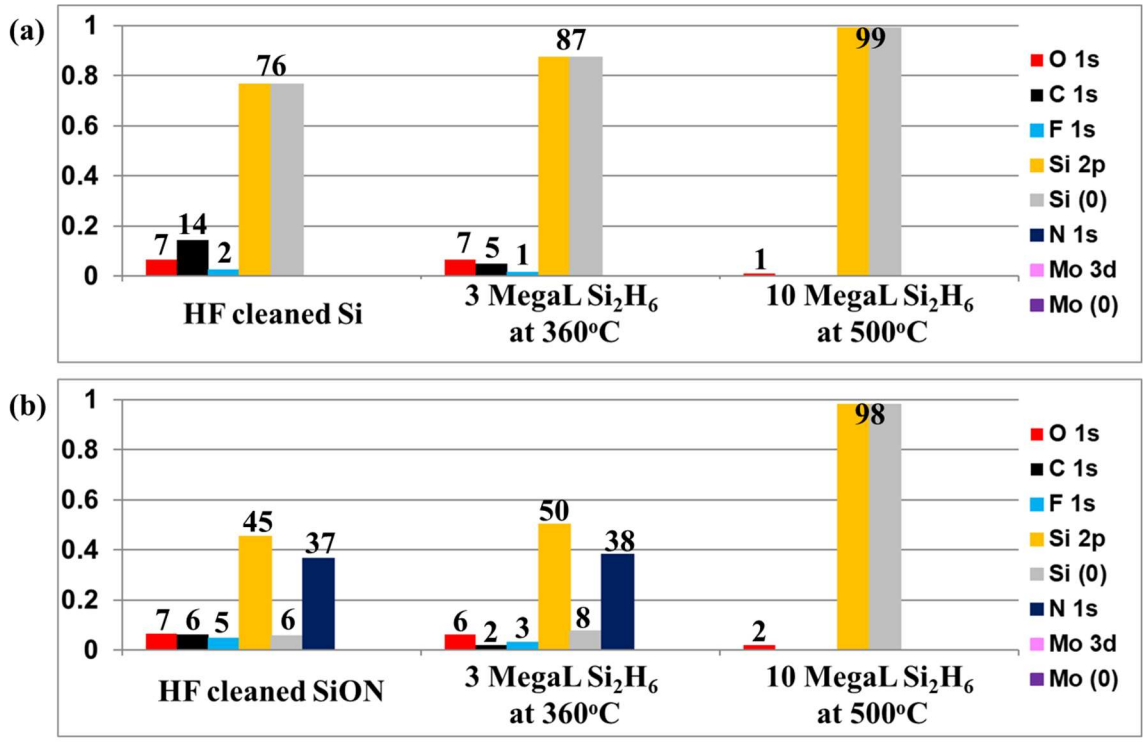

Figure 2.15. Chemical Vapor Deposition of Si via Si_2H_6 decomposition. (a) HF cleaned Si was exposed to Si_2H_6 doses at 360°C and 500°C. (b) HF cleaned SiON was exposed to Si_2H_6 at 360°C and 500°C. Both surfaces were completely covered with Si at 500°C consistent with the Si_2H_6 decomposition at 500°C.

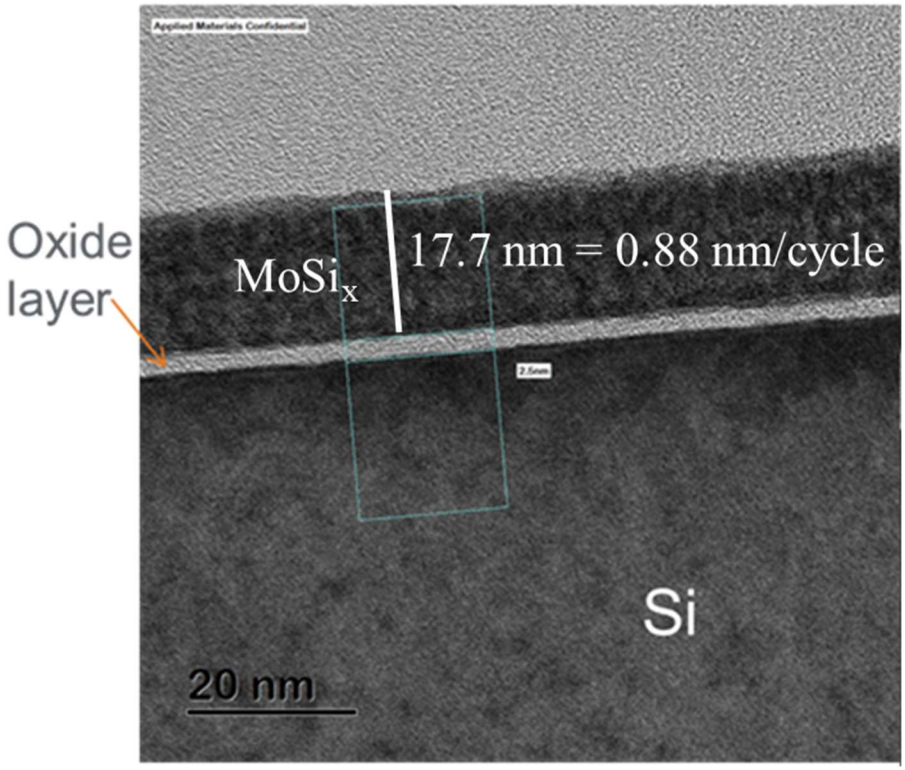

Figure 2.16. Cross-sectional TEM image after 20 cycles of $MoSi_x$ ALD on HF cleaned Si. 17.7 nm of $MoSi_x$ was deposited which corresponds to a growth rate of 0.88 nm/cycle.

2.9 References

(1) K. Lee; S.W. Park; M.J. Ko; K. Kim; N.-G. Park, *Nat. Mater.* **2009**, 8, 665.

(2) J. Xie; X. Yang; B. Han; Y. Shao-Horn; D. Wang; *ACS Nano* **2013**, 7, 6557.

(3) W.-H. Kim; F.S.M. Hashemi; A.J.M. Mackus; J. Singh; Y. Kim; D. Bobb-Semple; Y. Fan, T. Kaufman-Osborn; L. Godet; S.F. Bent, *ACS Nano* **2016**, 10, 4451.

(4) J.A. Liddle; G.M. Gallatin, *ACS Nano* **2016**, 10, 2995.

(5) D.G. Lishan; H.F. Wong; D.L. Green; E.L. Hu; J.L. Merz; D. Kirillov; *J. Vac. Sci. Technol., B: Microelectron. Process. Phenom*. **2019**, 7, 556.

(6) C.H. Jan; U. Bhattacharya; R. Brain; S.J. Choi; G. Curello; G. Gupta; W. Hafez; M. Jang; M. Kang; K. Komeyli; T.Leo; N. Nidhi; L. Pan; J. Park; K. Phoa; A. Rahman; C. Staus; H. Tashiro; C. Tsai; P. Vandervoorn; L. Yang; J.Y. Yeh; P. Bai, *IEEE int. Electron Devices Meet.* **2012**, 3.1.1.

(7) M. Fang; J.C. Ho, *ACS Nano* **2015**, 9, 8651.

(8) M.H. Park; Y.J. Jang; H.M. Sung-Suh; M.M. Sung; *Langmuir*, **2004**, 20, 2257.

(9) A. Mameli; M.J.M. Merkx; B. Karasulu; F. Roozeboom; W.M.M. Kessels; A.J.M. Mackus, *ACS Nano* **2017**, 11, 9303.

(10) F.S. Minaye Hashemi; C. Prasittichai; S.F. Bent, *ACS Nano* **2015**, 9, 8710.

(11) S.E. Atanasov; B. Kalanyan; G.N. Parsons; *J. Vac. Sci. Technol. A* **2015**, 34, 01A148-1-9.

(12) M.M. Kerrigan; J.P. Klesko; S.M. Rupich; C.L. Dezelah; R.K. Kanjolia; Y.J. Chabal; C.H. Winter, *J. Chem. Phy.* **2017**, 146, 052813-1-8.

(13) P.C. Lemaire; M. King; G.N. Parsons, *J. Chem. Phys.* **2017**, 146, 052811-1-9.

(14) B. Kalanyan; P.C. Lemaire; S.E. Atanasov; M.J. Ritz; G.N. Parsons, *Chem. Mater.* **2016**, 28, 117.

(15) A.H. Reader; A.H.V. Ommen; P.J.W. Wijs; R.A.M. Wolters; D.J. Oostra, *Rep. Prog. Phys.* **1992**, 56, 1397.

(16) S.P. Murarka, *Ann. Rev. Mater. Sci.* **1983**, 13, 117.

(17) M.Y. Tsai; H.H. Chao; L.M. Ephrath; B.L. Crowder; A. Cramer; R.S. Bennett; C.J. Lucchese; M.R. Wordeman, *J. Electrochem. Soc.* **1981**, 128, 2207.

(18) D. Seghete; G.B. Rayner Jr.; A.S. Cavanagh; V.R. Anderson; S.M. George; *Chem. Mater.* **2011**, 23, 1668.

(19) K. Bernal-Ramos; M.J. Saly; R.K. Kanjolia; Y.J. Chabal; *Chem. Mater.* **2015**, 27, 4943.

(20) T. Proslier; J.A. Klung; J.W. Elam; H. Claus; N.G. Becker; M.J. Pellin; *J. Phys. Chem. C* **2011**, 115, 9477.

(21) Y.J. Chabal; G.S. Higashi; K. Raghavachari; *J. Vac. Sci. Technol. A* **1989**, 7, 2104.

(22) J.W. Klaus; S.J. Ferro; S.M. George, *Thin Solid Films* **2000**, 360, 145.

(23) E.K. Broadbent; C.L. Ramiller; *J. Electrochem. Soc.* **1984**, 131, 1427.

(24) K.M. Chang; S.W. Wang; C.H. Li; J.Y. Tsai; T.H. Yeh; *Jpn. J. Appl. Phys.* **1996**, 35, 6555.

(25) D.-S. Choi, *Semicon. Sci. Technol.* **2012**, 12, 41.

(26) Y. Mitani, H. Satake, Y. Nakasaki, A. Toriumi, *IEEE Trans. Electron Devices* **2003**, 50, 2221.

(27) D.-G. Lin; T.A. Rost; H.S. Lee; D.-Y. Lin; A.J. Tsao; B. McKee, *IEEE Electron device lett.* **1993**, 14, 469.

(28) Ph. Gouy-Pailler; Ph. Lami; R. Morales; *Thin Solid Films* **1994**, 241, 374.

(29) R. Mueller; H.K. Kammler; K. Wegner; S.E. Prastsinis, *Langmuir* **2003**, 19, 160.

(30) J. Kwon; M. Saly; M.D. Halls; R.K. Kanjolia; Y.J. Chabal, *Chem. Mater.* **2012**, 24, 1025.

(31) C. Ahles; J.Y. Choi; A. Kummel, A Dry NF_3/NH_3 Plasma Clean for Removing Si native Oxide and Leaving a Smooth Si surface. Presented at Materials Research Society, Phoenix, the United States, Apr. 6, 2018; EP01.10.04

(32) C.D. Wagner; D.E. Passoja; H.F. Hillery; T.G. Kinisky; H.A. Six; W.T. Jansen; J.A. Taylor, *J. Vac. Sci. Technol.* **1982**, 21, 933

(33) W.A. Brainard; D.R. Wheeler, *J. Vac. Sci. Technol.* **1978**, 15, 1800.

Chapter 3

Highly Selective Atomic Layer Deposition of $MoSiO_x$ Using Inherently Substrate-Dependent Processes

3.1 Abstract

A resistive $MoSiO_x$ film was deposited with high selectivity on Si in preference to SiO_2 and SiN using MoF_6, Si_2H_6 and O_2 as reactants. Two different approaches were demonstrated via thermal atomic layer deposition (ALD). First, ALD of $MoSiO_x$ by sequential dosing of MoF_6, Si_2H_6 and O_2 (ABC-type) at 200°C followed by an ex-situ post-deposition anneal (PDA) in O_2 at 350°C was performed. The growth of the film using the ABC-type deposition was limited to ~5.25±0.5 nm because the insulating film inhibits the MoF_6 and Si_2H_6 ALD reaction. The second method was to grow $MoSi_x$ at 120°C and employ a post-deposition anneal in O_2/He at 350°C (AB+C-type) to form $MoSiO_x$. The selectivity of this process on Si versus SiO_2 was perfect for 10 nm of deposition on Si, as there were no nuclei or particle formation observed on the SiO_2 surface by atomic force microscopy (AFM). The high selectivity can be obtained due to the inherent inability of MoF_6 to react SiO_2 and SiN surfaces. Transmission electron microscopy (TEM) of a nanoscale-patterned sample demonstrated that the highly selective $MoSiO_x$ can be achieved and be integrated into three-dimensional nanoscale structures.

3.2 Introduction

As metal-oxide-semiconductor field effect transistors (MOSFETs) are scaled to sub-10 nm nodes with three-dimensional features, it becomes a significant challenge to

enhance the feature density and quality in patterning processes. Conventional patterning processes such as photolithography and e-beam lithography rely on multiple steps of resist patterning. These processes involve a combination of deposition and lithography followed by wet and plasma etching, which might lead to imperfect alignment and low resolution issues. [1,2] Additionally, some metals such as Cu and Co are not easy to etch. [3-5] Area selective atomic layer deposition (ALD) is of great interest in multi-patterning processes since it provides conformality, spatial uniformity and selectivity. Selective oxide deposition might simplify self-aligned double patterning (SADP) by depositing on side walls of the lithographically defined mandrel without depositing on the bottom layer (see Supplement, Fig. 3.11). In the multiple patterning processes, sharp self-aligned selective deposition is required not only to pattern the sub-10 nm features but also to reduce the need for lithography. [1,6]

Selective ALD of oxides is challenging since strongly oxidizing co-reactants can induced reactions on any surface. For example, the most commonly used oxygen sources for metal oxide deposition are H_2O, H_2O_2, O_2 plasma and ozone (O_3) which can physisorb or chemisorb onto semiconductor, insulator, and metallic surfaces initiating ALD nucleation. [7-12] One technique for selective deposition of oxides with these strong oxidants is to add passivants or plasma etching steps every cycle or every couple of cycles to prevent any nucleation leading to selectivity loss on an unwanted surface. [15-17] For example, Mameli et al. [15] demonstrated area selective atomic layer deposition of ~1.5 nm thick SiO_2 on GeO_2 against Al_2O_3 by a three-step deposition (ABC-type cycle) using A: acetylacetone (Hacac), B: bis(diethylamino)silane and C: O_2 plasma. They reported that the gas phase Hacac inhibitor reacts only with the Al_2O_3 substrate and not with GeO_2 or

SiO_2; however, the inhibitor needed to be dosed in each ALD cycle since the O_2 plasma removed the Hacac inhibitor. Single step passivation has also been reported; for example, Hashemi et al.[16] demonstrated area selective ALD of ~30 nm ZnO on SiO_2 against Cu using diethylzinc and water as ALD precursors. This was accomplished with vapor phase passivation using dodecanethiol (DDT) self-assembled monolayer (SAM) followed by an ex-situ sonication to inhibit growth on Cu. The selectivity could be expanded to 100 nm by regenerating DDT SAM every 150 ALD cycles; however, regeneration of passivation layer may also necessitate another wet selective removal step for residual passivants after the deposition process is complete. [18]

To avoid using oxidants such as H_2O or O_2 plasma, there have been studies to deposit oxide thin films by employing metal alkoxides as a precursor that can supply both an oxygen and a metal atom. [13,14,19] Atanasov et al.[19] demonstrated inherent substrate-dependent growth of TiO_2 on hydroxyl terminated SiO_2 (Si-OH) against hydrogen terminated Si (Si-H) using titanium tetra-isopropoxide (TTIP) and $TiCl_4$. It is hypothesized that the oxidants hydroxylate H-Si surfaces and initiate nucleation on Si. This process did not use any passivant nor seeding layers; however, the nucleation delay on Si was only sufficient to deposit 2 nm TiO_2 on SiO_2.

Inherently selective ALD is a compelling process to achieve selective deposition on the nanoscale without using passivants, seeding layers, or additional plasma steps since this relies only on the reactivity of ALD precursors with different substrates. Previously, Choi et al demonstrated on selective $MoSi_x$ deposition on Si in preference to SiO_2, SiON and SiN, [20]; MoF_6 and Si_2H_6 did not react with OH-SiO_2 and NH_x-SiN due to the chemical inertness of the strong Si-O, Si-N, SiO-H and SiN-H bonds towards the ALD

precursors. In contrast, MoF_6 reacted with a H-Si surface by forming Si-MoF_x bonds which enables a chain reaction with following Si_2H_6.

In this work, an insulating molybdenum silicon oxide ($MoSiO_x$) was deposited by ALD on silicon in preference to silicon oxide and silicon nitride using MoF_6 and Si_2H_6 and O_2 using substrate-dependent selectivity. A successful conformal $MoSiO_x$ deposition on a nanoscale three-dimensional Si sidewall with about 200:1 selectivity over SiO_2 and SiN were demonstrated which could be transferred to the multi-patterning process for 3-dimensional MOSFETs.

3.3 Experimental

Fig. 3.1 shows a schematic of the vacuum chamber. The selective deposition of $MoSiO_x$ was performed in a home-built reaction chamber (ALD chamber) pumped by a turbomolecular pump and a rotary pump connected in series. The chamber had an in-situ heating and sample transfer system using a pyrolytic boron nitride (PBN) heater mounted on a manipulator. The base pressure of the reaction chamber was 8.0×10^{-8} Torr. The chamber wall was set to 80°C and dosing lines for MoF_6, Si_2H_6, N_2 and O_2 were kept at room temperature. Pneumatic valves (UHP diaphragm sealed valve, Swagelok) controlled by a computer program (Labview 8.0) were employed to precisely regulate the valve opening times in milliseconds. The processed samples were transferred into an ultra-high vacuum (UHV) chamber equipped with X-ray Photoelectron Spectroscopy (XPS) for characterization without air exposure.

P-type Si (001) (Waferworld), thermally grown SiO_2 (Waferworld), and SiON samples (Applied Materials) were used for the selective deposition of $MoSiO_x$. Note that

the SiON is actually a stoichiometric Si_3N_4 after a reactive ion etching (RIE) and O_2 plasma ashing process which mimics the surface condition of a lithographically patterned sample. The samples were rinsed sequentially with acetone, methanol and HPLC-grade water followed by a wet clean in a 0.5% HF solution for 30 seconds to remove native oxides. After the HF clean, the samples were rinsed again with HPLC-grade water for 10 seconds and blow-dried with high purity N_2. The HF cleaned samples were loaded into a sample loading chamber, and the chamber was pumped down to 5.0×10^{-6} Torr before transferring the samples to the UHV chamber. The chemical compositions of the samples were investigated using XPS in the UHV chamber before and after each experiment.

MoF_6 (Synquest Laboratories, 99%), Si_2H_6 (Air Liquide, 99.99%) and O_2 (Praxair, 10% balanced in He) were used as the ALD precursors at a temperature in the range of 120 – 200°C followed by an in-situ or ex-situ O_2 anneal at 300 – 350°C. As previously reported, [20] MoF_6 and Si_2H_6 selectively react with Si in preference to SiO_2 and SiN_x to form $MoSi_x$. Two approaches were employed to incorporate oxygen into the $MoSi_x$ using O_2 in a thermal process. The first method was to incorporate oxygen into the film during a three step ALD cycle: MoF_6 + Si_2H_6 + O_2 at 200°C. The dose sizes of MoF_6 and Si_2H_6 were 1.2 MegaL and 2.2 MegaL (1 Lanmuir (L) = 10^{-6} Torr × 1 second exposure of a gas). O_2 (10% balanced in He) was dosed using a leak valve at 120 mTorr for 6 mins which corresponds to 4.3 MegaL of O_2. Each precursor was separated by an N_2 purge at 90 mTorr for one minute. Additionally, an ex-situ post deposition anneal (PDA) under a constant flow of 100% O_2 at 1 SLM was performed at 350°C in an AllWin21 rapid thermal annealing system. The ex-situ O_2 anneal was performed at ~1 atm pressure for 10 mins which corresponds to 456 GigaL of O_2. The second method was to grow a $MoSi_x$ film selectively on a Si substrate

and convert the $MoSi_x$ film into $MoSiO_x$ at high temperature; the ALD of MoF_6 + Si_2H_6 was performed at 120°C followed by an in-situ anneal in O_2 (10% balanced in He) at 15 Torr for 10 mins which corresponds to 900 MegaL of O_2 at 350°C.

A monochromatic Al Kα X-ray source and a hemispherical analyzer (XM 1000 MkII/SPHERA, Omicron Nanotechnology) were used for XPS. The anode voltage was set to 10 kV with a filament emission current of 25 mA. The focused beam size on the samples was 0.7 – 1 mm. For the XPS measurements, the samples were aligned to the detector to have a 30-degree take-off angle from the sample surface (i.e near glancing) for the surface sensitive detection. As the occasion demands, 60-degree take-off angle form the sample surface was also used for the bulk composition. The peak areas of XPS spectra were normalized to the sum of all elements after a sensitivity correction using the Casa XPS v2.3 program. The topology of the deposited film was studied using AFM (Agilent 5500) in tapping mode. The nanoscale patterned sample was supplied from Applied Materials and cross-sectional TEM was performed before and after the selective $MoSiO_x$ deposition at Applied Materials.

3.4 Results and Discussion

3.4.1 XPS of 3-step $MoSiO_x$ ALD at 200ºC followed by in-situ and ex-situ PDA

The sequential three-step reaction of MoF_6, Si_2H_6 and O_2 on Si at 120°C and 200°C was investigated using an in-situ XPS. The chemical composition of the Si surface after each experiment step is shown in Fig. 3.2. Si and Mo are presented in two different bars in order to indicate the total amount (Si 2p and Mo 3d) together with the oxidized components

(Si (ox) and Mo (ox)) which correspond to Si^{1+} through Si^{4+} and Mo^{1+} through Mo^{6+}. Note that $MoSiO_x$ should have both oxidized Si and oxidized Mo components.

Fig. 3.2(a) shows a cycle of $MoSiO_x$ deposition at 120°C on HF cleaned Si. (note: the raw XPS spectra are presented in Fig.S2). The Si sample had about 20% adventitious hydrocarbon (red and black) on the surface after the native oxide removal using an aqueous HF. 0.25 MegaL of MoF_6 were dosed at 120°C and 12% Mo and 28% F were deposited. All of the Mo was in oxidation states of +4 and +5 consistent with MoF_x termination of the surface. MoF_6 has a self-limiting reaction on HF cleaned Si, and 0.25 MegaL of MoF_6 was the saturated dose of MoF_6 on Si at 120°C. [20] 26.4 MegaL of Si_2H_6 was dosed on MoF_6 saturated Si surface which reduced MoF_x to Mo (0) by forming Mo-Si bonds consistent with $MoSi_x$ deposition. The 11% oxidized component of Si (grey bar) and 4% oxidized Mo component (purple bar) might be due to the O and F contamination at the surface. Subsequently, 3.5 MegaL of O_2 was dosed which increased O from 17% to 26%; however, the oxidized component of Mo remained 4% out of a total of 8%. After another 4.3 MegaL of O_2 was dosed at 120°C, O increased only by 2% and the oxidized component of Mo increased to 6% out of a total of 8%. At 120°C, reactivity of O_2 with a $MoSiO_x$ monolayer was insufficient to completely oxidize $MoSi_x$. In Fig. 3.2(b), the same sample was employed to investigate higher temperature (200°C) reaction with O_2. 4.3 MegaL O_2 at 200°C was able to fully oxidize Mo, the oxidized component of Si increased from 14% to 16%, and the O increased from 28% to 32% consistent with a complete conversion of $MoSi_x$ into $MoSiO_x$. After 3 additional ALD cycles at 200°C, the total thickness of the $MoSiO_x$ film on Si was ~ 2.2 nm calculated from the attenuation of the Si substrate. In contrast, during the same exposure of MoF_6, Si_2H_6, and O_2 at 120°C and 200°C, HF cleaned

SiO_2 remained non-reactive which is consistent with the inherent non-reactivity of the SiO_2 surface against these precursors. (Fig. 3.2(b))

After the $MoSiO_x$ ALD cycles at 120 – 200°C, in-situ and ex-situ post deposition anneals (PDA) in O_2 were performed to further oxidize the film. (note: the raw XPS spectra are presented in Fig. 3.13). Fig. 3.3(a) shows the XPS elemental compositions after each O_2 PDA step and Fig. 3.3(b-c) presents the corresponding oxidation states of Mo 3d and Si 2p. As deposited $MoSiO_x$ had oxidation states of Mo^{1+} and Mo^{3+}. Si had Si^{4+} and Si^0. Note that Si^0 component corresponds to the Si substrate peak. An in-situ O_2/He anneal was performed on $MoSiO_x$/HF-Si at 300°C for 6 mins at a constant flow of O_2/He at 80 – 150 mTorr. This corresponds to 432 MegaL of O_2. After the in-situ O_2/He anneal, F at the surface went down from 16% to 3% and O went up from 36% to 43% consistent with a substitution of surface F with O. However, the oxidation states of Mo still contained a large fraction of Mo^{1+}. Therefore, an ex-situ oxidation at ~ 1 atm was performed for 10 mins at 350°C using an AllWin21 rapid thermal annealing system with a constant 100% O_2 flow at 1 SLM at about 1 atm. This corresponds to 456 GigaL of O_2. After the ex-situ anneal, the sample was introduced back into the UHV chamber to analyze the compositions and oxidation states. The elemental composition showed a large amount of surface C and O which have resulted from the air exposure during transfer. However, the oxidation states of both Mo 3d and Si 2p were consistent with fully oxidized $MoSiO_x$. The could be due to either the higher temperature or $\sim 10^3\times$ larger dose of O_2 compared to the in-situ O_2/He anneal at 300°C. Below, it is shown that the film can be fully oxidized (as quantified by XPS) by an in-situ anneal in O_2/He at at 15 Torr at 350°C.

3.4.2 Surface morphology of the $MoSiO_x$ film deposited via 3-step ALD

The surface morphologies of the deposited $MoSiO_x$ film from 3 step ALD were studied using atomic force microscopy (AFM) for as-deposited, after an in-situ O_2/He anneal at 300°C, and after ex-situ O_2 anneal at 350°C. Fig. 3.4(a) shows the surface morphology of the as-deposited 3 step ALD $MoSiO_x$ on Si after the 4 ALD cycles at 120 - 200°C. The $MoSiO_x$ film was atomically flat with an RMS roughness of 5.3 Å. Fig. 3.4(b) depicts the 3 step ALD $MoSiO_x$ surface after an in-situ O_2/He anneal at 15 torr at 300°C to further oxidize the unsaturated $MoSiO_x$ film. The film was smoother after the anneal with an RMS roughness of 3.8 Å. Fig. 3.4(c) shows an AFM image of the 3 step ALD $MoSiO_x$ surface after the ex-situ O_2 anneal at ~1 atm at 350°C for 10 mins. The surface after the ex-situ anneal was roughened and had ~12 nm tall agglomerations which might be due to the large insertion of oxygen. The RMS roughness was 1.7 nm. To check the selectivity of $MoSiO_x$ on SiO_2, AFM was performed on HF cleaned SiO_2 after 4 ALD cycles of 3 step ALD $MoSiO_x$ followed by an in-situ O_2/He anneal at 300°C (see Fig. 3.4(d)). The SiO_2 surface was very clean with an RMS roughness of 5.3 Å. There was no $MoSiO_x$ nucleation or particle formation observed on the surface which shows the absolute inherent selectivity of the $MoSiO_x$ ALD on SiO_2.

3.4.3 Growth limit and selectivity of $MoSiO_x$ film deposited via 3-step ALD

To study the selectivity and growth rate of 3 step ALD $MoSiO_x$ with XPS, thicker films were deposited on Si and SiO_2. A total of 20 ALD cycles of 3 step ALD $MoSiO_x$ at 200°C were performed and the film thickness was calculated by the attenuation of the substrate after each 5 ALD cycles. (note: the raw XPS spectra are presented in Fig. 3.14).

Fig.5(a) presents the elemental percentage of Si and Mo from the Si and SiO_2 substrates for up to 20 ALD cycles at 200°C. As the number of cycles increases, the Si(0) percentage from the Si substrate decreases which is consistent with the attenuation of Si due to the $MoSiO_x$ growth. The Mo percentage on the Si substrate was saturated at ~20% after 5 ALD cycles consistent with the composition of the $MoSiO_x$ film being conformal throughout the film. In contrast, Si(ox) of SiO_2 which corresponded to the SiO_2 substrate remained at ~40% throughout the 20 ALD cycles which is consistent with no $MoSiO_x$ deposition. A negligible amount of Mo was detected on the SiO_2 substrate.

Fig. 3.5(b) shows the $MoSiO_x$ film thickness on Si and SiO_2 as a function of the number of ALD cycles. After the first 5 ALD cycles, the thickness of $MoSiO_x$ on Si was 3.30±0.35 nm which corresponds to a growth rate of 6.6 Å/cycle. The second set of 5 ALD cycles (up to 10^{th} cycle) and the third set (up to 15^{th} cycle) shows slower growth rates of 2.8 and 1.1 Å/cycle. After the 15^{th} ALD cycle, there was no additional growth of $MoSiO_x$ on Si. Overall, $MoSiO_x$ on Si showed a logarithmic growth and saturated at 5.25±0.5 nm. The larger growth rate of $MoSiO_x$ during the first 5 ALD cycles might be due to MoF_6 reacting more than a monolayer of the Si substrate. As the film grew, the substrate effect became smaller and the growth rate decreased. After 15 ALD cycles, the $MoSiO_x$ film became inert to both MoF_6 and Si_2H_6 due to the strong bonds of Mo-O and Si-O which terminate the reaction. Conversely, there was no growth observed on SiO_2 for up to 20 ALD cycles.

Selectivity of $MoSiO_x$ ALD on SiO_2 was calculated from XPS sensitivity. After a total of 20 ALD cycles, there were 1.9% Mo and 6.4% F detected on SiO_2 by XPS. Assuming all of Mo and F were conformally covering the topmost surface of SiO_2, this

corresponds to less than 0.5Å thick film calculated using the inelastic mean free path (IMFP) of electron and electron attenuation length (AL) as follows:

$$\lambda = \frac{143}{E^2} + 0.054\sqrt{E}$$

$$I = I_0 \exp(-t/\lambda \sin\theta)$$

, where λ is an IMFP of electron, E is a kinetic energy of electron, I is an attenuation length (AL), I_0 is a constant, t is a thickness (layer depth) and θ is an angle of emitted electron from the surface. Assuming a monolayer of the $MoSiO_x$ film is ~3 Å, $MoSiO_x$ on SiO_2 after 20 ALD cycles was calculated to 0.167 monolayer. As the $MoSiO_x$ film on Si after 20 ALD cycles was estimated to 5.25 nm, which corresponds to 17.5 monolayers, the selectivity of $MoSiO_x$ between Si and SiO_2 is at least 100:1 consistent with the more sensitive AFM determination of selectivity.

3.4.4 2-step ALD of $MoSi_x$ + in-situ O_2/He anneal

To overcome the growth limit, a second technique of selective $MoSiO_x$ deposition was investigated which was to selectively deposit $MoSi_x$ using MoF_6 and Si_2H_6 at 120°C and then convert the $MoSi_x$ film into $MoSiO_x$ via an in-situ O_2/He anneal at 350°C at 15 Torr. Fig. 3.6 shows the XPS composition of a new batch of HF cleaned Si and HF cleaned SiO_2 samples for the second technique denoted as "2 Step ALD". HF cleaned Si had ~20% hydrocarbon on the surface. After 5 ALD cycles of MoF_6 and Si_2H_6 to deposit $MoSi_x$ at 120°C, the composition of the film was 31% Mo, 16% Si, 23% O and 29% F consistent with previous experiments. [20] Note that Mo(ox) was only 7% out of 31% consistent with metallic Mo-Si bond formation of $MoSi_x$. After an in-situ O_2/He (10% balanaced in He) anneal at 15 Torr for 10 mins at 350°C, All of Mo was oxidized, and the film surface was

mostly MoO_x with only 4% Si. The data is consistent with the 350°C O_2 anneal inducing loss of fluorine from the surface via SiF_x desorption and formation of additional Mo-O bonds. To study the bulk composition of the film, near normal XPS (60° take-off angle from the sample surface) was performed. (see Fig. 3.6(a)) The bulk of the film had a Mo:Si:O ratio of 1: 0.8: 1.9 which is consistent with the in-situ O_2/He anneal segregating MoO_x on the surface of the film. This is consistent with the lower surface free energy of MoO_3 compared to SiO_2 (MoO_3: 70 ergs/cm_2 versus SiO_2: 307 ergs/cm^2)

HF cleaned SiO_2 has a negligible amount of C at the surface as presented in Fig. 3.6(b). (note: the raw XPS spectra are presented in Fig. 3.15). After 5 cycles of $MoSi_x$ ALD at 120°C, there was 1.5% Mo and 8% F detected on the surface. After an in-situ O_2/He anneal at 350°C, there was no change but a small decrease in F which is consistent with the inherently non-reactivity of $MoSiO_x$ on HF-SiO_2. The selectivity estimation using XPS sensitivity was also performed for 2 step ALD. There were 1.5% Mo and 5% F observed on SiO_2 after 5 ALD cycles of $MoSi_x$ followed by the in-situ O_2/He anneal at 350°C. This corresponds to a 0.5-thick conformal film which is 0.167 monolayer assuming 1 monolayer is 3 Å. The thickness of $MoSiO_x$ on Si after the same deposition deposited was about 6 nm $MoSiO_x$ (~20 monolayers of $MoSiO_x$) so that the selectivity of 2 step ALD was estimated to about 120:1. Fig. 3.6(c) presents the Mo 3d XPS spectra showing the oxidation states before and after the in-situ O_2/He anneal. After 5 ALD cycles of MoF_6 and Si_2H_6 at 120°C, Mo was mostly Mo^0 consistent with metallic $MoSi_x$ being deposited. After the in-situ O_2/He anneal at 350°C, Mo 3d peaks were shifted to Mo^{4+} and Mo^{5+} which corresponded to oxidized $MoSiO_x$. Fig. 3.6(d) shows the Si 2p XPS spectra before and after the in-situ O_2/He anneal. Before the in-situ O_2/He anneal, Si had two oxidation states of Si(0) and

Si(4). Si(0) corresponds to Mo-Si bonds from $MoSi_x$ and Si(4) component is due to the surface F and O contamination. After the in-situ O_2/He anneal at 350ºC, all of Si at the surface was at an oxidation state of 3 consistent with a full conversion to $MoSiO_x$.

3.4.5 Surface morphology and electrical property of the $MoSiO_x$ film

In Fig. 3.7, the surface morphology of $MoSiO_x$ before and after the in-situ O_2/He anneal at 350°C are shown. The surface morphology of $MoSi_x$ was smooth with an RMS roughness of 6.9Å (Fig. 3.7(a)). After an in-situ O_2/He anneal at 350ºC, the $MoSiO_x$ surface remained smooth with an RMS roughness of 1.0 nm (Fig. 3.7(b)). The slight increase of the RMS roughness can be attributed to the O_2 incorporation. To investigate the electrical properties of the $MoSiO_x$ film, a Ni gate on top of $MoSiO_x$ with an Al back contact were deposited via thermal evaporation. Fig. 3.7(c-d) depicts the current density-voltage (I-V) and conductance density-voltage (G-V) curves. The current density through the $MoSiO_x$ film in the gate bias range was smaller than ~$1x10^{-7}$A and the conductance density was constant across the gate bias which are both consistent with an insulating $MoSiO_x$ film.

3.4.6 Improvement of the selectivity window of 2-step $MoSiO_x$

Since the 2 Step ALD method relies on the selectivity of $MoSi_x$ before oxidizing the film using O_2/He, the selectivity limit of $MoSi_x$ ALD was studied using AFM. After 5 and 10 ALD cycles of $MoSi_x$ were dosed on SiO_2, the number of unwanted $MoSi_x$ particles on SiO_2 that were taller than 2.5 nm was detected using a SPIP v2.12 program. The threshold particle size of 2.5 nm was set to distinguish particles in proximity. Fig. 3.8(a) shows elemental compositions of SiO_2 after 5 and 10 $MoSi_x$ ALD cycles and corresponding

AFM images. There were 1% Mo detected on SiO_2 after 5 ALD cycles and 5.6% Mo after 10 ALD cycles. The AFM images show 16 particles/μm^2 after 5 ALD cycles and 268 particles/μm^2 after 10 cycles. The inherent selectivity of the $MoSi_x$ film on SiO_2 was preserved until 5 ALD cycles before having a critical amount of nucleation on SiO_2. The selectivity loss can be attributed to the decomposition of the precursors by the PBN heater that was placed in vacuum. To see the effect of the heater on the $MoSi_x$ selectivity, a cartridge heater, a different heater design, was installed and the number of $MoSi_x$ nuclei on SiO_2 were compared. The cartridge heater was placed on the air-side of the chamber conductively heating a Cu block on which the sample sits in vacuum, so that the precursors did not directly dose the heater. Using the cartridge heater, the $MoSi_x$ selectivity was greatly improved showing no nuclei on SiO_2 after 10 ALD cycles as shown in Fig. 3.8(b). XPS elemental composition only showed 0.5% Mo on SiO_2 after 10 ALD cycles which is an improvement of selectivity by a factor of 10 compared to the results using a PBN heater. There was no particle observed from AFM. This corresponds to ~10 nm thick $MoSi_x$ on Si which can be converted to $MoSiO_x$ by incorporating O_2. Using the cartridge heater, the selectivity could be extended to 200:1 calculated using the same XPS sensitivity method as described earlier.

3.4.7 TEM of 2-step $MoSiO_x$ demonstrated on a nanoscale patterned sample

Using inherently selective processes, a selective and conformal deposition of $MoSiO_x$ was demonstrated on a three-dimensional nano-trench structure with a high-aspect ratio. The structure of the patterned sample is described in Fig. 3.9(c). The Si fins are 225 nm tall and 50 nm wide with SiN mask on top of each Si fin separated by SiO_2.

Fig. 3.9(a) shows the elemental composition of the HF cleaned patterned sample. (note: the raw XPS spectra are presented in Fig. 3.16). The patterned sample had mostly SiN on the top-most surfaces. Note that there is 18% Si (0) which corresponds to the target area for $MoSiO_x$ deposition since the oxidized Si peak corresponds to the exposed SiN and SiO_2 surfaces. Fig. 3.9(b) shows the elemental composition after a selective $MoSiO_x$ deposition process. There was 8% fully oxidized Mo with 21% O. Note that all of the Si was oxidized consistent with a selective attenuation of the Si substrate (Si(0) component, the target area). The patterned sample shown in Fig. 3.9(c) is a top view SEM image of the HF cleaned patterned sample. The SiN mask was 50 nm wide and the gap between the SiN mask was 30 nm which is also shown in the insert on the left bottom corner. Fig. 3.9(d) shows the same region as Fig. 3.9(c) after the selective $MoSiO_x$ deposition. The gap between the features decreased to 20 nm and the SiN mask rows were enlarged to ~ 60 nm which is consistent with ~ 5 nm thick $MoSiO_x$ deposition on each sidewall of the Si fins.

Fig. 3.10 shows the cross sectional TEM images of the patterned sample before and after the selective $MoSiO_x$ deposition process. Fig. 3.10(a) shows the structure of the patterned sample. The patterned sample was cleaned using 5% HF solution for 30 seconds and selective $MoSiO_x$ deposition was performed. SiN mask and SiO_2 were etched by a 5% HF clean but $MoSiO_x$ was still very conformal and selective on Si. The deposited $MoSiO_x$ film was ~6 nm thick. The gap between each fin was ~20 nm which is consistent with the SEM image in Fig. 3.9(d). The TEM image demonstrates that the highly selective $MoSiO_x$ can be achieved on a patterned sample and be integrated into three-dimensional nanoscale multi-patterning processes.

3.5 Conclusions

A new approach to selectively deposit oxides on Si in preference to SiO_2 and SiN was demonstrated by two different inherently selective $MoSiO_x$ ALD processes using MoF_6, Si_2H_6 and O_2. Alternatingly dosed MoF_6, Si_2H_6 and O_2 at 200°C (3 Step ALD) deposited an oxygen-deficient $MoSiO_x$ film on Si with perfect selectivity over SiO_2 quantified by AFM. The selectivity estimated by XPS presented at least 100:1 between Si and SiO_2. An ex-situ anneal in 100% O_2 at 350°C could fully oxidized the film. The growth of $MoSiO_x$ on Si was limited up to 5 nm due to the inherent non-reactivity of the precursors towards the grown $MoSiO_x$ which demonstrates the strong substrate-dependent nature of $MoSiO_x$ ALD. For the thicker films, selective 2 step $MoSi_x$ ALD was employed before a conversion of the $MoSi_x$ film into $MoSiO_x$ by an in-situ O_2/He anneal. Loss of selectivity was not observed on SiO_2 until 10 nm of $MoSi_x$ was grown on Si which could expand the selectivity to 200:1. The selectivity of the process relies on the inherent selectivity of $MoSi_x$ ALD using MoF_6 and Si_2H_6 which deposits on Si but not on SiO_2 or SiON. It has been shown that this process is selective because of the weak Si-Si and H-Si bonds on Si and the ease of formation of SiF_4 on a Si substrate but the stronger Si-O, Si-N, SiO-H and SiN-H bonds in SiO_2 and SiN make this process less favorable. The conversion of metal or metal silicide into an oxide film is advantageous in terms of selectivity in that the process does not require any use of strong oxidants such as H_2O, H_2O_2 and O_2 plasma during the deposition which often leads to selectivity loss. For the selective ALD of metal or metal silicides such as $MoSi_x$, W, Mo, Co and $CoSi_2$, reductants are employed which utilize an inherent surface-dependent selectivity and subsequently convert them into oxides by an O_2

PDA. Selective $MoSiO_x$ deposition on the sidewalls of Si fins in nanoscale demonstrated a great potential application in three-dimensional nanoscale multi-patterning processes.

3.6 Acknowledgements

Funding support from Applied Materials is gratefully acknowledged. The electrical measurements were facilitated by the San Diego Nanotechnology Infrastructure (SDNI) which is supported by the National Science Foundation (NSF) to Nano3 (Grant ECCS-1542148).

Chapter 3, in part or in full, is reprinted with permission from J. Y. Choi, C. F. Ahles, K. T. Wong, S. Nemani, E. Yieh and A. C. Kummel, "Highly Selective Atomic Layer Deposition of $MoSiO_x$ Using Inherently Substrate-Dependent Processes" Applied Surf. Sci. (2019) (*manuscript accepted*). The dissertation author was the primary investigator and author of this paper.

3.7 Figures

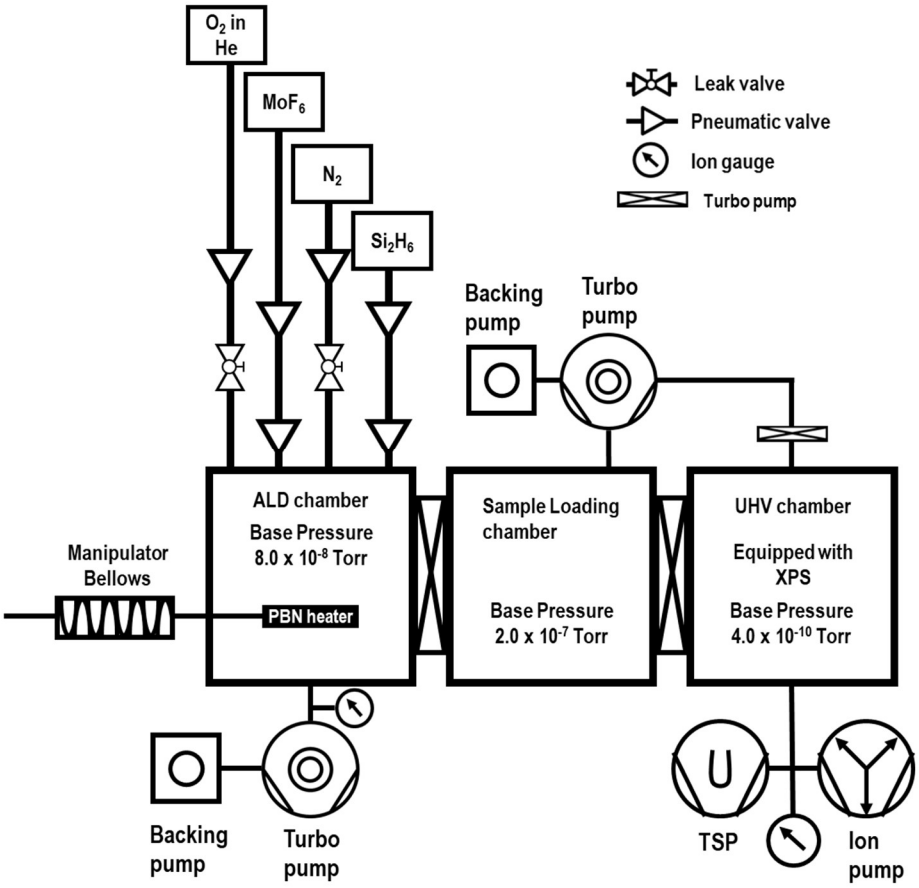

Figure 3.1. A schematic of vacuum chamber. The chamber was composed of a reaction chamber (ALD chamber), sample loading chamber, and UHV chamber equipped with X-ray photoelectron spectroscopy.

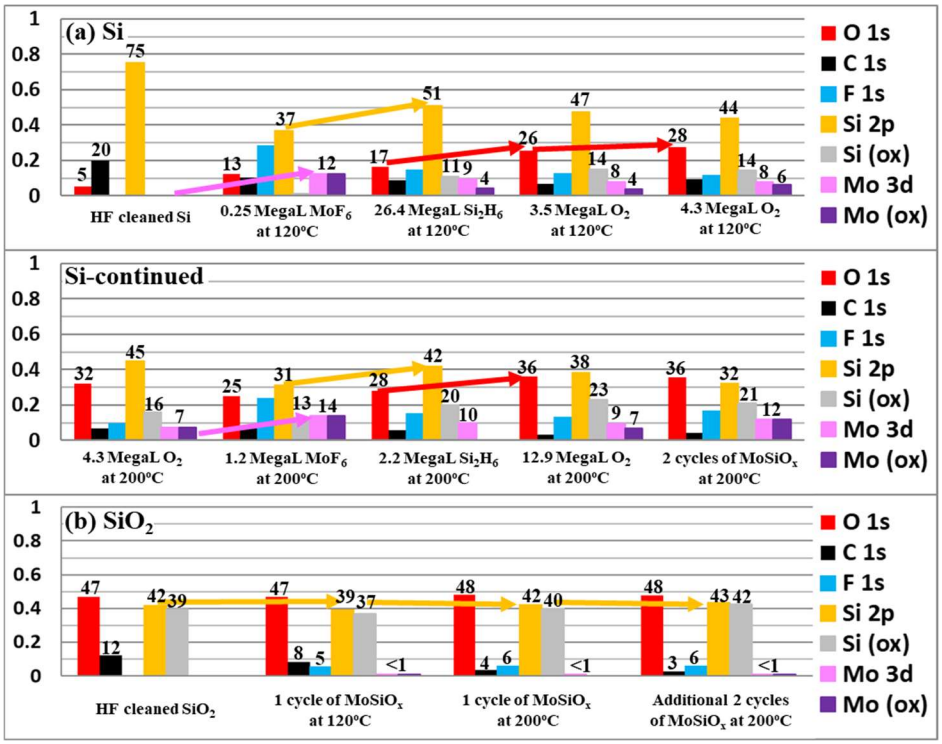

Figure 3.2. Elemental compositions at each deposition step of 3 step $MoSiO_x$ ALD. (a) At 120°C, MoF_6, Si_2H_6 and O_2 were sequentially dosed on HF cleaned Si. Mo was not fully oxidized after an ALD cycle at 120°C. Additional dosing with 4.3 MegaL of O_2 increase the fraction of oxidized Mo. The ALD process was continued on the sample at 200°C. The additional 4.3 MegaL of O_2 at 200°C fully oxidized the Mo. Additional cycles of MoF_6, Si_2H_6 and O_2 at 200°C deposited ~ 2.2 nm thick $MoSiO_x$ film with fully oxidized Mo. (b) During the same doses, HF cleaned SiO_2 shows negligible amount of Mo detected on the surface.

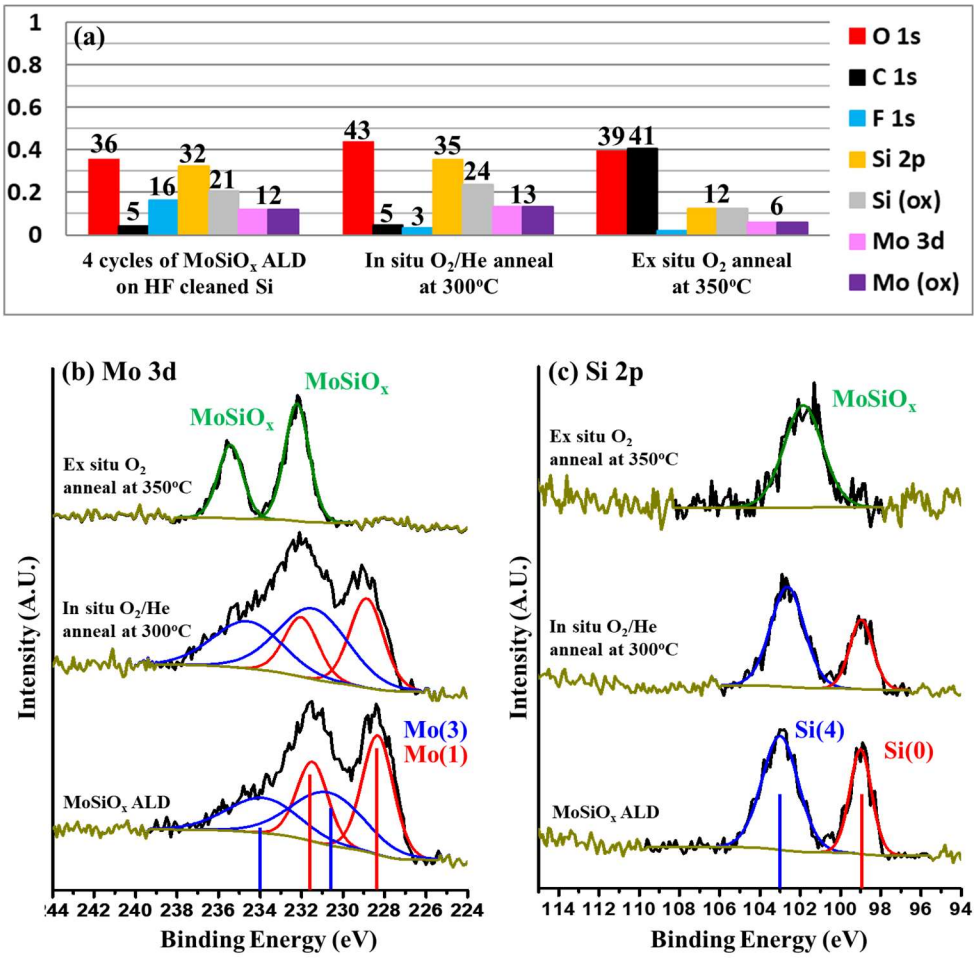

Figure 3.3. Elemental compositions and oxidation states of $MoSiO_x$ on HF cleaned Si from 3 Step ALD followed by in-situ and ex-situ O_2 post deposition anneals (PDA). (a) XPS compositions show fully oxidized Mo before and after the in-situ and ex-situ O_2 PDA. (b) Mo 3d peaks show complete oxidation of Mo after the ex-situ PDA at 350°C. (c) Si 2p peak also shows full conversion of Si into $MoSiO_x$.

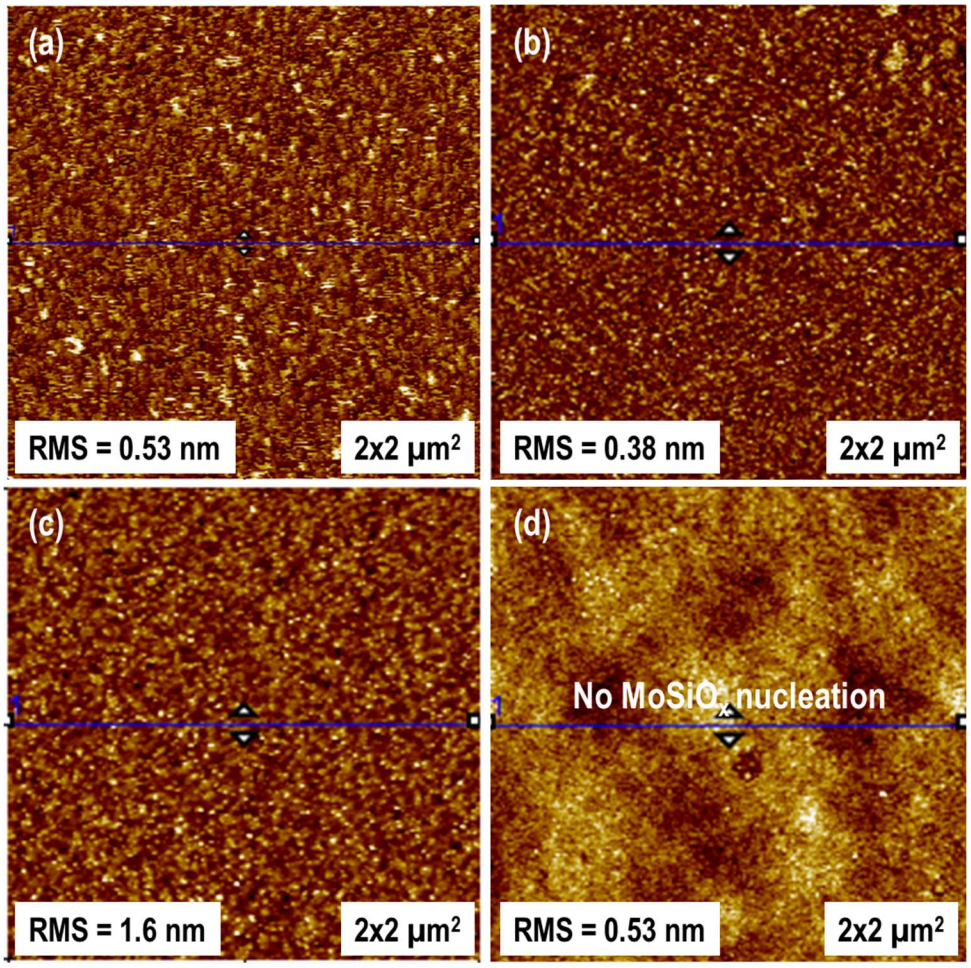

Figure 3.4. Surface morphologies of HF cleaned Si and SiO_2 after 3 step ALD $MoSiO_x$ deposition. (a) AFM image of the as-deposited $MoSiO_x$ film on HF-Si was atomically flat. (b) AFM after an in-situ O_2/He anneal at 300°C / $MoSiO_x$ / HF-Si showed a conformal film. (c) After an ex-situ O_2 anneal at 350°C, the $MoSiO_x$ surface on HF-Si was roughened with ~12 nm tall agglomerations. (d) SiO_2 after the $MoSiO_x$ ALD cycles followed by an in-situ O_2/He anneal at 300°C shows a flat SiO_2 surface without any $MoSiO_x$ nuclei.

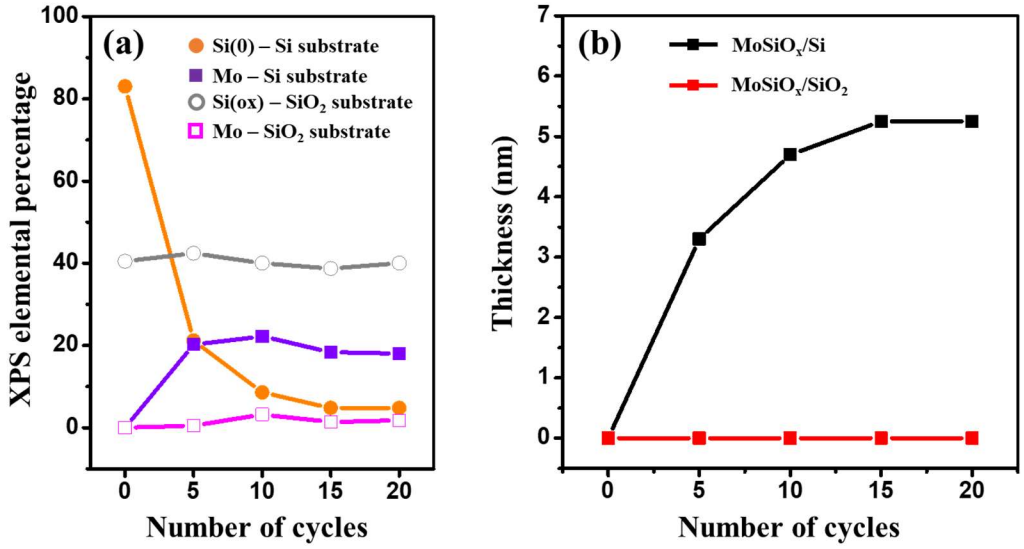

Figure 3.5. XPS elemental percentage of Si and Mo and the $MoSiO_x$ film thickness on Si and SiO_2 for 3 step ALD $MoSiO_x$. (a) The Si substrate peak (Si(0)) was attenuated as the number of cycles increased while the SiO_2 substrate peak (Si(ox)) remained the constant which is consistent with the selective growth of $MoSiO_x$ deposition. (b) The growth of $MoSiO_x$ on Si was limited up to 5.25±0.5 nm. There was no growth of $MoSiO_x$ on SiO_2. The film thicknesses were calculated using the attenuation of the substrates.

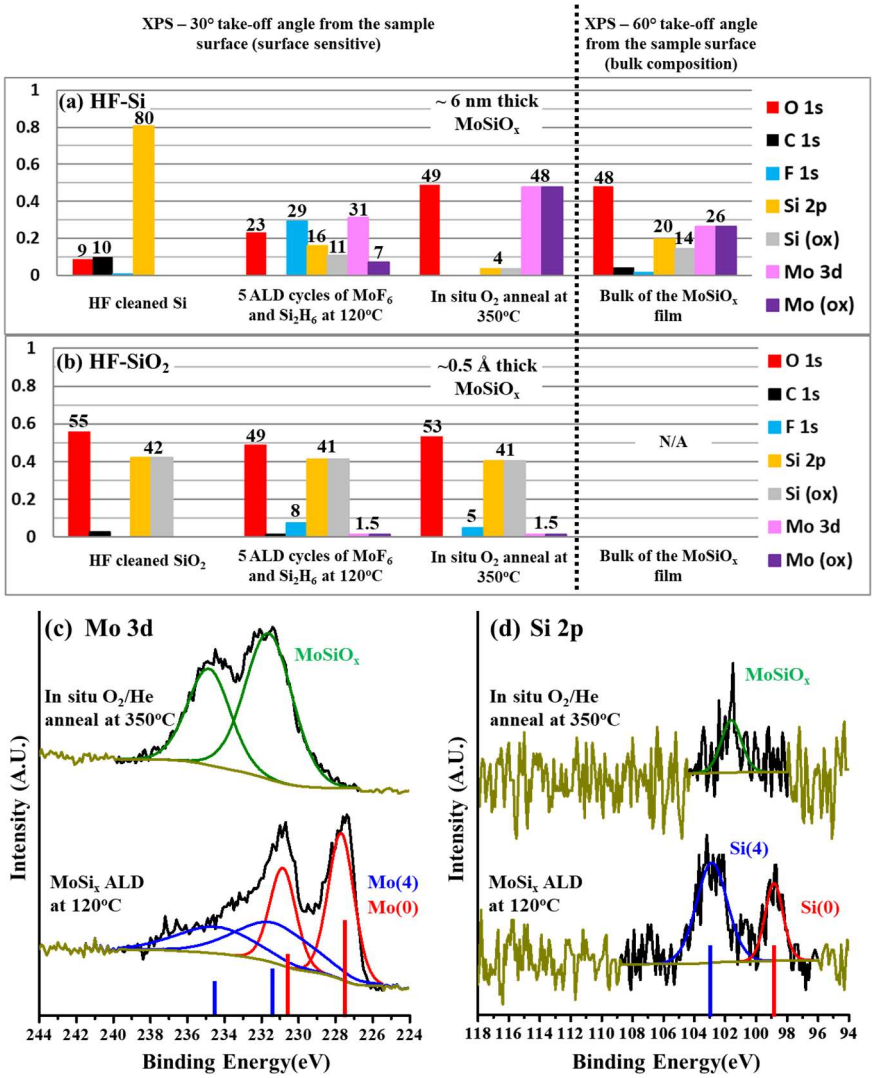

Figure 3.6. Elemental compositions at each deposition step of 2 Step $MoSi_x$ + in-situ O_2/He anneal on Si and SiO_2. (a) 5 ALD cycles of MoF_6 and Si_2H_6 at 120°C followed by an in-situ O_2/He anneal at 350°C were performed on HF cleaned Si. (b) 5 ALD cycles of $MoSi_x$ ALD at 120°C and an in-situ O_2/He anneal at 350°C on HF cleaned SiO_2. (c) The raw Mo 3d XPS spectra after $MoSi_x$ deposition at 120°C followed by the in-situ O_2/He anneal at 15 Torr at 350°C. (d) The raw Si 2p XPS spectra after MoSix deposition at 120°C followed by the in-situ O_2/He anneal at 15 Torr at 350°C.

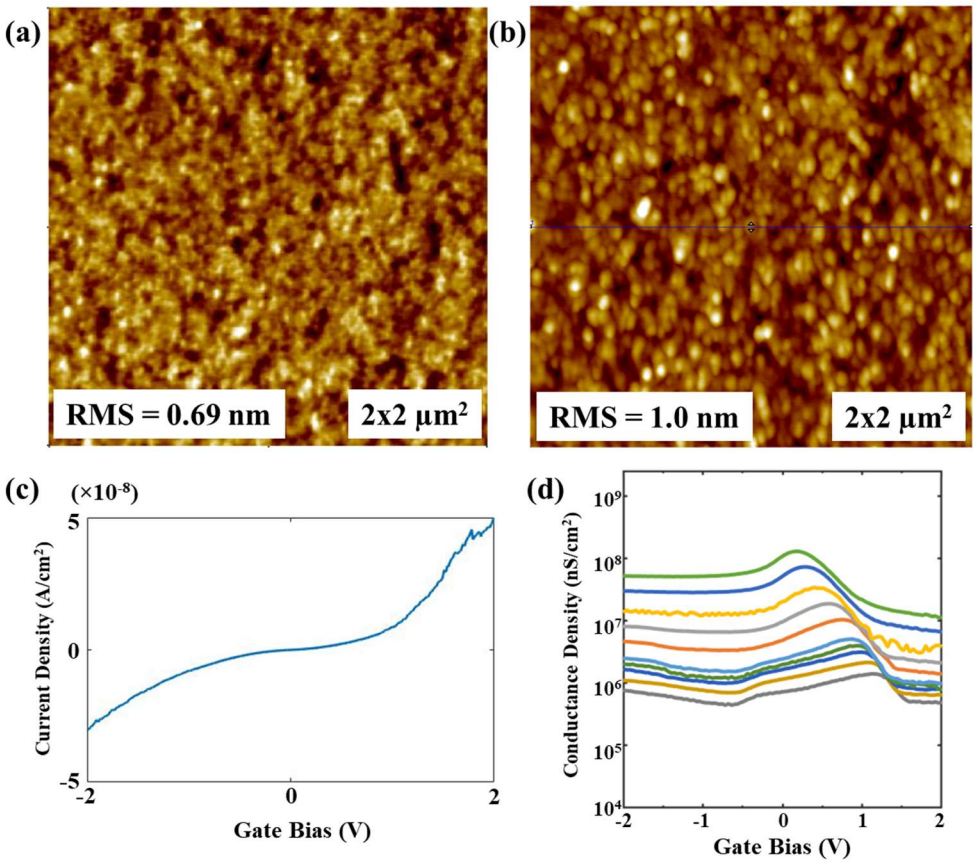

Figure 3.7. Surface morphologies of 2 Step ALD $MoSiO_x$ before and after the in-situ O_2/He anneal at 350°C and its electrical properties. (a) The surface morphology of an as-deposited $MoSi_x$ film on Si. (b) The surface morphology of $MoSiO_x$ after the in-situ O_2/He anneal at 350°C. (c) I-V curve of the $MoSiO_x$ film. (d) G-V curve of the $MoSiO_x$ film. Sweeping mode from 10kHz to 1 MHz frequency was used at -2 ~ 2 V gate bias.

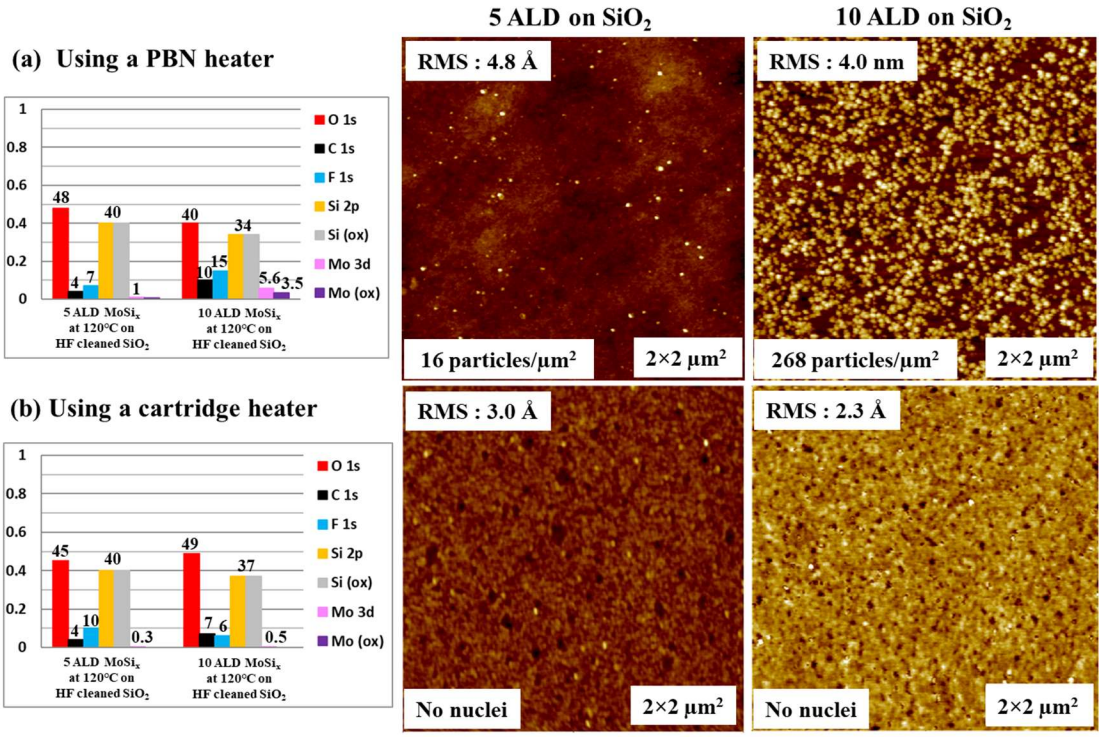

Figure 3.8. Improvement of selectivity of 2 Step ALD $MoSi_x$ on SiO_2 using a cartridge heater compared to a PBN heater. (a) XPS chemical composition and AFM images of SiO_2 after 5 and 10 ALD cycles of $MoSi_x$ at 120°C using a PBN heater. (b) the XPS chemical composition and AFM images of SiO_2 after 5 and 10 ALD cycles of $MoSi_x$ at 120°C using a cartridge heater.

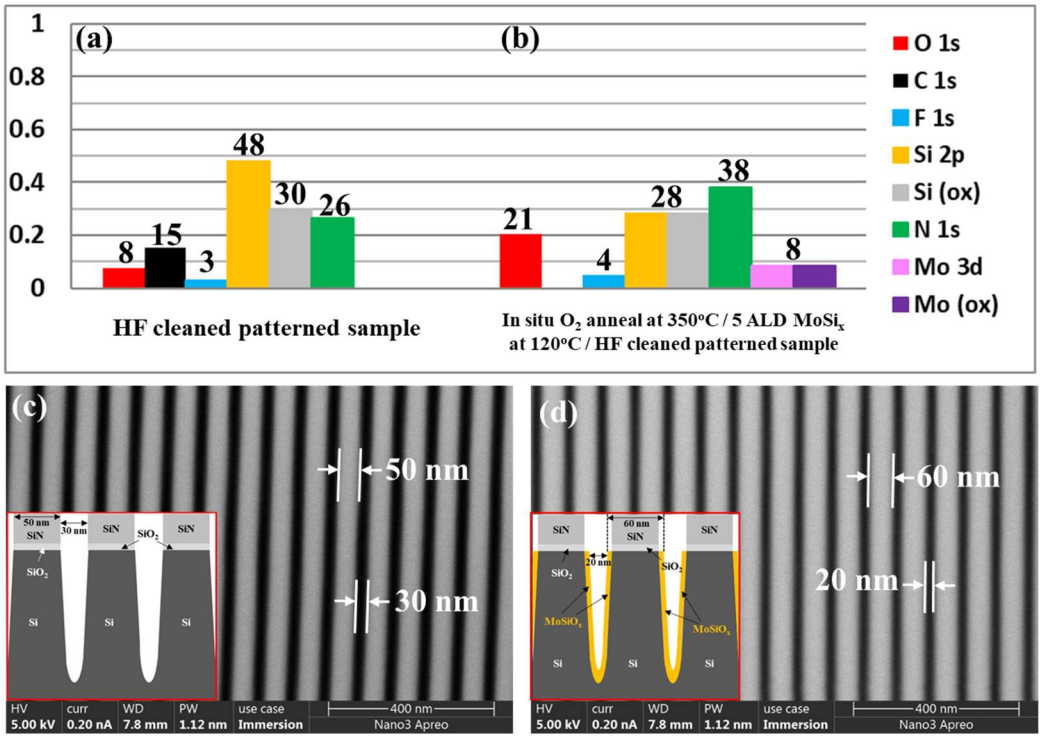

Figure 3.9. XPS elemental composition and SEM images of a patterned sample before and after selective 2 Step ALD $MoSiO_x$ + PDA deposition. (a) HF cleaned patterned sample mostly has SiN and Si(0) components. (b) After the selective $MoSiO_x$ deposition, there was $MoSiO_x$ together with SiN. (c) A top view SEM image of the HF cleaned patterned sample shows that the patterned sample had ~50 nm and ~30 nm trough structure. The insert is a schematic of the cross sectional patterned sample. (d) SEM image of the patterned sample after the $MoSiO_x$ deposition. The insert is a schematic of the cross-sectional patterned sample with $MoSiO_x$ deposition. After ALD, the patterned sample had ~60 nm and ~20 nm trough structure consistent with 5nm of ALD on the side walls.

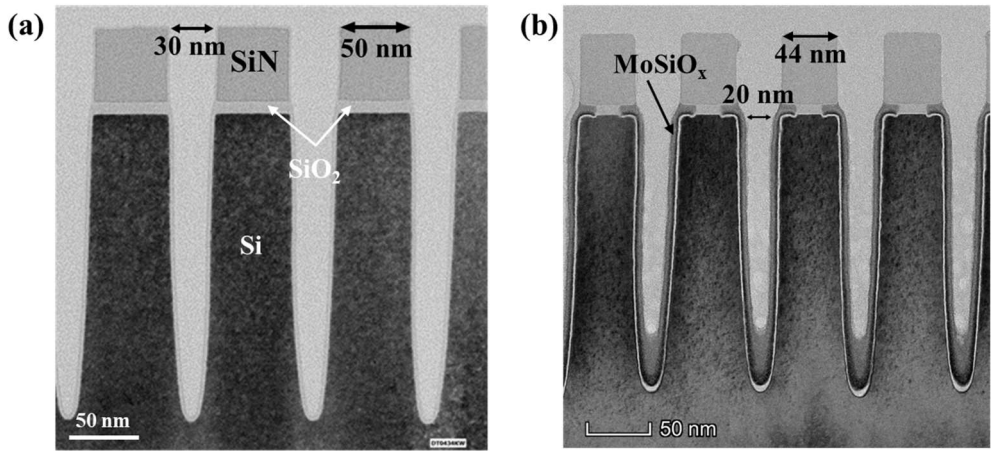

Figure 3.10. Cross-sectional TEM image of the patterned sample before and after the selective 2 Step ALD $MoSiO_x$ + PDA deposition. (a) The patterned sample had Si fins covered with a SiN mask. There was a SiO_2 interlayer in between. (b) After the 5% HF clean followed by the $MoSiO_x$ deposition, $MoSiO_x$ was selectively deposited on the sidewalls of the Si fins. Note that a wet etch in 5% HF solution before the $MoSiO_x$ deposition etched the SiN and SiO_2 features.

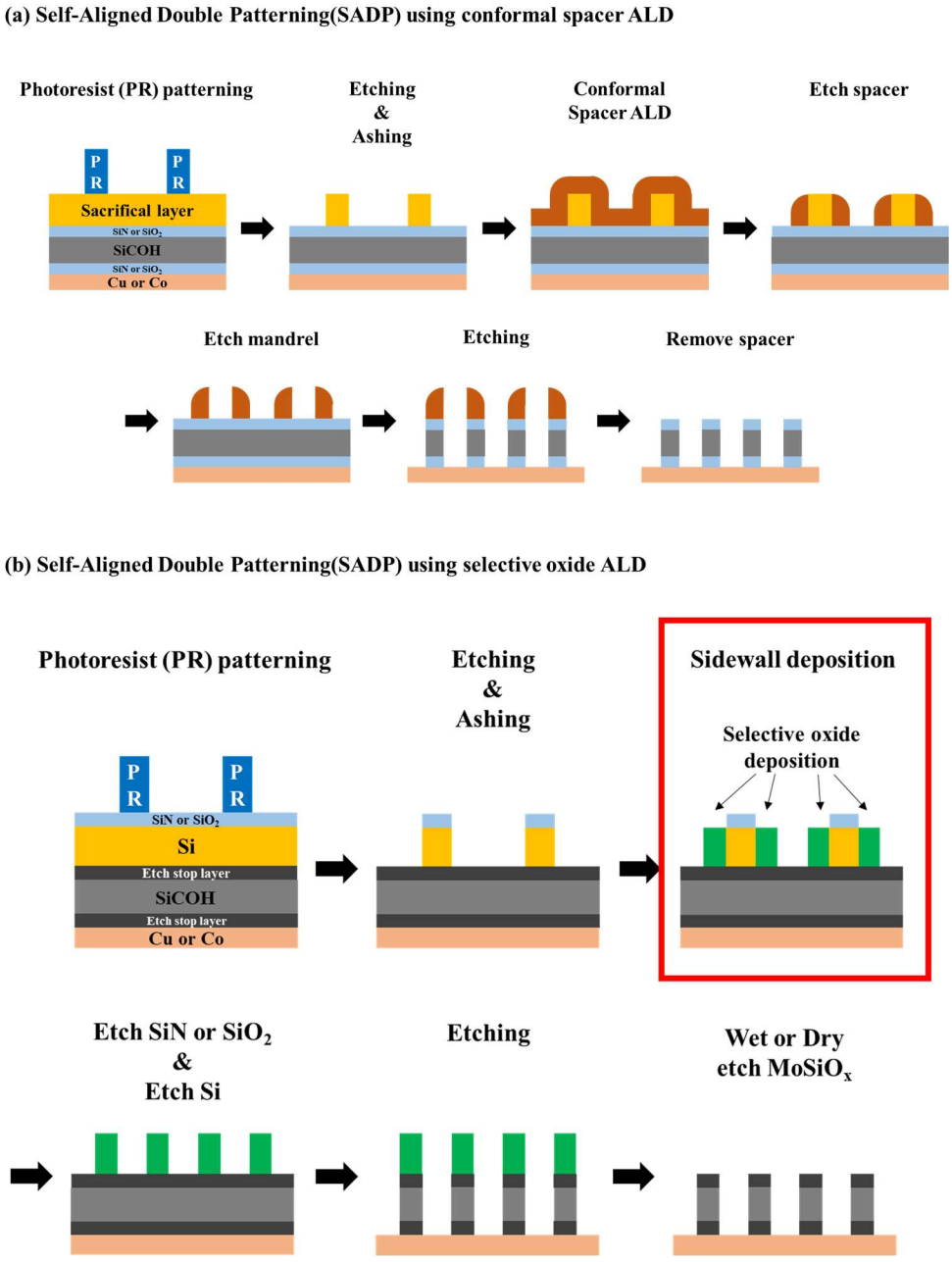

Figure 3.11. A diagram of a self-aligned double patterning (SADP) process. (a) SADP using a conformal spacer ALD requires another etching step to leave the spacer only on the sidewalls of the mandrels. (b) Selective deposition can initially deposit an oxide film only on the sidewall of mandrels (red box).

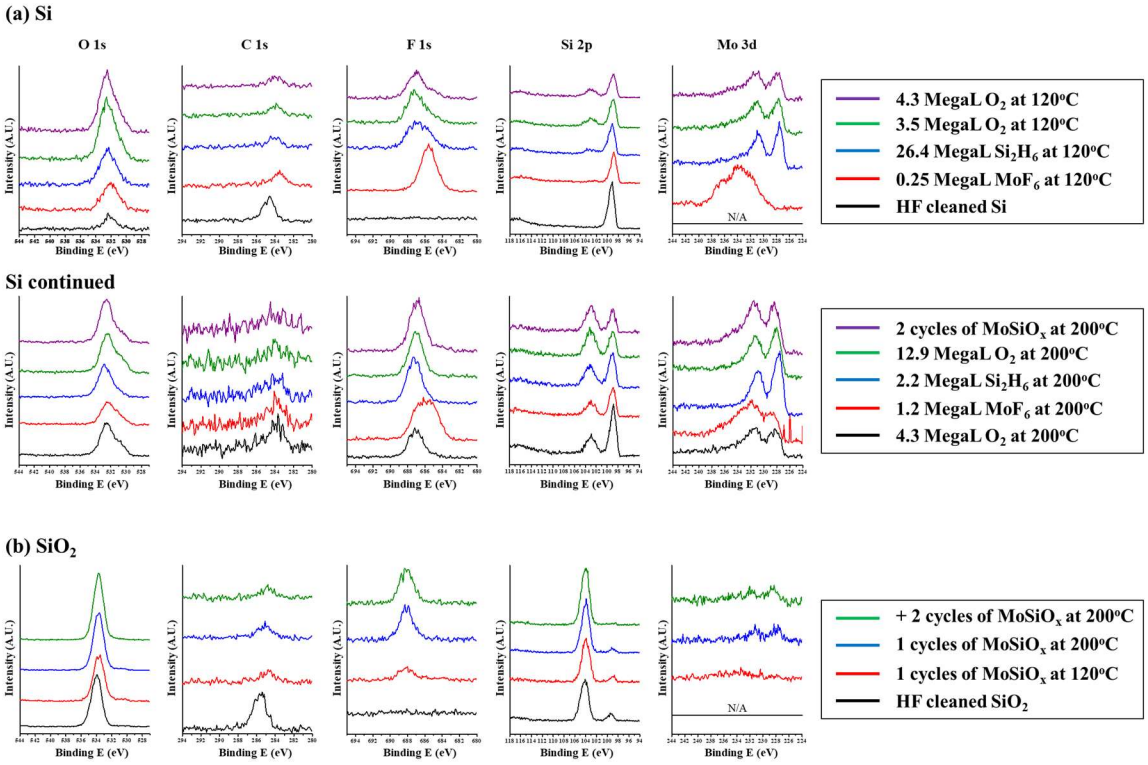

Figure 3.12. XPS spectra of Si and SiO_2 at each deposition step of 3 step $MoSiO_x$ ALD.

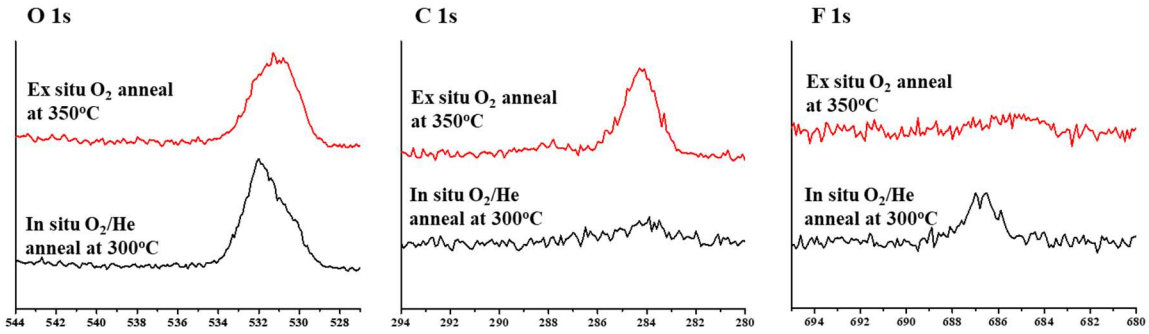

Figure 3.13. XPS spectra of $MoSiO_x$ on HF cleaned Si from 3 Step ALD followed by in-situ and ex-situ O_2 post deposition anneals (PDA).

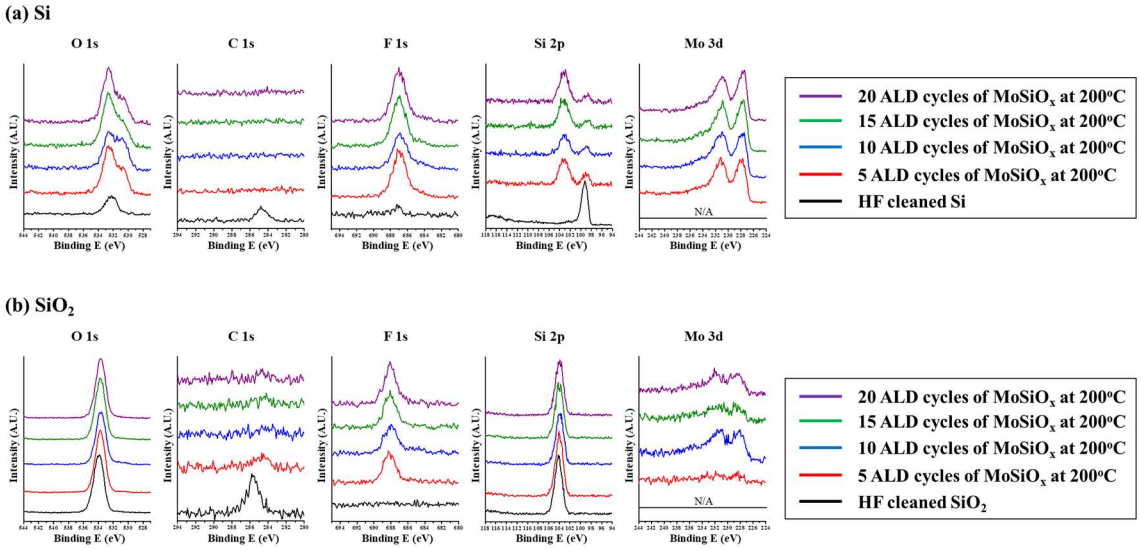

Figure 3.14. XPS spectra of Si and SiO_2 after 5, 10, 15 and 20 cycles of 3 step ALD $MoSiO_x$ at 200°C.

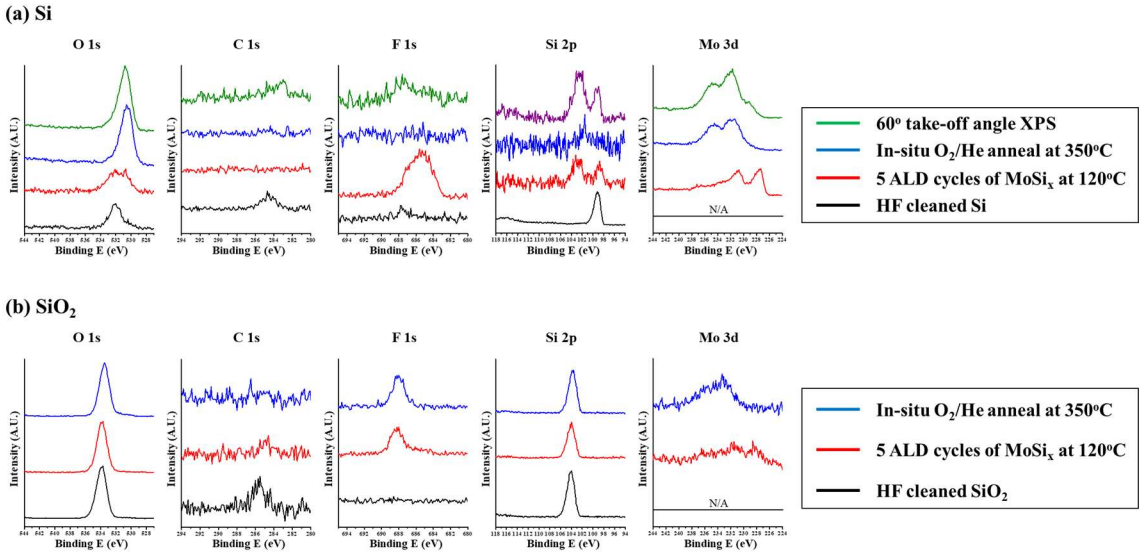

Figure 3.15. XPS spectra of Si and SiO_2 at each deposition step of 2 Step $MoSi_x$ + in-situ O_2/He anneal.

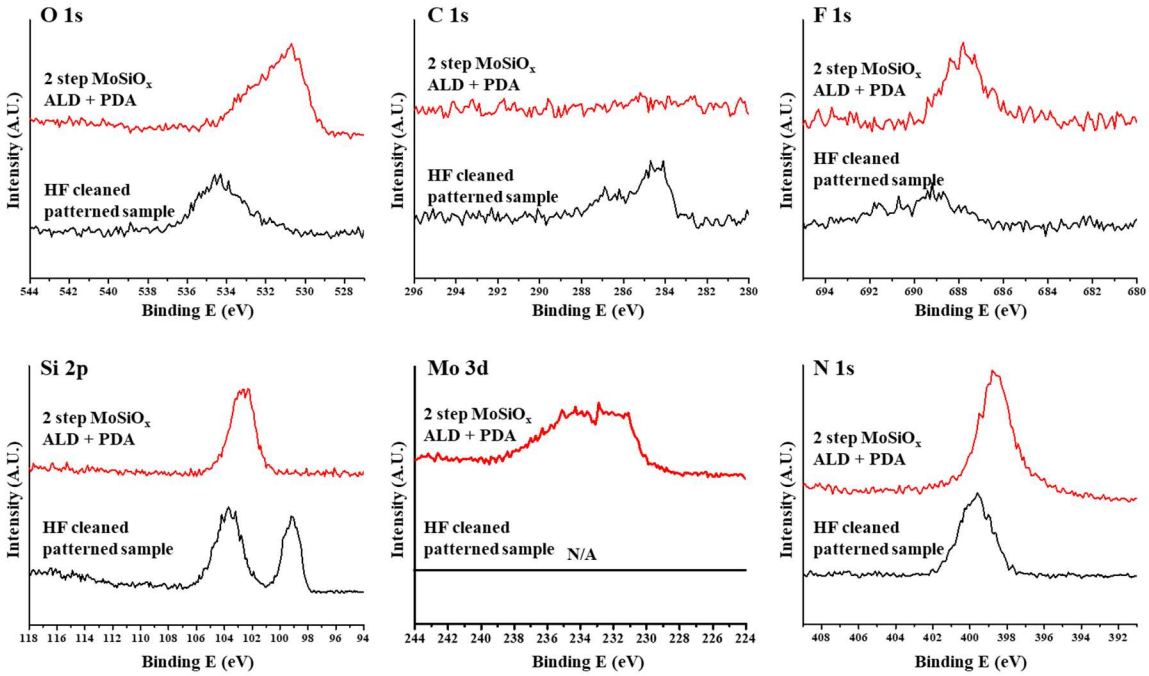

Figure 3.16. XPS spectra of a patterned sample before and after selective 2 Step ALD $MoSiO_x + O_2$ PDA deposition.

3.8 References

(1) A. J. M. Mackus; A. A. Bol; W. M. M. Kessels, Nanoscale **2014**, 6, 10941.

(2) L. Li; X. Liu; S. Pal; S. Wang; C. K. Ober; E. P. Giannelis, Chem. Soc. Rev. **2017**, 46, 4855.

(3) J. A. DeFranco; B. S. Schmidt; M. Lipson; G. G. Malliaras, Organic Electronics **2006**, 7, 22

(4) S. Liu; A. Al-Shadeedi; V. Kaphle; C.-M. Keum; B. Lüssem, Organic Electronics **2017**, 45, 124.

(5) K. R. Williams; K. Gupta; M. Wasilik, J. Microelectromech. Syst. **2003**, 12, 761.

(6) A. J. M. Mackus; M. J. M. Merkx; W. M. M. Kessels, Chem. Mater. **2019**, 31, 2

(7) X. Liu; S. Ramanathan; A. Longdergan; A. Srivastava; E. Lee; T. E. Seidel; J. T. Barton; D. Pang; R. G. Gordonb, Journal of The Electrochemical Society **2005**, 152, G213.

(8) S. W. Park; J. Y. Choi; S. Siddiqui; B. Sahu; R. Galatage; N. Yoshida; J. Kachian; A. C. Kummel, J. Chem. Phys. **2017**, 146, 052808.

(9) H. B. Profijt; P. Kudlacek; M. C. M. van de Sanden; W. M. M. Kessels, J. Electrochem. Soc. **2011**, 158, G88.

(10) X. Wang; S. M. Tabakman; H. Dai, J. am. chem. soc. **2008**, 130, 8152.

(11) J. Hamalainen; F. Munnik; M. Ritala; M. Leskela, Chem. Mater. **2008**, 20, 6840.

(12) J. A. Singh; N. F. W. Thissen; W.-H. Kim; H. Johnson; W. M. M. Kessels; A. A. Bol; S. F. Bent; A. J. M. Mackus, Chem. Mater. **2018**, 30, 663.

(13) M. Ritala; K. Kukli; A. Rahtu; P. I. Raisanen; M. Leskela; T. Sajavaara; J. Keinonen, SCIENCE **2000**, 288, 319.

(14) V. R. Anderson; A. S. Cavanagh; A. I. Abdulagatov; Z. M. Gibbs; S. M. George, J. Vac. Sci. Technol. A **2014**, 32, 01A114.

(15) A. Mameli; M. J. M. Merkx; B. Karasulu; F. Roozeboom; W. M. M. Kessels; A. J. M. Mackus, ACS Nano **2017**, 11, 9303.

(16) F. S. M. Hashemi; S. F. Bent, Adv. Mater. Interfaces **2016**, 3, 1600464.

(17) R. Vallat; R. Gassilloud; B. Eychenne; C. Vallée, J. Vac. Sci. Technol. A 35 (2017) 01B104.

(18) C. Prasittichai; K. L. Pickrahn; F. S. M. Hashemi; D. S. Bergsman; S. F. Bent, ACS Appl. Mater. Interfaces **2014**, 6, 17831.

(19) S. E. Atanasov; B. Kalanyan; G. N. Parsons, J. Vac. Sci. Technol. A **2016**, 34, 01A148.

(20) J. Y. Choi; C. F. Ahles; R. Hung; N. Kim; A. C. Kummel, Appl. Surf. Sci. **2018**, 462, 1008.

Chapter 4

Selective Pulsed Chemical Vapor Deposition of Water-free HfO_x on Si in Preference to SiO_2 and SiCOH

4.1 Abstract

Water-free HfO_x was selectively deposited on Si in preference to SiCOH using $Hf(O^tBu)_4$ via a pulsed chemical vapor deposition process. The conformal HfO_x film was deposited on Si by the thermal decomposition of the precursor, and the inherent selectivity of HfO_x was retained over SiCOH until ~2 nm of HfO_x was deposited on Si at 250°C. Additional selectivity enhancement was demonstrated by employing molecular surface passivation and reversible desorption of the precursor via control of the purge time. 1,1,3,3-tetramethyldisilazane (TMDS) and Bis(dimethylamino)dimethylsilane (DMADMS) were used to passivate reactive -OH sites on SiO_2 and SiCOH to increase the selectivity to ~7 nm HfO_x deposition on Si before any significant nucleation occurred on TMDS passivated SiCOH. It is expected that the selective water-free HfO_x deposition can be used for patterning three-dimensional nanoscale structures in MOSFET devices.

4.2 Introduction

In Metal-Oxide-Semiconductor Field Effect Transistors (MOSFETs), high-k dielectric materials for gate oxide such as hafnium oxide (HfO_x) has been intensively studied for several decades. HfO_x exhibits a high dielectric constant with moisture resistance and thermal stability so that it has been employed as a gate dielectric in conventional MOSFETs as a replacement for SiO_x. [1-3] As MOSFETs are scaled down

to 14 nm nodes or less, precise control of oxide thickness while maintaining good physical, electrical qualities is required. [4,5] Therefore, atomic layer deposition (ALD) of HfO_x was employed because it provides angstrom scale thickness control with great conformality, and many successful HfO_x ALD techniques using various precursors such as $HfCl_4$, tetrakis(dimethylamido)hafnium (TDMAHf), hafnium-t-butoxide (HTBO) with H_2O, H_2O_2 and Ozone have been reported. [6-9] However, patterning of the gate dielectric with three-dimensional features such as FinFETs and Gate-all-around (GAA) transistors common in the sub 10 nm nodes is challenging. Patterning sub-10 nm 3D features require multiple steps of lithography which might lead to an unsatisfactory resolution due to an imperfect alignment of masks or limited focal plane of the EUV source.

Area-selective atomic layer deposition (AS-ALD) is an alternative method to pattern sub-10 nm features. AS-ALD selectivity relies on the differential chemical reactivity the precursors and different substrates so that spontaneous patterning is possible. Therefore, a choice of reactants for a selective oxide deposition is critical since strongly oxidizing reactants such as H_2O and H_2O_2 easily provide nucleation sites on any surface. For example, previously reported HfO_x ALD has been using water (H_2O), ozone (O_3), ammonium hydroxide (NH_4OH), hydrogen peroxide (H_2O_2) or oxygen (O_2) plasma as oxygen sources [6-12]. These oxidants are effective in forming a high quality HfO_x film due to energetically favorable reactions of -OH groups or reactive oxygen species with Hf precursors; however, they can initiate nucleation on most of the surfaces which should be avoided for selective deposition.

Anderson et al. [13] have demonstrated waterless TiO_2 ALD using $TiCl_4$ and $Ti(O^iPr)_4$, and Atanasov et al. [14] reported an inherent substrate-dependency of the

"water-free" TiO_2 process between hydrogen terminated Si (H-Si) and hydroxylated Si (OH-Si). The authors showed that eliminating strong oxidants such as water was critical to obtain selectivity by preventing oxidation of the Si-H terminated surface.

S. Sayan et al. [15] and T. S. Yang et al. [16] previously demonstrated a water-free HfO_2 deposition on Si via a single-source chemical vapor deposition (CVD) process. The authors employed a thermal decomposition of hafnium alkoxides by continuously exposing Si to the precursors; however, to the best of our knowledge, the selectivity of water-free HfO_2 deposition has never been reported.

In this study, water-free HfO_x was selectively deposited on Si in preference to SiCOH and passivated SiO_2 by employing hafnium tetra-tert-butoxide ($Hf(O^tBu)_4$) which is a source of both metal and oxygen. The HfO_x deposition was performed via a pulsed CVD process which involved the decomposition of $Hf(O^tBu)_4$. In case of CVD, a thermally pyrolyzed precursor is generally less sensitive to the initial surface condition which is not desirable for selectivity. However, unlike a conventional CVD process which continuously flows a precursor, $Hf(O^tBu)_4$ was pulsed with a purge. Pulsed CVD provides a capability of investigating the mechanism of selectivity and of expanding selectivity by allowing reversibly physisorbed adsorbants to leave from the unwanted surface without reacting. The key of this work is to demonstrate the inherently selective CVD of water-free HfO_x and its enhancement using small molecules passivants and a purge control.

4.3 Experimental

Fig. 4.1 shows a chamber schematic. A home-built reaction chamber was pumped by a turbopump (Pfeiffer TPU 062) and a backing rotary pump (Edwards RV3). The base

pressure of the reaction chamber was 8.0×10^{-7} Torr. The reaction chamber had a manipulator rod with a sample mounting platform made of Cu. A cartridge heater was used to heat the Cu platform and the samples. The precursors and N_2 purge gas had dosing lines pointing at the samples with a 3-inch separation. The dosing was performed using pneumatic valves and leak valves. The chamber wall and dosing lines for precursors were kept at 150°C. After the deposition was performed, the processed samples were transferred in-situ into a UHV chamber to characterize the chemical compositions and oxidation states of the films using X-ray photoelectron spectroscopy (XPS). The UHV chamber was pumped by an ion pump (Agilent Varian VacIon 300 StarCell) and had a base pressed of 8.0×10^{-10} Torr. The in-situ transfer was performed using the manipulators and transfer arm so that the samples were not exposed to the ambient air between the depositions and chemical analyses. For the XPS measurements, a monochromatic Al Kα X-ray source (E = 1487 eV) and a hemispherical analyzer (XM 1000 MkII/SPHERA, Omicron Nanotechnology) were employed. The anode voltage and filament emission current were set to 10 kV and 25 mA respectively with a hemisphere analyzer pass energy of 50 eV. The focused X-ray beam size on the sample was 0.7 – 1 mm in diameter. For the surface sensitive measurements, the XPS detector was aligned to 60° from the sample surface normal (i.e. near glancing), but for the detection of the bulk compositions of deposited films, 30° from the surface normal was employed. After the XPS data collection, the areas of the XPS peaks were calculated and corrected using their relative sensitivity factors reported in the Casa XPS v2.3 program. The chemical compositions were normalized to the sum of all elements. The morphology of the deposited films were analyzed using ex-situ atomic force microscopy (AFM) (Agilent 5500) in tapping mode.

Passivation of SiO_2 and SiCOH was performed in a separate vacuum chamber where the base pressure was 200 mTorr pumped by a mechanical pump (Edwards RV3). The chamber consisted of a sample stage which had a cartridge heater to heat the samples to a reaction temperature of 70°C. The chamber walls were kept at 25°C. SiO_2 samples were loaded in the passivation chamber after degreasing using acetone, methanol and HPLC grade water for 30 seconds each followed by a 30 second dip in a 0.5% HF(aq) solution. SiCOH samples were degreased using the same process but without the HF clean. 1,1,3,3-tetramethyldisilazane (TMDS) (97%, Sigma Aldrich) and Bis(dimethylamino)dimethylsilane (DMADMS) (>95%, Sigma Aldrich) were used as passivation agents. The precursor bottles were kept at room temperature. The passivants were continuously flowed into the chamber at a constant pressure of 10 Torr for 10 mins using a manual bellows valve. After the passivation process, the passivated SiO_2 and passivated SiCOH samples were removed from vacuum and quickly loaded into a sample loading chamber that was connected to the reaction chamber and UHV chamber to minimize the contamination from the air transfer.

B-doped Si (001), SiO_2 and SiCOH were degreased using acetone, methanol and HPLC water sequentially for 30 seconds. After the degrease, Si and SiO_2 were cleaned in a 0.5% HF(aq) solution for 30 seconds followed by a HPLC water rinse to remove a native oxide. A combination of two or three samples (i.e. HF cleaned Si and degreased SiCOH or HF cleaned Si, passivated SiO_2 and passivated SiCOH) were loaded together in the sample loading chamber and pumped down to the base pressure of 2.0×10^{-7} Torr. By loading two or three different substrates at the same time, direct comparison of HfO_x selectivity with

identical reaction conditions was ensured. Before the deposition, the samples were pre-annealed in the UHV chamber at the corresponding deposition temperatures.

Selective CVD of HfO_x was performed using Hafnium tert-butoxide ($Hf(O^tBu)_4$, 99.99%, Sigma Aldrich) at sample temperatures of 150-250°C. $Hf(O^tBu)_4$ was contained in a glass tube that was vacuum-sealed to a stainless steel flange and dosing line. The container was kept at 80°C to increase the vapor pressure of $Hf(O^tBu)_4$. The exposure of $Hf(O^tBu)_4$ per pulse was ~6,000 Langmuir calculated using a pressure spike detected by a convectron gauge in the reaction chamber. (1 Lanmuir (L) = 1×10^{-6} Torr × 1 second exposure of a gas). Each pulse of $Hf(O^tBu)_4$ was separated by a N_2 purge for 15 seconds. The effect of the purge time on selectivity was determined by varying the purge time between 5 – 60 seconds at 250°C. The N_2 purge gas was continuously flowed into the reaction chamber at 130 mTorr during the deposition.

4.4 Results and Discussion

4.4.1 Temperature study of HfO_x CVD on Si using XPS

HfO_x single precursor CVD using $Hf(O^tBu)_4$ was performed on HF cleaned Si at three different temperatures, 250°C, 200°C and 150°C. Removal of the native SiO_x on Si using aqueous HF is known to leave the surface Si-H terminated. [17] The HfO_x thickness was calculated using the inelastic mean free path (IMFP) and attenuation length of an electron from the Si substrate as shown below.

$$\lambda = \frac{143}{E^2} + 0.054\sqrt{E}$$

$$I = I_0 \exp(-t/\lambda \sin\theta)$$

, where E is a kinetic energy of electron, I is the intensity of the substrate signal, I_0 is the intensity of the unattenuated substrate signal, t is the thickness of the film on top of the substrate(layer depth), λ is the IMFP of the electrons coming from the substrate and θ is the angle of emitted electron from the surface.

Fig. 4.2(a) shows the XPS chemical composition of Si after sequential $Hf(O^tBu)_4$ doses at 250°C, 200°C and 150°C. As loaded HF cleaned Si had 74% Si (depicted in yellow) and all the Si was in an oxidation state of 0 (depicted in grey). There was a total of 26% adventitious hydrocarbon and oxygen on the surface. After 10 pulses of $Hf(O^tBu)_4$ at 250°C, 19% Hf and 45% O were deposited, and the Si substrate peak was attenuated to 21%. After a total of 15 pulses at 250°C, Hf and O increased to 26% and 59% and the Si substrate was attenuated to 4% which is consistent with continuous growth of HfO_x. There was 5% C on the surface consistent with the presence of butoxide ligands.

At 200°C, a HfO_x film also continuously grew as the $Hf(O^tBu)_4$ doses increased. After a total of 150 pulses, the Si substrate was completely buried and HfO_x was deposited with 13% C on the surface. Lastly, at 150°C only 4% Hf, 17% O and 23% C was deposited on Si after 125 pulses dose which indicates poor nucleation at 150°C on Si.

Fig. 4.2(b) shows the HfO_x thickness on Si as a function of $Hf(O^tBu)_4$ doses at 250°C, 200°C and 150°C. At 250°C and 200°C, HfO_x continuously grows with a growth rate of 1.48±0.12 Å/pulse and 0.47±0.02 Å/pulse, respectively. At 150°C the growth per pulse was only 0.04±0.01 Å/pulse which is consistent with poor nucleation of $Hf(O^tBu)_4$ on H-terminated Si at 150°C.

4.4.2 Selective HfO_x deposition on Si in preference to SiCOH at 200°C

At 200°C, the selective pulsed HfO_x CVD was observed on Si in preference to SiCOH as shown in Fig. 4.3. SiCOH is a highly porous silicon oxide doped with carbon with Si-CH_3 termination on the surface. [18] SiCOH is a common low-k material in nearly all logic and memory devices due to its electrical, thermal and chemical compatibility with the fabrication processes. [18-20] Fig. 4.3(a) shows the chemical compositions of Si and SiCOH after sequential doses of $Hf(O^tBu)_4$ at 200°C. After 20 pulses of $Hf(O^tBu)_4$ on HF cleaned Si, 12% Hf was deposited and O increased from 11% to 31%. The Si substrate was attenuated from 77% to 42%. After another 40 pulses, 8% of Si was present which is consistent with HfO_x deposition. In contrast, on SiCOH, 20 pulses of $Hf(O^tBu)_4$ only deposited a trace amount of Hf on the surface. An additional 40 pulses of $Hf(O^tBu)_4$ deposited 12% Hf and O increased from 38% to 46%. Si was attenuated from 31% to 17%. This indicates that HfO_x deposition at 200°C showed a nucleation delay on SiCOH which consistent with inherent selectivity. Fig. 4.3(b) shows the HfO_x thicknesses on Si and SiCOH calculated using the substrate attenuation from XPS. For the thickness calculation, it was assumed that the HfO_x film on SiCOH was conformal across the surface. The HfO_x thickness after 20 pulses of $Hf(O^tBu)_4$ on Si and SiCOH was 0.7 nm and 0.1 nm, respectively. Another 40 pulses deposited 2.4 nm of HfO_x on Si and 0.7 nm of HfO_x on SiCOH. The inherent selectivity was retained up to ~ 0.7 nm growth on Si before the HfO_x film started to grow on SiCOH.

Fig. 4.3(c) shows the raw XPS spectra of the Si 2p, O 1s and Hf 4d orbitals after HfO_x deposition at 200°C. The Si 2p peak was at an oxidation state of 0 (99.7 eV) after the HF clean. The Si peak intensity decreased as HfO_x was deposited and the Si oxidation state

mostly remained at the initial binding energy consistent with Si(0) with a trace amount of an oxidized Si component at 102.6 eV. The absence of the oxidized Si component indicates that the HfO_x CVD at 200°C occurs without oxidizing more than a monolayer of the Si surface. The O peak of Hf cleaned Si was at 532.4 eV which corresponds to the H-C-O bonding from the adventitious hydrocarbon and the O peak shifted to 531.6 eV consistent with Hf-O bonds. The Hf 4d (214.2 eV and 225.2 eV) peaks became larger in intensity as the number of pulses increased showing the continuous growth of HfO_x.

4.4.3 Surface morphology of HfO_x deposited at 200°C

The surface morphology of the deposited HfO_x film on Si and SiCOH was evaluated using AFM depicted in Fig. 4.4. Fig. 4.4(a-b) shows the surface morphologies of HF cleaned Si before and after the HfO_x deposition at 200°C. The HF cleaned Si surface was flat with a root mean square (RMS) roughness of 8.3 Å. After a total of 60 $Hf(O^tBu)_4$ pulses at 200°C, the HfO_x film was conformal with an RMS roughness of 2.1 Å. An AFM image of degreased SiCOH had < 2 nm tall chain-like features on the surface which might be due to the porous structure of the film and cross-linking of O-Si-C_xH_y surface termination groups (Fig. 4.4(c)). [21,22] Fig. 4.4(d) shows the SiCOH surface after 60 pulses of $Hf(O^tBu)_4$ at 200°C. The surface was smooth with a chain-like feature with an RMS roughness of 4.2 Å.

4.4.4 Strategies for improving selectivity

The inherent selectivity of HfO_x on Si was less than 1 nm before growth took place on SiCOH at 200°C. The selectivity loss could be due to: (1) defect sites (reactive -OH

sites) on SiCOH and/or (2) lack of thermal energy or time for $Hf(O^tBu)_4$ to desorb from SiCOH which can initiate nucleation. To test the first hypothesis that the defect sites initiated nucleation of HfO_x, TMDS and DMADMS were employed to passivate the active -OH sites on SiCOH. The possible chemical reactions are:

$(Si\text{-}OH)_4^* + [(CH_3)_2SiH]_2NH(g) \rightarrow [(Si\text{-}O)_2\text{-}Si(CH_3)_2]_2^* + 2H_2(g) + NH_3(g)$ for TMDS

and

$(Si\text{-}OH)_2^* + [(CH_3)_2N]_2Si(CH_3)_2(g) \rightarrow (Si\text{-}O)_2\text{-}Si(CH_3)_2^* + 2(CH_3)_2NH(g)$ for DMADMS

, where the asterisk indicates surface species.

$S = T_G/T_{NG}$ was used as a metric of the selectivity, where T_G is the HfO_x thickness on the growth area and T_{NG} is the HfO_x thickness on the non-growth area. The growth area was Si and the non-growth areas were SiCOH and passivated SiO_2. The HfO_x thicknesses were calculated using the XPS attenuation method and ellipsometry. As a control, HfO_x deposition was also performed on OH-terminated SiO_2 (HF cleaned SiO_2) at 200ºC. A control sample of OH-terminated SiO_2 showed the same growth rate of HfO_x as on Si which had a selectivity metric of S=1.1±0.1.

Fig. 4.5(a) shows the selective HfO_x deposition on Si in preference to TMDS passivated SiO_2 (TMDS-SiO_2) and DMADMS passivated SiO_2 (DMADMS-SiO_2) using XPS at 200ºC. After 20 pulses of $Hf(O^tBu)_4$ pulses at 200ºC, 2.9±0.6 nm HfO_x was deposited on Si (T_G) and the selectivities were S=2.2±0.7 for DMADMS-SiO_2, and S=14.5±3.3 for TMDS-SiO_2. This significant improvement in selectivity compared to OH-terminated SiO_2 indicates that TMDS is highly effective for passivating -OH groups on the surface. For greater oxide thickness on Si (T_G=10.7±0.1 nm), the selectivity for TMDS decreased while the selectivity for DMADMS increased from S=2.2±0.7 at T_G =2.9±0.6

nm to 4.1±1.5 at T_G=10.7±0.1 nm. In Fig. 4.5(b), the selectivity of different combinations of passivants and substrates were compared as a function of HfO_x thickness on Si. (D+T) denotes a sequential passivation using DMADMS followed by TMDS and (T+D) denotes a sequential passivation using TMDS followed by DMADMS. (D+T) SiO_2 showed similar selectivity to TMDS while (T+D) SiO_2 exhibited a similar selectivity as DMADMS-SiO_2 consistent with the final passivant dominating the chemistry due to reversible bonding during the passivation process.

To study the hypothesis that reversible adsorption of the Hf precursor on SiCOH initiates the nucleation, selective HfO_x deposition at 250°C was performed with different purge times between the $Hf(O^tBu)_4$ pulses. The purge time between the doses was varied from 5 to 60 sec. Fig. 4.6(a) shows the timing scheme of the $Hf(O^tBu)_4$ dosing process with example purge times of 5 s and 60 s. N_2 purge gas was continuously flowed at 130 mTorr. The HfO_x thicknesses on SiCOH were plotted with respect to the HfO_x thickness on Si in Fig. 4.6(b). At 250°C, with 5 second and 15 second purge times, there was 1 nm HfO_x deposition on Si before a monolayer of HfO_x (~0.25 nm) was deposited on SiCOH which was similar to the selectivity at 200°C. The selectivity was greatly improved by increasing the purge time to 30 s as shown by the selectivity loss on SiCOH being delayed until ~2.3 nm of HfO_x deposited on Si. 60 s purge time further increased the selectivity, giving S = 13.6±0.5 at 3.4±0.1 nm of HfO_x on Si. This corresponds to a monolayer of HfO_x deposition on SiCOH. The data is consistent with reversible molecular chemisorption of the Hf precursor on the SiCOH surface.

4.4.5 Surface morphology of HfO_x deposited at 250°C

The surface morphologies of Si and SiCOH were investigated using AFM after the selective HfO_x deposition at 250°C with 60 s purge time. Fig. 4.7(a) shows the Si surface after deposition of a 5.2 nm thick HfO_x film. The HfO_x film was conformal with an RMS roughness of 3.8 Å but there were a few ~3 nm tall particles. Fig. 4.7(b) shows the SiCOH surface after ~ 0.6 nm of HfO_x was deposited. HfO_x on SiCOH was also conformal and there were also ~ 6 nm tall particles observed. The particle formation may be due to gas phase or walls reactions since they occur on all surfaces and might be suppressed by better reactor design to avoid wall reaction product from impinging on the wafer.

4.4.6 Optimized selectivity of HfO_x on TMDS passivated SiCOH

Since TMDS was most effective at passivating -OH groups on SiO_2 and 60 s purge time could delay the nucleation on SiCOH, HfO_x deposition with 60 s purge time was performed on TMDS passivated SiO_2 and TMDS passivated SiCOH as shown in Fig. 4.8. A total of 20 pulses of $Hf(O^tBu)_4$ deposited 7.5±0.1 nm thick HfO_x on Si (Fig. 4.8(a) as measured by ellipsometry). In contrast, there were only 7% Hf and 3% Hf detected on TMDS-SiO_2 and TMDS-SiCOH, corresponding to 0.27±0.03 nm and 0.12±0.02 nm thick HfO_x respectively as calculated by the attenuation of the substrates in XPS. The selectivity metrics were S=28±1.9 for TMDS-SiO_2 and S=62±4.6 for TMDS-SiCOH both at 7.5±0.1 nm HfO_x on Si.

4.4.7 The mechanism of selectivity

The proposed mechanism of the selective HfO_x deposition is shown in Fig. 4.9. Fig. 4.9(a) shows a growth mechanism of HfO_x on Si using $Hf(O^tBu)_4$. $Hf(O^tBu)_4$ first molecularly adsorbs on the H-terminated Si surface and decomposes. The decomposition temperature of $Hf(O^tBu)_4$ is ~200°C. [15] Once the precursor decomposes, the butoxide ligands leave as isobutylene ($C_2H_2(CH_3)_2$) and $Hf(O^tBu)_4$ transforms to $Hf(O^tBu)_xOH_{4-x}$. Subsequently, OH groups can react with H-Si bonds to form Si-O-$Hf(O^tBu)_x$. This decomposition of $Hf(O^tBu)_4$ is necessary to deposit HfO_x on Si since the nucleation of HfO_x does not readily occur on H-Si at 150°C which is below the decomposition temperature as shown in Fig. 4.2. As the $Hf(O^tBu)_4$ decomposes, the HfO_x film can continuously grow via a reaction of surface-bound $Hf(OH)_x$ and $Hf(O^tBu)_4$. Fig. 4.9(b) shows a model for the degreased SiCOH surface after $Hf(O^tBu)_4$ dosing. $Hf(O^tBu)_4$ first reversibly and molecularly adsorbs on the surface and decomposes at >200°C. However, since the surface is terminated with O-Si-CH_3 groups, $Hf(O^tBu)_x(OH)_{4-x}$ readily desorbs from the surface without reacting with O-Si-CH_3 bonds. This is consistent with top-most Si atoms being bonded to O (Si-O: 798 kJ/mol) and C (Si-C: 435 kJ/mol) which are harder to break compared to Si-H bonds (298 kJ/mol). [23] In addition, the Hf atom in $Hf(O^tBu)_4$ is already bonded to four oxygens with strong bond energy of 791 kJ/mol. [23] The energetical stability of both the SiCOH surface and the Hf metal atoms of the precursor impede HfO_x nucleation on the SiCOH surface while the CH_3 termination reduces the physisorption energy promoting desorption. However, the surface passivation of SiCOH is not perfect so the adsorbed precursor may diffuse and react with the defect -OH sites. This is consistent with better selectivity after passivation by TMDS.

Fig. 4.9(c) depicts the $Hf(O^tBu)_4$ reaction on passivated SiO_2 using TMDS or DMADMS. Both TMDS and DMADMS react with OH-terminated SiO_2 and ideally form O-Si-CH_3 surface terminations. This is the same surface condition as SiCOH in terms of the topmost Si atoms on the surface bonded to O and CH_3. The subsequent $Hf(O^tBu)_4$ adsorption followed by the decomposition and desorption from the passivated surface is analogous to those on SiCOH in Fig. 4.9(b).

4.5 Conclusions

Hafnium oxide (HfO_x) was selectively deposited on Si in preference to SiCOH and passivated SiO_2 using $Hf(O^tBu)_4$. The inherent selectivity has benefited from the water-free process since commonly used oxygen sources such as H_2O or H_2O_2 can readily physisorb or chemisorb on any surface to initiate nucleation which is undesirable for selectivity. It was demonstrated that pulsed CVD allows for the $Hf(O^tBu)_4$ precursor to reversibly molecularly physisorb on SiCOH and the use of passivation molecules together with careful control of purge time is critical to improve the selectivity of the water-free oxide CVD.

HfO_x deposition using a pulsed single precursor CVD of $Hf(O^tBu)_4$ showed excellent selectivity (S=62, 7.5 nm HfO_x deposition on Si as opposed to 0.1 nm deposition on TMDS passivated SiCOH) and avoided substrate oxidation since it does not require H_2O as an O source. The methods to control the reversible adsorption of the precursor to improve selectivity could be integrated into the patterning process for sub-10 nm MOSFETs with three-dimensional structures.

4.6 Acknowledgements

Funding support from Applied Materials is gratefully acknowledged. The electrical measurements were facilitated by the San Diego Nanotechnology Infrastructure (SDNI) which is supported by the National Science Foundation (NSF) to Nano3 (Grant ECCS-1542148).

Chapter 4, is in part or full, reprinted with permission from J. Y. Choi, C. F. Ahles, Y. Cho, A. Anurag, K. T. Wong, S. Nemani, E. Yieh and A. C. Kummel, "Selective Pulsed Chemical Vapor Deposition of Water-free HfO_x on Si in Preference to SiO_2 and SiCOH" (*manuscript in preparation)*. The dissertation/thesis author was the primary investigator and author of this paper.

4.7 Figures

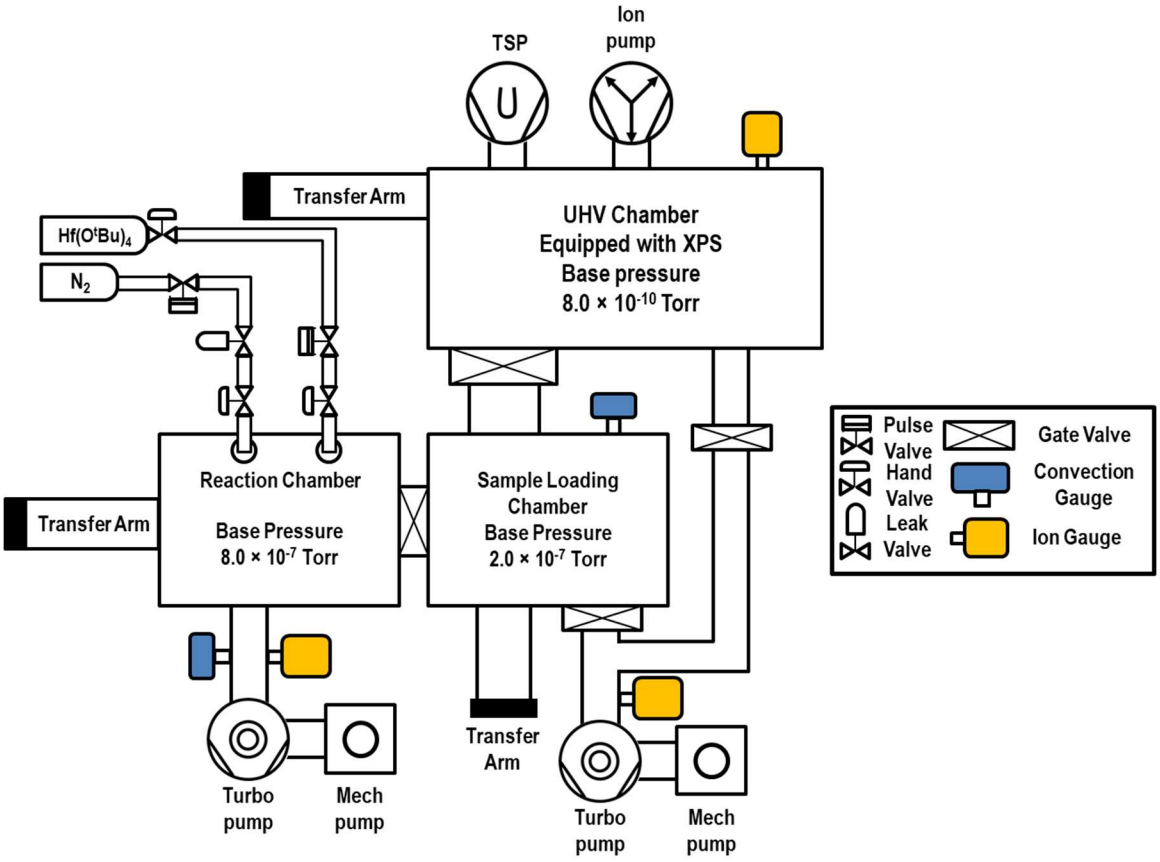

Figure 4.1. A schematic of the vacuum system. The chamber consisted of a reaction chamber, sample loading chamber and UHV chamber equipped with X-ray photoelectron spectroscopy.

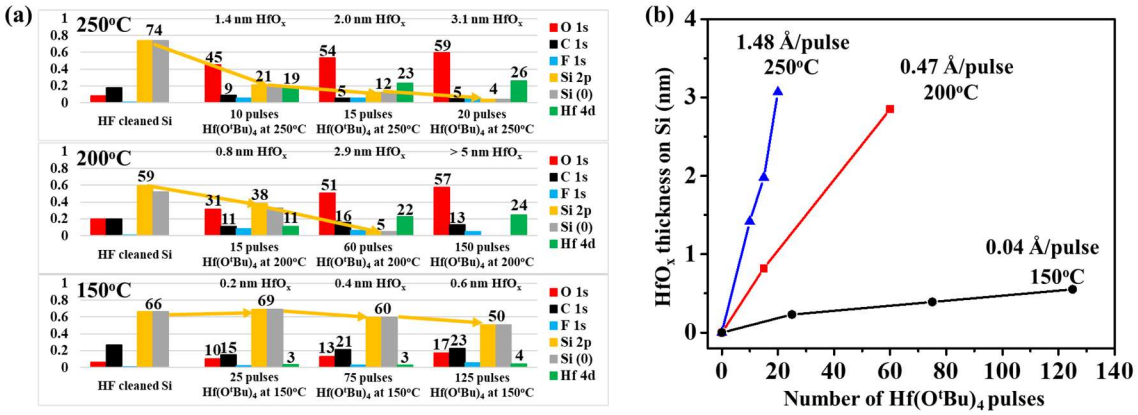

Figure 4.2. XPS elemental compositions and the growth rates of HfO_x on H-terminated Si at 250°C, 200°C and 150°C. (a) Elemental composition of HF cleaned Si after sequential doses of $Hf(O^tBu)_4$ at 250°C, 200°C and 150°C. The elemental composition is normalized to the sum of all elements. (b) The growth rate of HfO_x on H-terminated Si using $Hf(O^tBu)_4$ at 250°C, 200°C and 150°C.

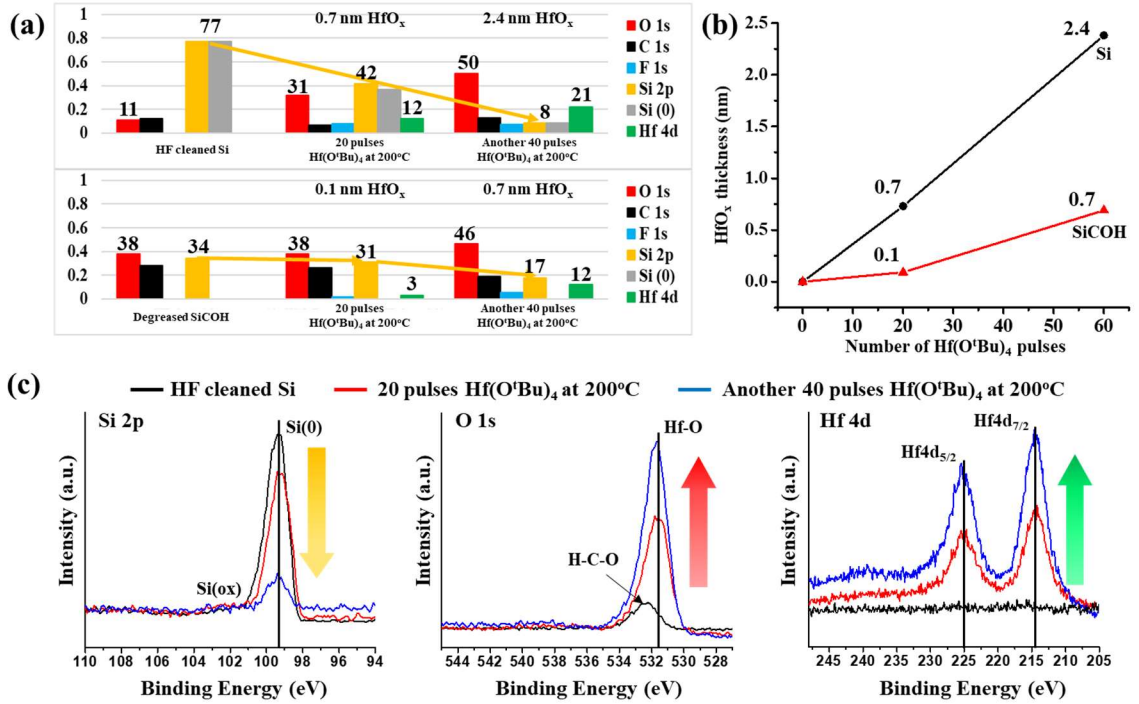

Figure 4.3. Selective HfO_x deposition on Si in preference to SiCOH at 200°C. (a) XPS elemental compositions showed that HfO_x was selectively deposited on Si at 200°C. (b) HfO_x thicknesses on Si and SiCOH were plotted as a function of $Hf(O^tBu)_4$ doses at 200°C. ~0.7 nm HfO_x was deposited on Si before nucleation occurred on SiCOH. (c) Raw XPS data of Si 2p, O 1s and Hf 4d show that HfO_x was deposited without forming significant SiO_x at the interface.

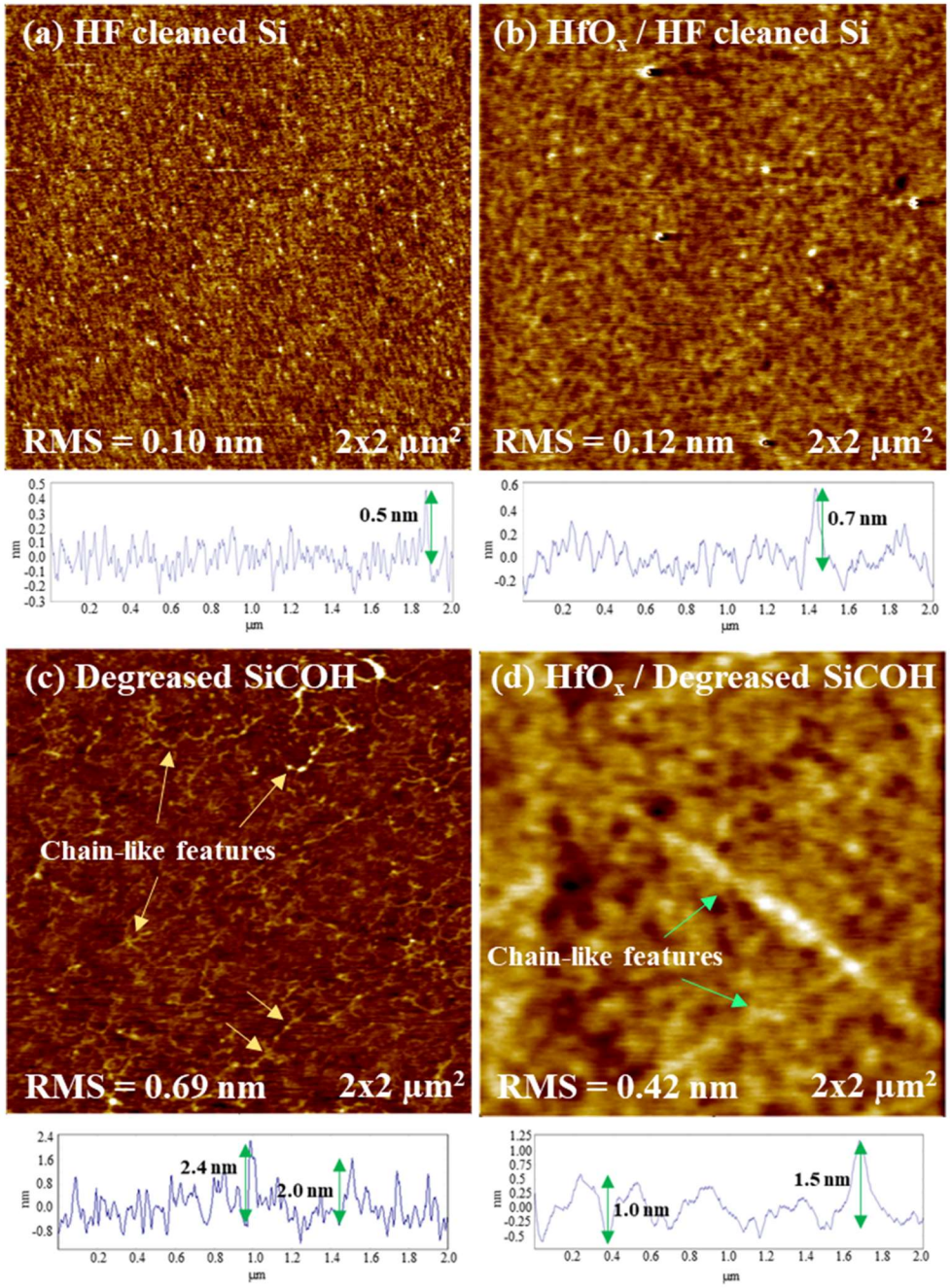

Figure 4.4. Surface morphologies of HF cleaned Si and degreased SiCOH before and after HfO_x deposition. (a) AFM image of HF cleaned Si. (b) The surface morphology of HF-Si after the HfO_x deposition at 200°C. (c) AFM image of degreased SiCOH. (d) AFM image of degreased SiCOH after the HfO_x deposition at 200°C.

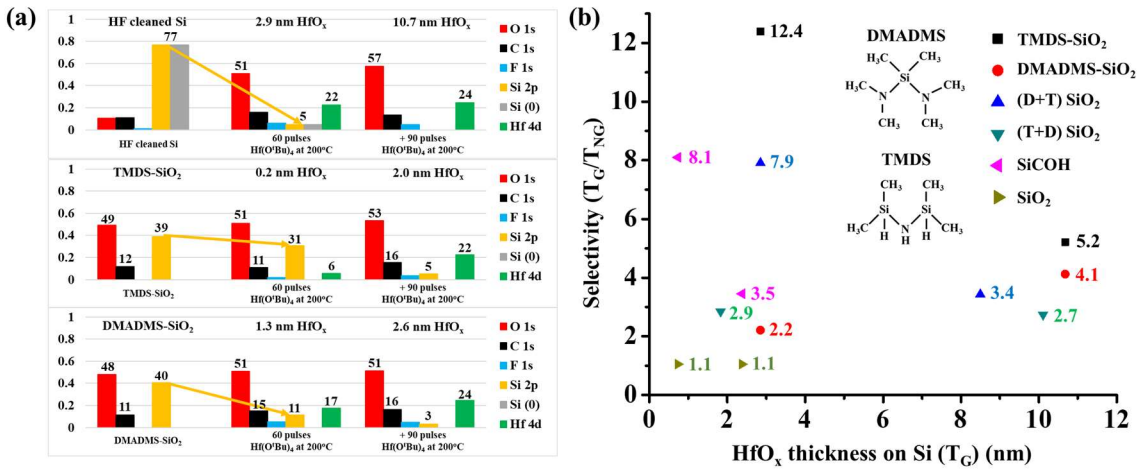

Figure 4.5. Selectivity metric (S) of passivated SiO_2 and SiCOH as a function of HfO_x thickness on Si. (a) Chemical compositions of HF cleaned Si, TMDS passivated SiO_2 and DMADMS passivated SiO_2 after selective HfO_x deposition at 200ºC. TMDS was the most effective passivant on OH-terminated SiO_2. The HfO_x on Si was 2.9 nm before less than a monolayer deposition occurred on TMDS-SiO_2. The DMADMS and TMDS molecular structures are shown on the right.

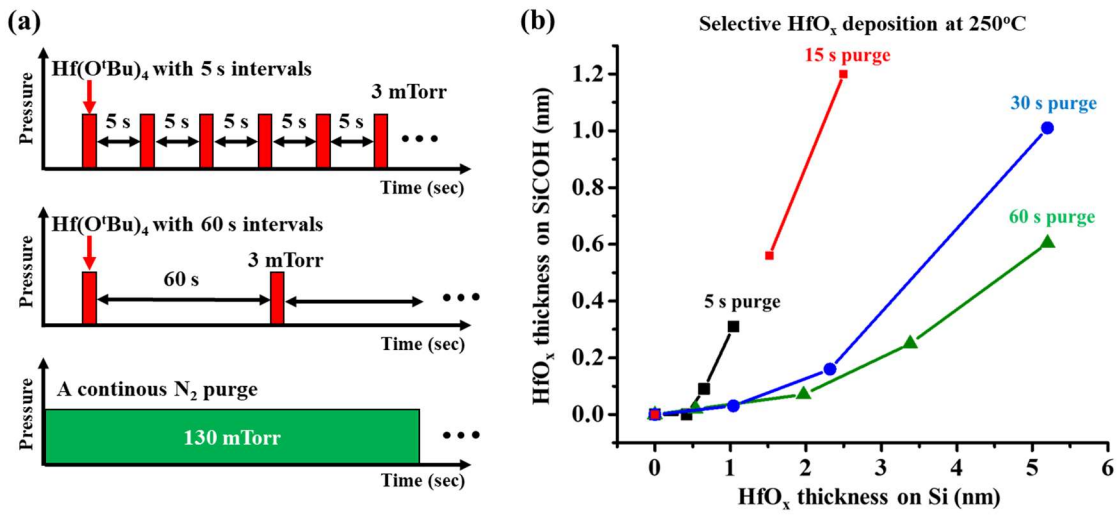

Figure 4.6. Selectivity enhancement of HfO_x on Si versus SiCOH by increasing the purge time between the $Hf(O^tBu)_4$ pulses at 250°C. (a) A schematic timing diagram of $Hf(O^tBu)_4$ doses with a continuous N_2 purge. (b) HfO_x thickness on SiCOH with the respect to HfO_x thickness on Si with different purge times. The selectivity was improved by increasing the purge time between the $Hf(O^tBu)_4$ pulses. 60 s purge time showed 2 nm HfO_x deposition on Si before any nucleation occurred on SiCOH.

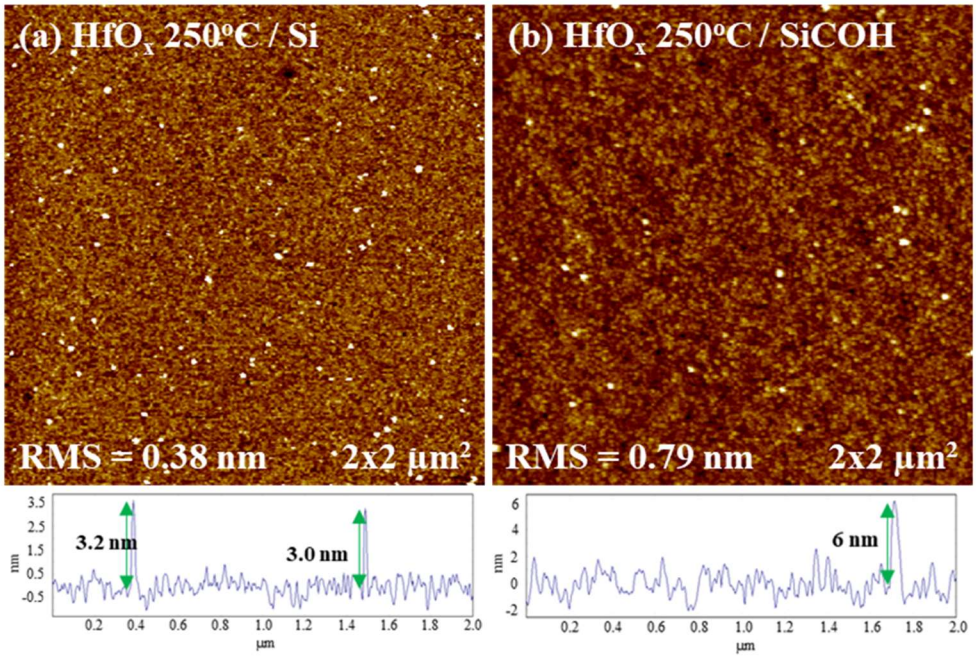

Figure 4.7. Surface morphology of the HfO_x films deposited at 250°C on Si and SiCOH. (a) HfO_x on H-terminated Si showed a conformal film with an RMS roughness of 3.8 Å. (b) On degreased SiCOH, HfO_x was conformal with ~6 nm tall particles.

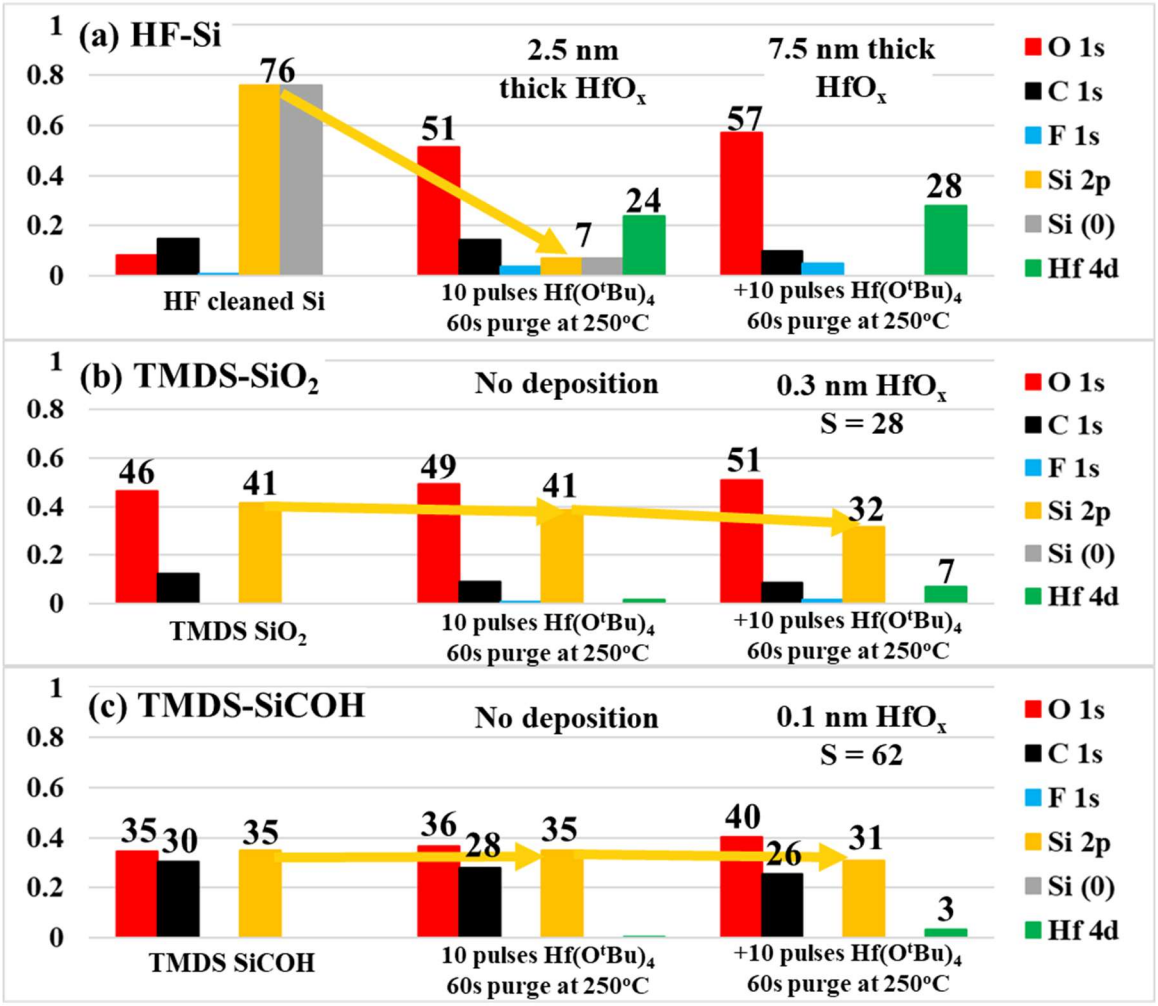

Figure 4.8. Selectivity enhancement of HfO_x on Si versus TMDS passivated SiO_2 and TMDS passivated SiCOH. (a) 20 pulses of $Hf(O^tBu)_4$ with 60 s purge on HF-Si at 250°C deposited 7.5 nm thick HfO_x. (b) On TMDS-SiO_2, 0.3 nm thick HfO_x was deposited which gives a selectivity metric of S= 28±1.9. (c) On TMDS-SiCOH, 0.1 nm thick HfO_x was deposited which gives a selectivity metric of S= 62±4.6.

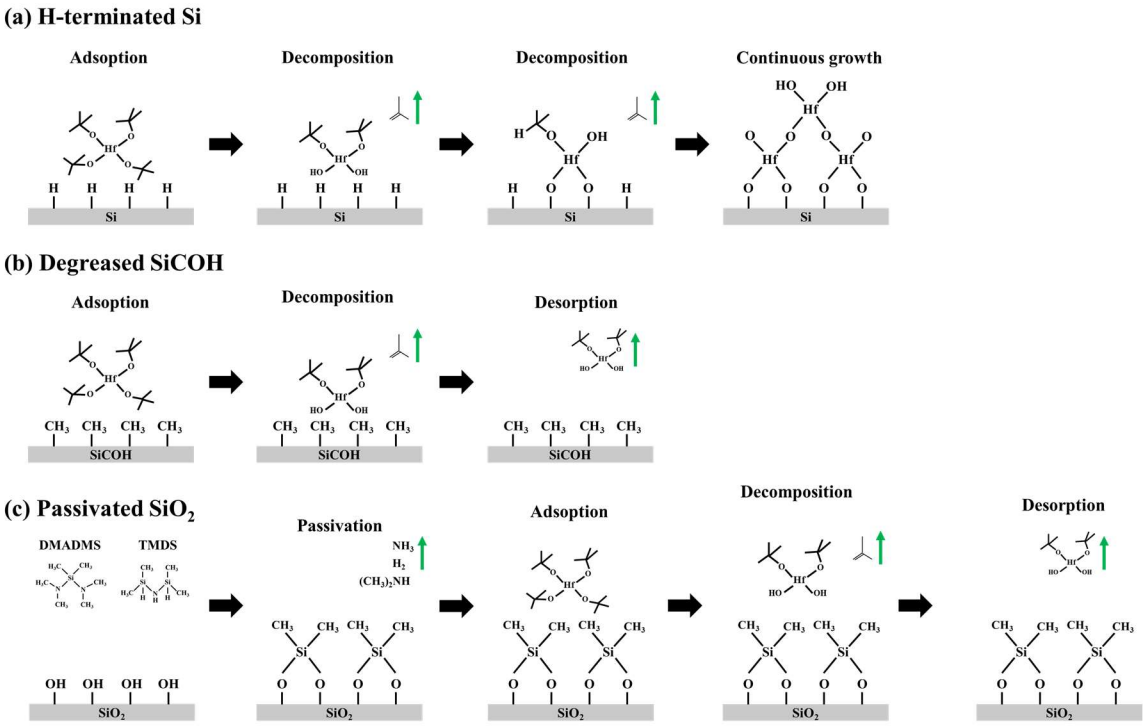

Figure 4.9. Mechanism of selective HfO_x pulsed CVD on Si versus SiCOH and passivated SiO_2. (a) On H-terminated Si, $Hf(O^tBu)_4$ adsorbs on the surface and decomposes into $Hf(O^tBu)_xOH_{4-x}$. Then OH reacts with H-Si and HfO_x continuously grows. (b) Adsorbed and decomposed $Hf(O^tBu)_4$ leaves from the O-Si-CH_3 terminated SiCOH surface. (c) TMDS and DMADMS reacts with OH-terminated SiO_2 and leaves a O-Si-CH_3 terminated surface which prevents the decomposed $Hf(O^tBu)_4$ from reacting.

4.8 References

(1) G. D. Wilk; R. M. Wallace, Appl. Phys. Lett. **1999**, 74, 2854.

(2) M.-T. Ho; Y. Wang; R. T. Brewer; L. S. Wielunski; Y. J. Chabal; N. Moumen; M. Boleslawski, Appl. Phys. Lett. **2005**, 87, 133103.

(3) B. Wang; W. Huang; L. Chi; M. Al-Hashimi; T. J. Marks; A. Facchetti, Chem. Rev. **2018**, 118, 5690.

(4) Y. Kuo; J. Lu; S. Chatterjee; J. Yan; H. C. Kim; T. Yuan; W. Luo; J. Peterson, M. Gardner, ECS Transactions **2006**, 1, 447.

(5) B. H. Lee; L. Kang; R. Nieh; W.-J. Qi; J. C. Lee, Appl. Phys. Lett. **2000**, 76, 1926.

(6) Y. Widjaja; C. B. Musgrave, J. Chem. Phys. **2002**, 117, 1931.

(7) R. L. Puurunen; A. Delabie; S. V. Elshocht; M. Caymax; M. L. Green; B. Brijs; O. Richard; H. Bender; T. Conard; I. Hoflijk; W. Vandervorst; D. Hellin; D. Vanhaeren; C. Zhao; S. D. Gendt; M. Heyns, Appl. Phys. Lett. **2005**, 86, 073116.

(8) M.-J. Choi; H.-H. Park; D. S. Jeong; J. H. Kim; J.-S. Kim; S. K. Kim; Appl. Surf. Sci. **2014**, 301, 451.

(9) Y. Senzaki; S. Park; H. Chatham; L. Bartholomew; W. Nieveen; J. Vac. Sci. Technol. A **2004**, 22, 1175.

(10) E. Oudot; M. Gros-Jean; K. Courouble; F. Bertin; R. Duru; N. Rochat; Christophe Vallée, J. Vac. Sci. Technol. A **2008**, 36, 01A116.

(11) S. X. Lao; R. M. Martin; J. P. Chang, J. Vac. Sci. Technol. A **2005**, 23, 488.

(12) M. S. Kavrik; E. Thomson; E. Chagarov; K. Tang; S. T. Ueda; V. Hou; T. Aoki; M. Kim; B. Fruhberger; Y. Taur; P. C. McIntyre; A. C. Kummel, ACS Appl. Mater. Interfaces **2008**, 10, 30794.

(13) V. R. Anderson; A. S. Cavanagh; A. I. Abdulagatov; Z. M. Gibbs; S. M. George, J. Vac. Sci. Technol. A **2014**, 32, 01A114.

(14) S. E. Atanasov; B. Kalanyan; G. N. Parsons, J. Vac. Sci. Technol. A **2016**, 34, 01A148.

(15) S. Sayan; S. Aravamudhan; B. W. Busch; W. H. Schulte; F. Cosandey; G. D. Wilk; T. Gustafsson; E. Garfunkel, J. Vac. Sci. Technol. A **2002**, 20, 507.

(16) T. S. Yang; K.-S. An; E.-J Lee; W. Cho; H. S. Jang; S. K. Park; Y. K. Lee; T.-M Chung; C. G. Kim; S. Kim; J.-H. Hwang; C. Lee; N.-S Lee; Yunsoo Kim, Chem. Mater. **2005**, 17, 6713.

(17) Y.J. Chabal; G.S. Higashi; K. Raghavachari; J. Vac. Sci. Technol. A **1989**, 7, 2104.

(18) B. Narayanan; R. Kumar; P.D. Foo, Microelectron. J. **2002**, 33, 971.

(19) S. M. Gates; G. Dubois; E. T. Ryan; A. Grill; M. Liu; D. Gidley, J. Electrochem. Soc. 2009, 156, G156.

(20) C. Ye; Z. Ning; T. Wang; X. Yu; Y. Wei; X. Qiana; J. Electrochem. Soc. **2007**, 154, G63.

(21) G. Li; G. Zheng; Z. Ding; L. Shi; J. Li; Z. Chen; L. Wang; A. A. O. Tay; W. Zhu, J. Mater. Sci. **2019**, 54, 2379.

(22) B. R. Kim; J. W. Kang; K. Y. Lee; J. M. Son; M. J. Ko, J. Mater. Sci. **2007**, 42, 4591.

(23) D. D. Wagman; W. H. Evans; V. B. Parker; R. H. Schumm; I. Halow; S. M. Bailey; K. L. Churney; R. L. Nuttall, J. Phys. Chem. Ref. Data **1982**, 11, 1807.